Evaluation and Correlation of Morphological, Blood Flow and Physiological Retinal Changes in a Rat Model of Glaucoma with a Combined Optical Coherence Tomography and Electroretinography System

by

Bingyao Tan

A thesis
presented to the University of Waterloo
in fulfillment of the
thesis requirement for the degree of
Doctor of Philosophy
in
Physics

Waterloo, Ontario, Canada, 2017

Examining Committee Membership

The following served on the Examining Committee for this thesis. The decision of the Examining Committee is by majority vote.

External Examiner	Marinko V. Sarunic Professor, School of Engineering Science Simon Fraser University
Supervisor(s)	Kostadinka Bizheva Associate Professor, Department of Physics and Astronomy University of Waterloo
Internal Member	Kevin J. Resch Professor, Department of Physics and Astronomy University of Waterloo
Internal Member	Matteo Mariantoni Associate Professor, Department of Physics and Astronomy University of Waterloo
Internal-external Member	Trefford Simpson Professor, Department of Physics and Astronomy University of Waterloo

AUTHOR'S DECLARATION

This thesis consists of material all of which I authored or co-authored: see Statement of Contributions included in the thesis. This is a true copy of the thesis, including any required final revisions, as accepted by my examiners.
I understand that my thesis may be made electronically available to the public.

Statement of Contributions

Chapter 3:

Choh V, Gurdita A, **Tan B**, Prasad RC, Bizheva K, Joos KM. "Short-Term Moderately Elevated Intraocular Pressure Is Associated With Elevated Scotopic Electroretinogram Responses," *Investig. Opthalmol. Vis. Sci*. 2016;57(4):2140. doi:10.1167/iovs.15-18770.

Vivian Choh, **Kostadinka Bizheva** and **Karen M Joos** conceived the study and provided study materials.

Bingyao Tan collected the OCT images; **Bingyao Tan**, **Akshay Gurdita** and **Vivian Choh** collected the STR and ERG data.

Bingyao Tan wrote the algorithm for xBMO calculation. **Bingyao Tan** and **Akshay Gurdita** analyzed the experiment data.

Ratna Prasad conducted the histology and immunohistochemistry.

Bingyao Tan, **Kostadinka Bizheva**, **Vivian Choh**, **Karen Joos** and **Akshay Gurdita** contributed to the interpretation of all results.

Vivian Choh wrote part of the first draft of the manuscript, while **Bingyao Tan** wrote the "Methods" sections related to the OCT system description, OCT imaging protocol and OCT image analysis.

All authors contributed to the final version for publication.

Chapter 4:

B. Tan, B. Maclellan, E. Mason and K. Bizheva. "The effect of acute intraocular pressure elevation to ischemic and non-ischemic levels on the rat retinal structure, function and blood perfusion, evaluated with a combined OCT + ERG system," submitted to *Scientific Reports*

Bingyao Tan and **Kostadinka Bizheva** conceived the study.

Kostadinka Bizheva provided the study materials.

Bingyao Tan designed, built and tested the combined OCT+ERG probe.

Bingyao Tan collected the OCT and ERG data, and **Benjamin Maclellan** helped with the animal handling and monitoring.

Bingyao Tan wrote the algorithm for *en-face* TRBF calculation, the microvascular density calculation and the OCTA image extraction.

Bingyao Tan, Erik Mason and Benjamin Maclellan wrote the algorithm for the microvascular map generation.

Bingyao Tan analyzed the data and wrote the first draft of the manuscript.

Kostadinka Bizheva contributed to the interpretation of the results.

All authors contributed to the final version of the manuscript.

Chapter 5:

B. Tan, A. Gurdita, V. Choh, K. M. Joos, R. Prasad and Bizheva, Kostadinka. "Morphological and functional changes in the rat retina associated with 2 months of intermittent moderate intraocular pressure elevation, measured with a combined OCT and ERG system," submitted to the *Journal of Biomedical Optics.*

Kostadinka Bizheva, Vivian Choh and **Karen M Joos** conceived the study and provided the materials for the study.

Bingyao Tan collected the OCT, ERG and STR data, and **Akshay Gurdita** helped with the animal handling and monitoring.

Bingyao Tan wrote the OCT image processing algorithms and analyzed all OCT, ERG and STR data.

Ratna Prasad conducted the histology.

Kostadinka Bizheva, **Vivian Choh**, **Karen Joos** and **Akshay Gurdita** contributed to the interpretation of all results.

Bingyao Tan wrote the first draft of the manuscript.

All authors contributed to the final version of the manuscript.

Chapter 6:

B. Tan, E. Mason, B. Maclellan and K. Bizheva. "Measurement of neurovascular coupling in rat's retina measured with combined Functional Doppler Optical Coherence Tomography (fDOCT) and electroretinography (ERG)," *Investig. Ophthalmol. Vis. Sci.*, 2017.58:1673–1681. DOI:10.1167/iovs.17-21543.

Bingyao Tan and **Kostadinka Bizheva** conceived the study.

Kostadinka Bizheva provided the study material.

Bingyao Tan collected all data, and **Erik Mason** helped with the animal monitoring.

Bingyao Tan and **Benjamin MacLellan** wrote the algorithm for temporal blood flow quantification.

Bingyao Tan analyzed the data and wrote the first draft of the manuscript.

Kostadinka Bizheva contributed to the interpretation of the results.

All authors contributed to the final version of the manuscript.

Chapter 7:

B. Tan, E. Mason, B. MacLellan and K. Bizheva. "The Effect of Acutely Elevated Intraocular Pressure on the Functional and Blood Flow Responses of the Rat Retina to Flicker Stimulation," *Investig. Ophthalmol. Vis. Sci. (in revision).*

Bingyao Tan and **Kostadinka Bizheva** conceived the study.

Kostadinka Bizheva provided the study material.

Bingyao Tan conducted the study, and **Erik Mason** helped with the animal monitoring.

Bingyao Tan wrote the algorithm for TRBF and blood vessel size quantification.

Bingyao Tan analyzed the data and wrote the first draft of the manuscript.

Kostadinka Bizheva contributed to the interpretation of the results.

All authors contributed to the final version of the manuscript.

Chapter 8:

Bingyao Tan, Zohreh Hosseinaee and K. Bizheva. "Dense concentric circle scanning protocol for measuring pulsatile retinal blood flow in rats with Doppler optical coherence tomography," *Journal of Biomedical Optics (in revision).*

Bingyao Tan and **Kostadinka Bizheva** conceived the study.

Kostadinka Bizheva provided the study material.

Bingyao Tan conducted the experiment and **Zohreh Hosseinaee** assisted with the animal handling and monitoring.

Bingyao Tan wrote the image analysis algorithms for the automatic blood vessel segmentation and the pulsatile blood flow quantification.

Bingyao Tan analyzed the data.

Kostadinka Bizheva contributed to the interpretation of all results.

Bingyao Tan wrote the first draft of the manuscript.

All authors contributed to the final version of the manuscript.

Abstract

Glaucoma is a chronic disease associated with progressive dysfunction of the retinal ganglion cells (RGC), reduction of the retinal blood flow, thinning of the retinal nerve fiber layer (RNFL) and deformation of the optical nerve head (ONH). It is the second leading cause of blindness worldwide, with an estimate of 64.3 million people between the ages of 40 to 80 years affected in 2013, 76.7 million by 2020, and 111.8 million by 2040. Currently, there is no cure for glaucoma and any clinically available pharmaceutical or surgical approaches to treating the disease can only slow its progression. Therefore, early detection and treatment are essential for managing the glaucoma progression. Elevated intraocular pressure (IOP) is one of the most well studied and documented pathogenic risk factors for open-angle glaucoma (OAG), and as such, numerous animal models have been developed to study the acute and chronic IOP elevation effect on the ONH structure, retinal blood perfusion and RGC function. However, most of these studies utilized static chronic IOP elevation, while the relation between the IOP dynamics and the progression of glaucoma is still poorly understood. Joos et al. proposed a rat model of glaucoma that utilized a dynamic approach to IOP elevation by use of a vascular loop that consists of short duration (~1h), intermittent IOP elevations. This model resembles closely the daily IOP spiking observed in glaucomatous patients, especially during the early stages of the disease. Better understanding of how the retina (human and animal) responds to such intermittent spikes of the IOP can provide ophthalmologists with valuable information on the origins and early stages of glaucoma development when treatment would be most efficient, as well as insights into developing new therapeutic approaches for glaucoma.

Over the past few decades, a number of *ex-vivo* and *in-vivo* optical imaging modalities ranging from histopathology to confocal microscopy and optical coherence tomography (OCT) have been used to image changes in the morphology of the retina and the optic nerve head (ONH) in human subjects and animal models of OAG. Laser Doppler Flowmetry, Doppler OCT (DOCT) and Optical Coherence Tomography Angiography (OCTA) have been utilized to image and quantify changes in the total retinal blood flow and the blood perfusion in retinal capillaries during IOP elevations. Furthermore, electroretinography (ERG) has been used to assess changes in the retinal

function (response to visual stimulation) during elevated IOP. However, all previous studies collected information about the morphological, functional and blood flow/perfusion changes in the retina during elevated IOP separately, at different time points, which prevented the researchers from correlating those changes and uncovering the relationship between them, typically referred to as neurovascular coupling.

Since OCT provides both intensity and phase information in a single acquisition, this imaging technology is able to assess changes in the retinal morphology, function and blood flow/perfusion *in-vivo* and simultaneously. Therefore, the main goals of this PhD project were to:

- Develop a combined OCT+ERG imaging system that can image *in-vivo* and record simultaneously, changes in the retinal morphology, retinal electrophysiological response to visual stimulation and retinal blood flow/perfusion at normal and elevated IOP.
- Test the performance of the OCT+ERG system in a rat model of glaucoma.
- Utilize the OCT+ERG technology and the dynamic IOP rat model of glaucoma based on the vascular loop, to investigate the effects of acute and chronic IOP elevation to ischemic and non-ischemic IOP levels on the rat retina.
- Utilize the OCT+ERG technology to investigate neurovascular coupling in the rat retina at normal and abnormal IOP levels.

Results from this PhD research have been published or summarized in manuscripts that are currently under review. Therefore, this PhD thesis was prepared in such a way that individual manuscripts represent separate thesis chapters.

Acknowledgements

These years will definitely be the cherished treasure of my life and I would like to acknowledge the persons who were of great importance to me during that time. This study would not have been possible without your generous support.

First, I would like to thank Dr. Kostadinka Bizheva, my supervisor as well as mentor, for nourishing me with knowledge and training me to be a scientist. She is always both positive and constructively critical to the ideas I came up with. Those challenges and encouragements helped me to grow into an independent researcher. Dr. Bizheva provided a wonderful research atmosphere in the lab that encouraged both independent studies and team work. I am very fortunate to have been one of the researchers in her lab and gained a lot of support scientifically and mentally from all of my colleagues.

I also want to thank Dr. Bizheva for financially supporting my research and providing funding for journal publications and my trips to international conferences. She provided spectacular opportunity for me to collaborate with researchers from other fields in this interdisciplinary area. Dr. Vivian Choh from the University of Waterloo and Dr. Karen Joos from the Vanderbilt University provided valuable suggestions and training related to the animal studies and the rat model of glaucoma, while Dr. Alexander Wong provided invaluable advice on development of new OCT image processing approaches and offered great opportunities for me to collaborate with talented researchers from the Vision and Imaging Processing Lab at the University of Waterloo. Furthermore, Dr. Bizheva encouraged me to get involved in many other forefront research projects in her lab, such as the development of the sub-micrometer OCT system and the linescan OCT system for human cornea and limbus imaging all of which greatly extended my knowledge and broadened my view in this research field.

Second, I want to take this chance to thank Nancy Gibson and Jean Flanagan from the University of Waterloo Central Animal Facility for their help and continuous support for all animal experiments, and Harmen Vander Heide from the University of Waterloo Science Shop for his and his team's assistance with the mechanical design and machining of custom optomechanical components for the OCT+ERG system. I am also fortunate enough to have Dr. Donna Strickland,

Dr. Kevin Resch and Dr. Trefford Simpson as my committee members throughout my PhD study. Your constructive critique and prudent advice are precious experience for me.

Especially, I want to thank my parents, my girlfriend Tuo Tan and my friends for gracious support of my choice to become a scientist and throughout my PhD training. I am very grateful for the support you offered during the difficult times of my PhD training and for celebrating my every single success regardless of how small it may have been. I could not even begin my PhD study in the first place without your understanding and non-hesitant support.

To my Mom and Dad, for their endless love and support.

Table of Contents

List of Figures

List of Abbreviations

AMD	Age-Related Macular Degeneration
ANOVA	Analysis of Variance
ANSI	American National Standards Institute
CCD	Charge Coupled Device
CL	Collimating
DC	Dispersion Compensator
DG	Diffraction
DOCT	Doppler Optical Coherence Tomography
DR	Diabetic Retinopathy
ELM	External Limiting Membrane
ERG	Electroretinography
FHC	First Harmonic Component
FL	Focusing Lens
FOCT	Functional Optical Coherence Tomography
FOV	Field of View
FWHM	Full Width Half Maximum
GCL	Ganglion Cell Layer
ICG	Indocyanine Green
IFT	Inverse Fourier Transform
INL	Inner Nuclear Layer
IOP	Intraocular Pressure
IOS	Intrinsic Optical Signal
IPL	Inner Plexiform Layer
IS	Inner Segment
M	Mirror
MIP	Maximum Intensity Projections
NA	Numerical Aperture
NIR	Near-Infrared

OAG	Open Angle Glaucoma
OCT	Optical Coherence Tomography
OCTA	Optical Coherence Tomography Angiography
OMAG	Optical Microangiography
ONH	Optic Nerve Head
ONL	Outer Nuclear Layers
OPD	Optical Path Difference
OS	Outer Segment
PBS	Phosphate Buffered Saline
PC	Polarization Controllers
PSF	Point Spread Function
RGC	Retinal Ganglion Cell
RMS	Root Mean Square
RNFL	Retinal Nerve Fiber Layer
RPE	Retina Pigmental Epithelium
SD-OCT	Spectral Domain Optical Coherence Tomography
SHC	Second Harmonic Component
SLD	Superluminescent Diode
SNR	Signal to Noise Ratio
SS-OCT	Swept Source Optical Coherence Tomography
STR	Scotopic Threshold Response
TBRF	Total Retinal Blood Flow
TDOCT	Time Domain Optical Coherence Tomography
UHR-OCT	Ultra-High Resolution Optical Coherence Tomography
VEP	Visual Evoked Potential

List of Tables

Chapter 1
Introduction and Overview

1.1 Glaucoma

Glaucoma is the second leading cause of blindness worldwide, with an estimate of 64.3 million people between the ages of 40 to 80 years affected in 2013, 76.7 million by 2020, and 111.8 million by 2040[1]. The whole population of people with glaucoma worldwide will increase 74% from 2013 to 2040. A recent systematic review predicts a glaucoma population increase of 19% in the United Kingdom, 9% in Europe and 18% in the United States in the next decade[2].

Glaucoma is usually characterized with progressive RGC loss[3]–[5], altered retinal vascular[6]–[8] and morphological change of the ONH including the remodeling of the lamina cribrosa[9]–[11] and physiological cupping[12]–[15]. Recently, factors such as retinal autoregulation[16], [17] and retinal neurovascular coupling[18]–[23] have been shown to be associated with glaucoma. Early glaucoma is usually quiet and asymptomatic, thus it lacks awareness until sever and irreversible vision loss happens. Therefore, early diagnosis and treatment plays an important role to prevent vision loss. However, so far, the exact mechanism of this disease and the factors that cause disease progression are still not fully understood.

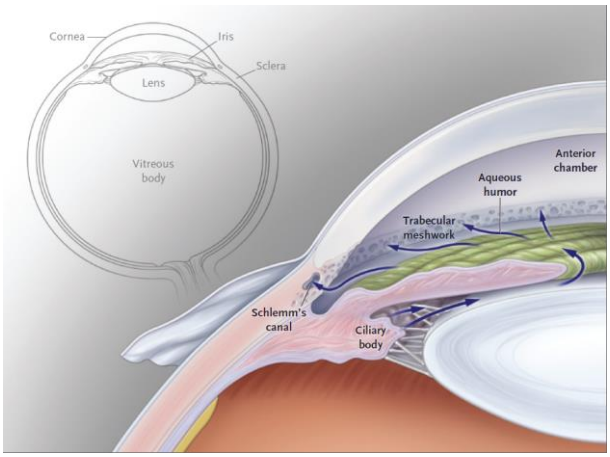

Figure 1.1 Circulation of the aqueous flow. Reproduced with permission from [4], Copyright Massachusetts Medical Society.

High IOP is a well-known risk factor in open-angle glaucoma, therefore, lowering IOP is still the main choice for clinical treatment of glaucoma. IOP is regulated by the balance of the production and drainage of the aqueous humour in the anterior chamber of the eye. As shown in Figure 1.1, the production of aqueous humour occurs in the ciliary epithelium, which is controlled by the ciliary body in the posterior chamber of the eye. The aqueous humour flows into the anterior chamber and provides metabolic supply to the iris, lens and cornea. Afterward, the aqueous humour is collected by a spongy tissue, named the trabecular meshwork, and drains into the tube-shaped Schlemm's canal. Clogging of the trabecular meshwork, obstruction or collapse of the Schlemm's canal, and the increased resistance of the inner canal wall could all cause in-balance of the aqueous humour circulation, resulting in IOP elevation and progression of OAG. For this reason, investigators use elevated IOP as an approach to study its effect on the retinal structure and function, and attempt to correlate the high IOP induced damage to the progression of glaucoma in human subjects.

Experimental glaucoma with IOP elevations aims to study the mechanism of IOP-induced alterations in the eye and bridge the fundamental pathological studies and clinical management of

the disease. Previously, several animal models have been used in experimental glaucoma, such as rabbits[24]–[26], rodents[27]–[39], cats[40], dogs[40], pigs[41], zebrafish[42] and monkeys[10], [43]–[47]. Among all of the above animal models, rodents are the most widely used because of certain advantages[48]. First, rodents are relatively affordable, easily available, and easy to maintain in an animal facility. Second, rats are mammals that have anatomical[49] and developmental[50] anterior chamber, aqueous outflow and ONH similar to that of humans. Third, the habitual IOP level, as well as IOP elevation in response to retinal and ONH operation are similar to the human ones. One limitation of the rodent models of glaucoma is that rat retina does not have a macula, however, since glaucomatous pathogenesis occurs commonly at the ONH and its periphery this limitation is not very significant.

Over the past several decades, numerous IOP elevation protocols have been developed, which include genetic, chronic, acute, and intermittent IOP elevations. Based on the different levels of IOP elevation, they can also be differentiated into non-ischemic and ischemic IOP elevation. Below is a brief description of these IOP elevation protocols.

The genetic glaucoma animal model, especially, DBA/2J mice[51], [52], is associated with mutation of two genes, Gpnmb and Tyrp1, and an enzyme related to melanin synthesis, which results in alteration of the iris's stroma and causes change to the aqueous outflow. This strain of mice develops elevated IOP as early as 9-12 months after birth, pronounced ganglion cell loss has been observed as early as 10 months of age, and progressive optic nerve atrophy and ONH cupping occurs as early 12 months of age. This animal model of static IOP elevation has several limitations. One, there is no control eye in this model to provide baseline information for the retinal structure, function and blood flow/perfusion. Second, large variations of the elevated IOP level and as well

as onset of the IOP elevation have been reported, which could affect negatively the conclusions from animal research studies utilizing this model of IOP elevation.

Cannulation of the anterior chamber method requires connection of an external reservoir with physiological solution to the anterior chamber through a needle. The level of IOP elevation is adjusted by changing the height of the reservoir relative to the eye. Bui[31], [53], [54] used ERG and STR to show that by using cannulation to raise the IOP acutely, retinal function is attenuated temporally for the duration of the elevated IOP and recovered back to baseline shortly after the IOP returned to a normal value[55], [56]. Zhi et al. [57]–[59] also used cannulation to increase the IOP from 30 mmHg to 100 mmHg, and by utilizing DOCT and OMAG, he demonstrated that the TRBF and the retinal capillary density in the IPL and the OPL of the rat retina decreased with the increase of the IOP elevation level. The same study also showed acute deformation of ONH and rearrangement of the lamina cribrosa[60] that returned to baseline shortly after normalization of the IOP. A recent publication points out that the cannulation method is associated with inflammation of the retina[61], and the injected liquid can cause higher optical aberrations that will affect the quality of the optical images, as well as change the impedance of the electrical signal, which will affect the ERG recordings, and therefore, the conclusions from the study based on the analysis of the corrupted optical images and ERG data.

Photocoagulation of the trabecular meshwork and the episcleral veins could generate longitudinal IOP elevation over time and 16.1% RGC loss has been reported with this method as early as one-week post operatively[62]. In another study, retinal function was attenuated as early as 24h post operatively, as shown by reduced ERG and STR amplitudes[63]. One major disadvantage of this method is that the IOP elevation level cannot be controlled precisely. An IOP spike is typically

observed immediately after the operation, followed by progressive IOP drop over time, and IOP normalization can happen as early as 5 days after the operation. Moreover, IOP spikes could introduce temporal retinal ischemia, which would cause a damage to the retinal structure and function and has different physiological mechanism than moderately IOP elevation alone.

Injection of polystyrene microbeads into anterior chamber can cause partial blockage of the aqueous outflow in trabecular meshwork and the Schlemm's canal. Chronic, moderate IOP elevation can be introduced with this method, and animal studies based on this method showed that degeneration of the RGCs reached 50% after 8 weeks post-injection[64]. By combining microbeads injection and laser coagulation[65], more sustainable IOP elevation can be achieved within 18 weeks compared to injection of microbeads or coagulation alone. Animal studies have reported significant thinning of the RNFL at 8 weeks, as well as between week 8 and 15, while changes in the retinal function were insignificant.

Episcleral vein injection of hypertonic saline can cause trabecular meshwork sclerosis and obstruction of the aqueous outflow[66]–[70]. Sustained moderate IOP elevation has been recorded within 200 days post-op and diurnal IOP fluctuation pattern has been reported[71]. Progressive RGC loss, alteration of the retinal function and optic nerve atrophy have been reported 32 weeks after for IOP elevation using this method.

More recently, circumlimbal suture with compression of the equator of the eyeball with a tight suture was used to induce a mild IOP elevation[34], [72], [73]. The sustained IOP elevation was initiated by a IOP spike that occurred within the first 3 hours of the suture placement. At week 15, there was a significant attenuation of RGC function and thinning of the RNFL, while no significant

reduction of RGC function or RNFL thinning was reported at week 8[34]. This method showed no pronounced effect on the anterior chamber and no evidence of inflammation process, however, circumlimbal suture placement requires specific skills and results (IOP level) vary significantly with the personnel performing the procedure.

All of the aforementioned IOP elevation protocols generate a static, longitudinal IOP elevation, which causes difficulty when comparing results from the animal with those of clinical studies on OAG patients. One major difference is that OAG patients exhibit dynamic changes of the IOP over the course of 24h[74], [75], and results from most recent studies show that intermittent IOP spiking to moderate levels of ~ 35 mmHg also results in RGC loss and RNFL thinning[30], [76]. A headstand yoga posture (Sirsasana) had been reported to elevate IOP immediately, and routine practitioners could eventually develop glaucoma[77], [78]. In other studies, recurrent uveitis and its treatment has been shown to cause intermittent IOP spiking that can also lead to glaucoma uveitis[79], [80].

Therefore, an animal model with intermittent IOP elevation that can accurately mimic IOP spiking in glaucomatous patients is needed. Gramlich et al used suction-cup oculopression[76] to elevate the IOP to 30-35 mmHg for one hour a day, and reported significant loss of RGC density in the treated eye after 30 repeated procedures over a period of 6 weeks. Joos et al[30] used an adjustable vascular loop to elevate the IOP to 35 mmHg for an hour per day on 6 days of the week over a period of 6 weeks, and reported up to 25% thinning of the RNFL, 7%–10% loss of RGC somas, and axonal degeneration in the optic nerve in the treated eye. Compared to the suction-cup approach, the vascular loop method has a relatively lower cost and is easier to apply. Moreover, there is no need to anesthetize the animal since the rats were tolerant to the vascular loop. This is

an important point, as studies suggest that different types of anesthesia have accumulative effect on the retinal function. Last but not least, the vascular loop is placed anterior to the eye chamber and thus has only a weak effect on the transmission of the optic beam (slight increase in the axial eye length, anterior chamber length and curvature of the cornea), which does not affect strongly the *in-vivo* optical imaging of the retina during IOP elevation.

As the vascular loop provides a dynamic animal model of OAG, the question remains: what is the acute and progressive (chronic) change of the retinal morphology, blood perfusion and function in this rat model of glaucoma. This thesis aims to answer the question above and to provide insight to the understanding of the progression of glaucoma.

1.2 Chapter Overview

This thesis is organized based on several journal manuscripts (published or currently in review):

Chapter 2 describes the concept of ERG, Spectral Domain OCT and its extensions, like phase resolved Doppler OCT and OCT angiography (OCTA). Also, it briefly discusses the advantages for OCT to assessing the morphology, blood perfusion, and function of the rat retina in our model of glaucoma.

Chapter 3 focuses on the effect of acute IOP elevation to a moderate level (35 mmHg) and reversible recovery of the ONH depression and the retinal function in the rat's eye.

Chapter 4 examines the effect of different levels of acute IOP elevation from normal (10 mmHg) to ischemic (70 mmHg) levels. ONH morphology, retinal total blood flow, retinal blood perfusion and retinal function were assessed.

Chapter 5 focuses on a chronic rat model of glaucoma. It studies the effect of intermittent, moderate level IOP elevation over a period of 8 weeks, on the rat retinal morphology and function.

Chapter 6 discusses a modified OCT+ERG system setup and data acquisition protocol for simultaneous measurement of visually evoked retinal blood flow and retinal function changes.

Chapter 7 Summarizes results from a study where the same imaging system and data acquisition protocol as the ones used for the study in Chapter 6, were used to investigate the effect of IOP elevation on the retinal neurovascular coupling.

Chapter 8 Describes a new scanning protocol and an automatic retinal blood vessel segmentation algorithm designed to measure more accurately pulsatile retinal blood flow. It enables the accurate quantification of pulsatile retinal blood flow with a relatively slow camera, and it can be easily transferred to human clinical studies.

Chapter 9 Summarizes the results from this PhD thesis and discusses potential future studies.

Chapter 2 Optical Coherence Tomography (OCT) and Electroretinography (ERG)

2.1 Theory of Optical Coherence Tomography

The word tomography originated from the ancient Greek *tomos*, meaning 'section'. OCT is a non-invasive imaging technology that utilizes the coherence properties of backscattered light to generate cross sectional images of the imaged object. The first clinical application of OCT was for non-contact, *in-vivo* imaging of the structure of the human retina back in 1991. Over the past 25 years, advances in laser and camera technologies have allowed for dramatic improvement of the spatial resolution, sensitivity, scanning range and image acquisition rate of OCT. Furthermore, utilization of different scanning protocols, as well as phase information in addition to intensity, has resulted in the development of OCT extensions such as Doppler OCT and OCT angiography (OCTA) that are currently used to image and quantify blood flow and blood perfusion of biological tissue, including the retina. Over the past 25 years, OCT and its functional extensions have found a broad range of clinical and fundamental research applications other than in ophthalmology: for example, in cardiology, dermatology, dentistry, etc. Today, the majority of the clinical and commercial OCT systems are still used mainly for retinal imaging due to the semi-transparent properties of the retina, and the distinct retinal layered structure visible in a single OCT cross-sectional image. This section presents an overview of the general principles of operation of OCT and some of the configurations and OCT extensions that that were utilized in this PhD research project.

2.1.1 Spectral Domain Optical Coherence Tomography

At the core of most OCT systems is an interferometer design that was developed in 1889 by Albert

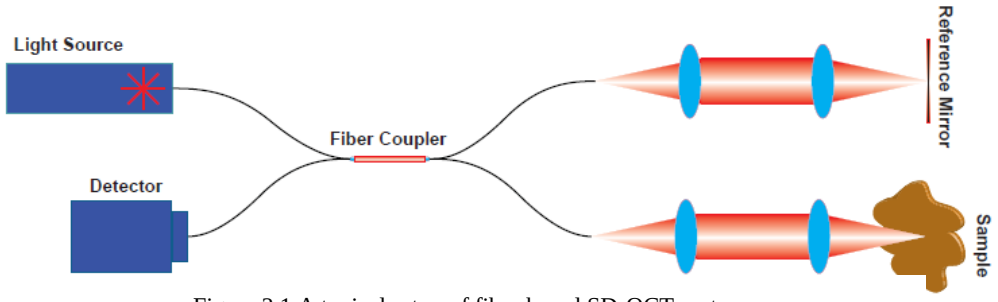

Figure 2.1 A typical setup of fiber based SD-OCT system

Abraham Michelson and is currently referred to as "Michelson interferometer".

A general schematic of a typical fiber-based Spectral Domain OCT (SD-OCT) system is shown in Figure 2.1. The output of a low coherence light source is connected to a 2×2 fiber coupler that divides the light into sample and reference arms. Backscattered light from different depths within the imaged object is coupled back into the sample arm fiber and interferes with the light back-reflected from the mirror in the reference arm of the interferometer. The interferometric pattern is projected though a spectrometer onto a linear array camera at the detection end of the SD-OCT system. Therefore, the intensity of the interference pattern, *I*, can be expressed as a superposition of the reference and sample arm beam:

$$I = \frac{\eta}{4}\{I_r + I_s + 2\sqrt{I_s I_r}\cos[\,2k(z_s - z_r)]\} \tag{2.1}$$

where η is the detector responsibility, I_r and I_s are the back scattered intensity from the reference and sample arms, respectively. $2k(z_s - z_r)$ is the phase difference between the sample and reference beams, where $k = 2\pi/\lambda_0$ is the wavenumber and λ_0 is the central wavelength of the light

source measured in free space, and $z_s - z_r$ is the OPD between the same and reference beams. When the imaged sample has spatially varying refractive index that can generate reflections from multiple depths inside the imaged object (e.g. biological tissue) and the light source has broad bandwidth emission spectrum that can be expressed as $S(k)$, then equation 2.1 can be modified to:

$$\begin{aligned} I(k) = {} & \frac{\eta}{4} S(k) \left(R_r + \sum\nolimits_{m=1}^{n} R_m \right) \\ & + \frac{\eta}{4} \sum_{m=1}^{n} S(k) \sqrt{R_r R_m} \cos[\, 2k(z_r - z_m)] \\ & + \frac{\eta}{4} \sum_{m \neq l = 1}^{n} 2S(k) \sqrt{R_l R_m} \cos[\, 2k(z_l - z_m)] \} \end{aligned} \tag{2.2}$$

where *R* is the spectral-dependent reflectivity of the imaged object. Here, the first term is the DC component from the reference mirror that appears as background in the OCT image. The second term is called the cross-correlation term, representing the interference component between multiple reflections from different depths inside the imaged object and the reference mirror. The last term is called the auto-correlation term, representing the interference between multiple reflections from different depths within the imaged object. In order to detect the spectral signal, SD-OCT employs a diffraction grating to separate different frequency components into different diffraction angles, and all the frequency components are recorded by a linear array CCD or CMOS camera. By taking the Fourier transform of $I(k)$, the depth-dependent reflectivity profile, *I*(z), for the multiple layers in the imaged object can be generated.

$$I(z) = \mathcal{F}^{k\to z}[I(k)] = \frac{\eta}{8} i(z) \left(R_r + \sum\nolimits_{m=1}^{n} R_m \right) + \frac{\eta}{8} \sum_{m=1}^{n} \sqrt{R_r R_m}\, i(z) * \delta(z_r - z_m) + \frac{\eta}{8} \sum_{m \neq l = 1}^{n} 2\sqrt{R_l R_m}\, i(z) * \delta(z_l - z_m) \tag{2.3}$$

where $i(z) = \mathcal{F}^{k\to z}[S(k)]$. Note that because of the conjugate symmetry of the Fourier transform, there is a factor of 2 difference between the intensity profile and the recorded interferogram. The DC and the auto-correlation components appear close to the zero-delay line since the OPD between the individual layers in the sample is small compared to the OPD between the beam splitter and the imaged object. Therefore, by adjusting the OPD between the reference arm and the sample arm, the cross-correlation components can be separated from the background. The cross-correlation components contain information about the depth-dependent reflectivity of the sample, *R(z)*. A one-dimensional OCT scan along depth (z direction) is referred to an "A-scan". By scanning the OCT imaging beam laterally over the imaged object with a galvanometric scanner or by translating the object in transverse direction (e.g. X) relative to the OCT imaging beam while acquiring OCT A-scans continuously, a 2D cross-sectional OCT image can be generated (also called an OCT B-scan). By scanning the imaging beam along two orthogonal transverse directions (X and Y) with two galvanometric scanners, or by translating the imaged object relative to the OCT imaging beam in a 2D transverse raster pattern, a 3-D image of the object can be reconstructed.

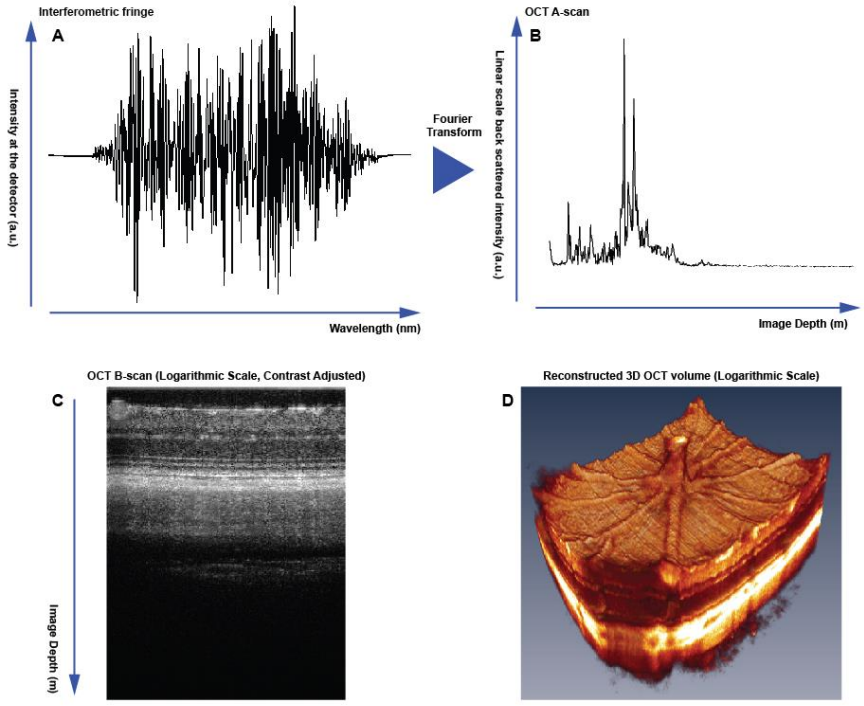

Figure 2.2 (A) Interferometric fringe recorded from camera provides information of different sinusoidal frequencies. (B) An OCT A-scan (1D, depth-dependent reflectivity profile) can be generated by taking the Fourier transform of the interferometric fringe. (C) An OCT B-scan of a rat retina generated by stitching the A-scans from different transverse positions. Logarithmic scale with contrast adjustment can be applied for optimal visualization. (D) A volumetric OCT image of the rat retina centered at the ONH.

Axial resolution

The axial OCT resolution, Δz, is defined as the FWHM of the cross-correlation intensity profile between reference mirror reflection and single perfect reflection from the sample arm, i.e. $\frac{\eta}{8}\sqrt{R_r R_s}i(z) * \delta(z_r - z_s)$. Hence, the axial resolution is calculated as the FWHM of $i(z)$.

Assuming that the spectrum of the low-coherence light source has a Gaussian profile, which can be expressed as:

$$S(k) = |S_0|e^{-\frac{(k-k_0)^2}{\Delta k^2}} \tag{2.4}$$

$i(z)$ can be calculated as:

$$i(z) = \mathcal{F}^{k\to z}\, S(k) = \int_{-\infty}^{\infty} S(k) e^{-ikz} dk = |I_0| e^{-z^2 \Delta k^2} \tag{2.5}$$

where the FWHM of $i(z)$ is $2\sqrt{\ln 2}/\Delta k$. The axial resolution can also be expressed in terms of the central wavelength, λ_0, and the FWHM, $\Delta\lambda$, of the light source, with the relation $\Delta k = \frac{\pi}{2\ln 2}\frac{\Delta\lambda}{{\lambda_0}^2}$; $\Delta z = \frac{2\ln 2}{\pi}\frac{{\lambda_0}^2}{\Delta\lambda}$.

Theoretically, the axial resolution in free space is only determined by the spectral characteristics of the light source, which means that a shorter central wavelength and a broader spectral bandwidth will result in higher axial resolution. In practice, the axial OCT resolution is dependent both of the OCT system's design (transmission properties of the optical and fiber-optic components, the number of pixels and the spectral responsivity of the camera) and the optical properties of the imaged object (wavelength dependent scattering and absorption).

Digital axial resolution

As the interferometric fringes are recorded by a CCD or a CMOS camera with finite number of pixels, based on the Nyquist theorem, the maximum sinusoidal frequency that can be detected without aliasing is half of the sampling frequency of the detector. Moreover, in OCT, higher image depth is associated with higher frequencies in the spectral domain due to the larger OPD, thus the limit of the sinusoidal frequency detection gives rise to the corresponded maximum imaging depth:

$$\text{image depth} = \frac{{\lambda_0}^2}{4\delta\lambda} \tag{2.6}$$

where $\delta\lambda$ is the spectral sampling interval of the detector. Therefore, the axial digital resolution can be calculated given the total image depth and the number of pixels in an A-scan:

$$\text{axial digital resolution} = \frac{{\lambda_0}^2}{2\text{N}\delta\lambda} \tag{2.7}$$

where N is the total number of pixels of the detector. In order to generate high axial resolution OCT image, both high axial resolution and high axial digital resolution are required. High axial resolution can resolve small particles in the sample with a broadband light source and short central wavelength, while high axial digital resolution is needed to be able to display a small feature in the OCT image.

Lateral resolution

As in standard and confocal microscopy, the OCT lateral resolution is determined by the central imaging wavelength and the effective NA of the focusing lens. When the aperture of the imaging lens is properly filled, the lateral resolution can be calculated as the radius of the Airy disk at the focal plane:

$$\Delta\text{x (Lateral resolution)} = {}^{0.61\lambda}/_{NA} \tag{2.8}$$

High lateral resolution will compromise the depth of focus, which is defined as twice the Rayleigh length Z_r:

$$Focal\ Parameter = 2Z_r = \frac{\pi\Delta x^2}{\lambda} \tag{2.9}$$

As shown in Figure 2.3, an imaging lens with high NA generates higher lateral resolution, however, the depth of focus is limited due to the short Rayleigh range. In contrast, an imaging lens

with low NA yields more uniform lateral resolution over a larger depth range. New numerical defocus compensation methods, such as interferometric synthetic aperture microscopy, could refocus the light numerically to simulate large depth of focus while maintaining the high lateral OCT resolution. For *in-vivo* retinal imaging, the focusing of the imaging beam is done by the corneal curvature and the ocular lens. The ocular NA varies significantly between species and is fairly low (NA = 0.2) in dilated human eye, thus the lateral resolution is not expected to change significantly from the anterior retina to the choroid (distance of ~500 µm).

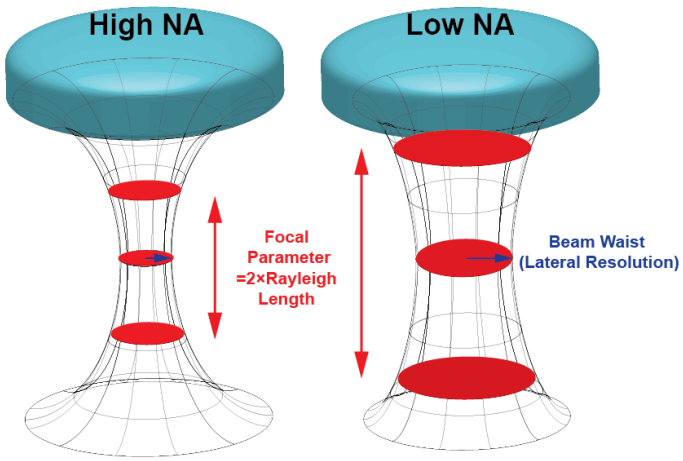

Figure 2.3 Samples to show the on focus imaging depth and lateral resolution with low NA and high NA optics

Depending on their intended application, OCT systems can be designed to operate at different spectral regions, for example, at ~800 nm, ~1050 nm, ~1300 nm and ~1700 nm central wavelength. Since both the axial and lateral OCT resolutions are wavelength dependent, a longer central wavelength will result in poorer spatial resolution.

In the case of retinal imaging, a parallel beam is delivered onto the cornea and the eye focuses the collimated beam onto the retina. Therefore, there choice for the spectral region of operation for a

retinal OCT system will be determined by a number of factors: 1. The maximum optical power that can be incident on the retinal surface without damage to the retinal tissue as determined by the ANSI; 2. The water absorption spectrum has two optical "windows" that correspond to minimal attenuation of the optical imaging power; 3. The optical transmission of ocular tissues which is determined by the wavelength dependent scattering and absorption properties of the cornea, the anterior chamber, the lens, the vitreous and the retina. Based on the aforementioned considerations, for this research project, a SD-OCT system operating in the 1060 nm spectral region was developed in order to utilize a local minimum in the water absorption spectrum, low scattering of the anterior part of the eye and improved transmission through the RPE, to allow for better penetration into choroid to visualize the choroidal vasculature. Another reason for selecting this central wavelength was to ensure that the OCT imaging beam will not stimulate visually the retinal photoreceptors and therefore will not corrupt the retinal function measurements.

Sensitivity (SNR)

Sensitivity in an imaging system is defined as the smallest signal that can be differentiated from the noise. SD-OCT has the advantage of significantly higher signal-to-noise ratio (SNR of 20 – 30 dB) compared to TD-OCT due to the fact that SD-OCT utilizes M number of detectors (pixels), while TD-OCT uses only 1 detector (or a pair of dual balanced detectors). Theoretically, the SNR of a SD-OCT system is M/2 times larger than the SNR of a TD-OCT system, where M is the pixel number of photodetector[81]. The factor of 2 is due to the conjugate symmetry of the Fourier transform. In a short noise limited SD-OCT system, the noise obeys the Poisson distribution and the theoretical SNR at zero delay can be simplified to

$$Sensitivity = \frac{\eta S t}{2e} \tag{2.10}$$

where η is the photodiode responsivity, S is the power reflected perfectly back from a mirror in the sample arm, *t* is the integration time for one A-scan, and *e* is the electronic charge. For simplicity, photodiode responsivity remains constant over different wavenumbers, whose typical value for silicon based photodetector in the near infrared region (NIR) is between 0.4 and 0.8, while for an InGaAs photodetector it is 0.7 - 0.85. According to the ANSI standard, the maximum permissible optical power incident on the rat's cornea is 1.8 mW. For that power level and at 92 kHz data acquisition rate of the InGaAs camera, the theoretical sensitivity of our 1060 nm SD-OCT system was evaluated to be ~106 dB. In practice, the value is somewhat smaller (5 dB to 10 dB) than the theoretical calculation because of factors such as room background illumination and intensity fluctuation of the light source.

2.1.2 Phase-resolved Doppler Optical Coherence Tomography

Doppler OCT, also called optical Doppler tomography, is an extension of standard OCT that can be used to visualize and measure blood flow in arteries and veins, analogues to Doppler ultrasound. The principle of Doppler OCT is based on measurement of the Doppler frequency shift between the incident optical beam and the backscattered light from moving particles, or more specifically the red blood cells in the blood vessels, as shown in Figure 2.4.

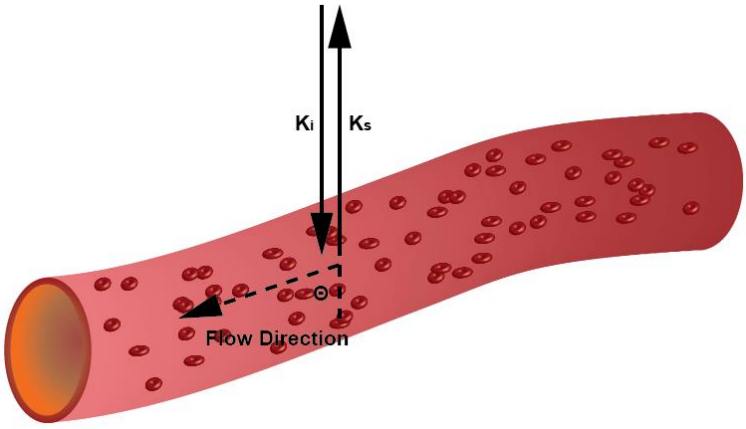

Figure 2.4 A schematic to show that the Doppler angle (Θ) is the angle between incident beam and the flow direction.

This Doppler frequency, f_D, is dependent on both the velocity of the moving particles (red blood cells) and the wavelength of the imaging beam:

$$f_D = \frac{1}{2\pi}(\boldsymbol{k_i} - \boldsymbol{k_s})\boldsymbol{v} \tag{2.11}$$

where $\boldsymbol{v}$ is the velocity vector of blood flow and k_i and k_s are the wavevectors of incident beam and backscattered light. Alternatively, this equation can be simplified to

$$f_D = \frac{2v_z}{\lambda} \tag{2.12}$$

where λ is the central wavelength and v_z is the blood flow velocity along the incident beam propagation $v_z = |\boldsymbol{v}|cos\theta$, as θ the angle between beam propagation and blood flow, also named Doppler angle. In phase-resolved OCT, the averaged frequency shift is the rate of phase change over time, and given the small time interval T between A-scans, $\Delta\theta$ becomes the phase difference between consecutive A-scans with high oversampling:

$$f_D = \frac{\partial \Delta\theta_{n,z}}{\partial t} \simeq \frac{\theta_{n+1,z} - \theta_{n,z}}{T} \tag{2.13}$$

Since the signal $\check{I}(z,n)$ in spatial domain is a complex number, thus it can be expressed as: $\mathrm{Re}\big(\check{I}(z,n)\big) + i\ \mathrm{Im}(\check{I}(z,n))$ where $\mathrm{Re}\big(\check{I}(z,n)\big)$ and $\mathrm{Im}\big(\check{I}(z,n)\big)$ are the real and imaginary part of $\check{I}(z,n)$. Then f_D becomes:

$$f_D = \frac{1}{2\pi nT}\tan^{-1}\frac{\mathrm{Re}\left(\check{I}(z+1,n)\right)\mathrm{Im}\left(\check{I}(z,n)\right) - \mathrm{Im}(\check{I}(z,n))\mathrm{Re}\big(\check{I}(z+1,n)\big)}{\mathrm{Re}\left(\check{I}(z+1,n)\right)\mathrm{Re}\left(\check{I}(z,n)\right) + \mathrm{Im}(\check{I}(z,n))\mathrm{Im}\big(\check{I}(z+1,n)\big)} \tag{2.14}$$

Substituting with equation 2.12, the velocity along the beam propagation, or axial velocity becomes:

$$v_z = \frac{\lambda}{4\pi nT}\tan^{-1}\frac{\mathrm{Re}\left(\check{I}(z+1,x)\right)\mathrm{Im}\left(\check{I}(z,x)\right) - \mathrm{Im}(\check{I}(z,x))\mathrm{Re}\big(\check{I}(z+1,n)\big)}{\mathrm{Re}\left(\check{I}(z+1,x)\right)\mathrm{Re}\left(\check{I}(z,x)\right) + \mathrm{Im}(\check{I}(z,n))\mathrm{Im}\big(\check{I}(z+1,n)\big)} \tag{2.15}$$

where moving particles perpendicular to the axial direction will not generate any Doppler frequency shift. The axial blood flow is the flow velocity integration over the cross-section of the blood vessel in an OCT B-scan. As various ocular diseases are associated with change of the retinal blood flow, such as glaucoma, AMD, DR, etc., absolute blood flow measurement is important. There are two basic approaches to determining the absolute blood flow with OCT. One is called *en-face* Doppler OCT and it in this case the absolute blood flow is determined as integration of the axial flow over the cross section of the blood vessel determined from an OCT C-scan[82]–[85]. Therefore, the absolute blood flow can be expressed as:

$$F = \iint_S |v|\, dS = \iint_{S_{en-face}} v_z\, dS_{en-face} \tag{2.17}$$

This method is Doppler angle irrelevant, therefore it is applicable to cases where the orientation of the blood vessel is difficult to identify. However, this method also has limitations: this method requires volumetric scan, so the motion artifact will affect the image registration.

Alternatively, precise knowledge of the Doppler angle between the OCT beam and the blood vessel is required for accurate assessment of the absolute blood flow by using point-scanning SD-OCT or swept source OCT systems. Pedersen et al.[86] proposed a method to separate the OCT. In this case, the absolute blood flow was calculated from 2 OCT B-scans acquired from the same location in the imaged object from two different probing angles sequentially. A dual-beam design[87]–[89] of the OCT imaging probe was used to detect the blood flow from different angles simultaneously, utilizing 2 identical detectors. Singh et al[90] extracted the Doppler angle from a reconstructed 3D volume by tracking the orientation of the blood vessels. The Doppler angle can also be simply extracted by taking two cross-sectional scans on blood vessels[91], [92], where the distance between these two scans are close enough to enable approximation of linear orientation of the blood vessels. This method does not require volumetric scans or complicated and expensive OCT system design. Furthermore, by acquiring concentric scans around the ONH, the total blood flow can be estimated.

2.1.3 Optical Coherence Tomography Angiography (OCTA)

OCTA is a dye-free method for generating angiograms of biological tissue. With the recent development of commercial OCTA instrument, over the past few years OCTA has found numerous

clinical ophthalmic application for investigation of the pathological changes in the retinal blood flow and blood perfusion associated with retinal diseases such as AMD, DR, glaucoma. Compared with the gold standard fluorescein angiography and ICG based angiography, OCTA does not require any intravenous injection of contrast agents, therefore the procedure is shorter and less invasive.

OCTA technologies enhance the contrast of moving particles from the static tissue by evaluating the temporal change of the OCT signal. An example of temporal OCT signal fluctuations measured from a blood vessel and static tissue is shown in Fig. 2.5. Based on the information type that it used for generating the OCTA images, methods can be divided into intensity-based, phase-based, and complex signal-based. Specifically, speckle-variance[93], [94] and phase-variance[95], [96] method calculate the temporal intensity and phase variance by acquiring multiple B-scans from the sample location. Jonathan et al.[97] and Chen et al.[98] calculated the cross correlation between adjacent B-scans, based on intensity signal of the image and the imaginary part of the image, respectively. Split-spectrum amplitude-decorrelation angiography[99] separates the full spectrum into several sub-spectra, and the angiogram is calculated by analyzing the flow images generated from the sub-spectra and repeated measurements from the same location. Similarly, the spatial angular compounded OCTA[100] splits the full incident beam into different angular components, and an angiogram is generated by analyzing the flow images from sub-angular components and repeated measurements from the same location. OMAG was proposed first by Wang et al.[59], and it simply uses the complex signal from an OCT image to calculate the absolute complex difference between adjacent repeated B-scans. As OCTA is a good tool to enhance the contrast of the flow in order to separate it from the static tissue, parametric OCTA uses the ratio between the

flow signal and the intrinsic signal to filter out the static tissue contribution with high intrinsic signal (e.g. skull). In this thesis, complex signal based OCTA was used for some of the animal studies because of its simplicity in terms of implementation and lower computational cost:

$$OCTA(x,y) = \frac{1}{n-1}\sum_{i=2}^{n}|S(x,y,i) - S(x,y,i-1)| \tag{2.18}$$

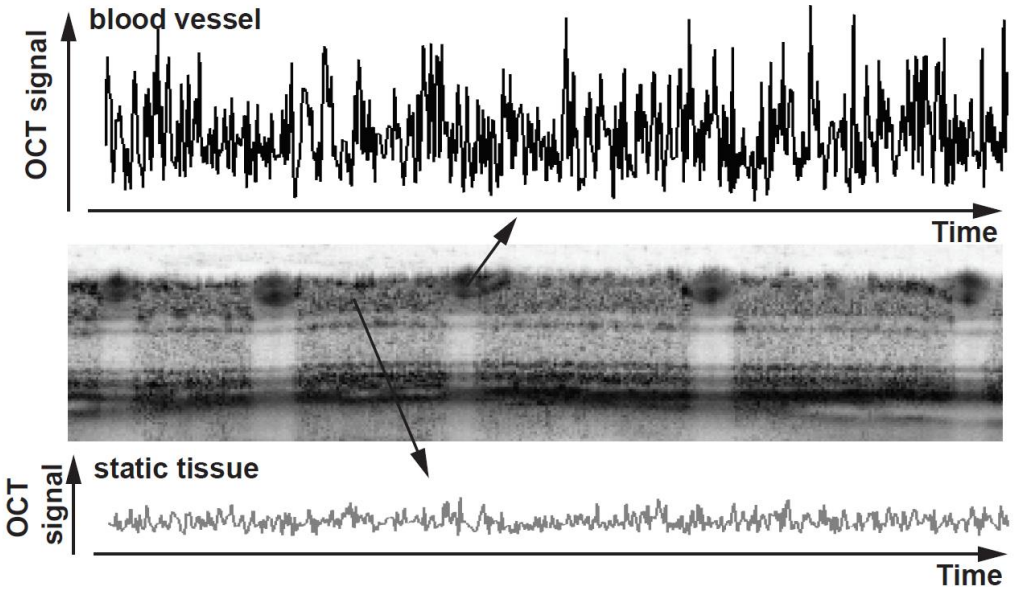

Figure 2.5 An example to show the difference of temporal OCT signal fluctuations between static tissue and a blood vessel.

2.2 ERG

ERG is an electrical method of recording electrical currents in the eye, generated when the eye is exposed to visual stimulation. This technology originated in 1865 when Holmgren found out that a light stimulus can trigger an electrical signal in the animal eye. Nowadays, ERG is an indispensable clinical method for evaluating the normal and abnormal retinal function in patients

with various retinal neurodegenerative conditions. It is also widely used in basic and clinical research to study the dysfunction of retinal cells *in-vitro* and *in-vivo* in animal studies.

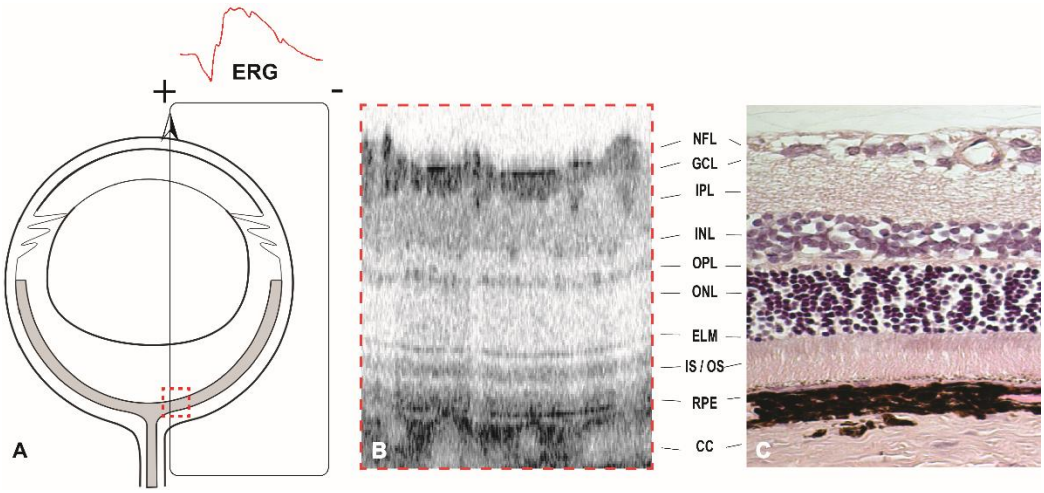

Figure 2.6 (A) A schematic to show how the extracellular ERG is recorded. "+" and "-" label the positive and negative electrodes, respectively, and the arrow represents the direction of current pathway. (B-C) Representative OCT B-scan and histology to show rat's retinal with distinctive layers.

As shown in Figure 2.6, when a photoreceptor in the retina is stimulated, it generates an electrical current to all the directions, associated with directional flow of Ca^{2+} and Na^{+} ions in the retinal tissue. Since the photoreceptors in vertebrate eyes are arranged in parallel and the ERG recording is associated with a massive number of stimulated photoreceptors, the horizontal electrical current is cancelled and only the radial current flows through the inner retinal cells, such as the retinal bipolar cells, Müller cells, amacrine cells, and RGCs, and reaches the vitreous. Then the radial current flows back through the choroid, sclera and the skin. ERG is recorded in a minimally invasive way by placing a positive electrode in the form of a loop or a tip on the corneal surface and attaching a reference electrode to the skin in the temples (human subjects) or inserting a needle behind the ear or in the tail. The ERG traces can also be recorded directly from the vitreous and

the retinal layers by inserting a needle electrode, however this method is more invasive. In this thesis, ERG traces were recorded *in-vivo* from rat eyes by placing a positive electrode in the form of a loop on the rat cornea, and negative and reference electrodes between and behind the ear respectively. The diameter of the loop electrode was sufficiently large to allow the OCT imaging beam to pass through the pupil and image the retina without any obstruction by the loop electrode.

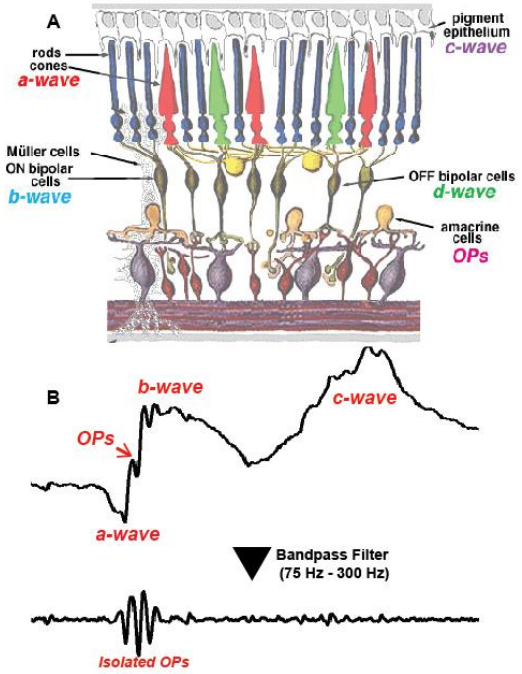

Figure 2.7(A) Origins of ERG components in retina. (B) A representative short duration flash ERG trace and its isolated OP with all the components labelled. D-wave is not shown as it can only be separated from long duration (>200 ms) ERG trace. (A) Reproduced with permission from [101], Copyright 2017 Webvision: Attribution, Noncommercial, No Derivative Works Creative Commons license.

It is important to note that the ERG traces correspond to integrated electrical signal that originates from different types of retinal cells. Because the temporal response of different retinal cells overall partially in time, one way to analyze and classify ERG traces is to characterize specific positive and negative peaks. For example, Ragnar Granit divided the typical ERG trace into three major

components, named PI, PII, and PIII, which correspond to a slow positive wave, a fast transition to a positive peak followed by a mediated positive amplitude wave, and a fast negative wave, respectively. The integrated signal from these three components displayed several distinctive peaks and oscillations. An ERG a-wave is defined as the first negative peak, and mainly reflects the response from photoreceptors (both rods and cones) in the posterior retina. The ERG b-wave is defined as the first positive peak, and its amplitude is usually defined as the voltage difference between a-wave and b-wave peaks respectively. B-wave is associated with the integrated response from several different types of cells in the retinal INL. Previous studies have shown the Müller cells and the ON bipolar cells contribute to the b-wave. OP is the high frequency oscillation observed between the a-wave and the b-wave in a typical ERG trace, and it originates from the amacrine cells located in the inner retina. The OP frequency ranges from 100 Hz to 150 Hz, and based on the latest ERG standard, it can be isolated with a bandpass filter (75 Hz – 300 Hz). The ERG C-wave is a slow positive wave that appears after the b-wave and originates from the RPE, located in the posterior retina. The C-wave is also associated with the regeneration of the photoreceptors. Lastly, the d-wave can only be identified in ERG traces when the stimulation is long (>100 ms). It appears after the end of the stimulation and is associated with the response of the OFF bipolar cell to visual stimulation. In this project, we used brief single flashes of <10 ms duration, or flicker stimuli of 1s or 2s total duration and 10 Hz frequency to study the functional retinal response therefore, the c-wave and d-wave will not be discussed in this thesis.

Chapter 3 The effect of acute IOP elevation to a moderate level on the rat retina morphology and function

Notes and Acknowledgement

This chapter summarizes results from a study that aimed to investigate changes in the retinal and ONH morphology measured with UHR-OCT and retinal function, measured with ERG, associated with acute elevation of the IOP to a moderate level of 35 mmHg in a rat model of glaucoma. The content of this chapter is based on the following journal manuscript:

Choh V, Gurdita A, **Tan B**, Prasad RC, Bizheva K, Joos KM. "Short-Term Moderately Elevated Intraocular Pressure Is Associated With Elevated Scotopic Electroretinogram Responses," *Investig. Opthalmol. Vis. Sci*. 2016;57(4):2140. doi:10.1167/iovs.15-18770.

Author contributions

Vivian Choh, **Kostadinka Bizheva** and **Karen M Joos** conceived the study and provided study materials.

Bingyao Tan collected the OCT images; **Bingyao Tan**, **Akshay Gurdita** and **Vivian Choh** collected the STR and ERG data.

Bingyao Tan wrote the algorithm for xBMO calculation.

Bingyao Tan and **Akshay Gurdita** analyzed the experiment data.

Ratna Prasad conducted the histology and immunohistochemistry.

Bingyao Tan, **Kostadinka Bizheva**, **Vivian Choh**, **Karen Joos** and **Akshay Gurdita** contributed to the interpretation of all results.

Vivian Choh wrote part of the first draft of the manuscript, while Bingyao wrote the "Methods" sections related to the OCT system description, OCT imaging protocol and OCT image analysis.

All authors contributed to the final version for publication.

3.1 Introduction

Glaucoma is a chronic disease that is characterized by progressive degeneration of the RGC axons within the optic nerve resulting in loss of RGCs and eventually blindness. It is the second leading cause of blindness worldwide, with an estimate of 64.3 million people between the ages of 40 to 80 years affected in 2013, 76.7 million by 2020, and 111.8 million in 2040.[102] According to a 2008 to 2009 survey by Statistics Canada, more than 400,000 people over the age of 45 in Canada have glaucoma[103]. Currently, there is no cure for glaucoma; patients can be treated only with medications or surgery to slow the progression of the disease. Therefore, early detection and early treatment are essential for managing the disease. High IOP remains a risk factor for open-angle glaucoma (OAG)[4], [104], [105], and, therefore, a target for early treatment. However, a confounding factor is that some patients acquire glaucoma even when their IOPs are normal (IOP < 21 mm Hg) during clinic examinations. Fluctuations in IOP may have a role in the development of glaucoma since multiple studies have demonstrated nocturnal IOP elevation[106]–[108] or elevations with inversion activities[109], [110]. Retinal changes evoked by chronic and acute models of IOP elevation are detectable using various components of the scotopic ERG[24], [53], [111], [112]. The information collected with full-field flash ERGs typically pertains to the photoreceptor and INL cell function. However, components of the scotopic ERG have been shown to reflect proximal retinal functions, including the negative and positive responses to very dim (typically near rod threshold) light stimuli that are too dim to elicit the b-wave; these components are conventionally called STRs[101], [113]. Joos et al.[114] demonstrated that controlled transient elevations of IOP in rats led to structural changes in the optic nerve that are similar to the early

damage observed in chronic glaucoma models but no information about retinal function was available. The present study was done to determine whether acute moderate increases in IOP can lead to glaucomatous damage and whether early changes in retinal function can be detected using various components of the scotopic ERG.

3.2 Methods

All procedures in this study were conducted in accordance with the Guidelines of the Canadian Council on Animal Care and conform to the ARVO Statement for the Use of Animals in Ophthalmic and Vision Research. All protocols were approved by the University of Waterloo Animal Care Committee and/or the Institutional Animal Care and Use Committee (Vanderbilt University).

3.2.1 Animals and anesthesia

Male Sprague-Dawley rats (11 weeks old, approximately 300 g) were obtained from Harlan Labs (Indianapolis, Indiana) and were fed ad libitum. The rats were subjected to a 12-hour light:12-hour dark cycle (maximum 257 lux for 3.5 hours a day) in the housing facility, for the duration of the study, and 1 week before the start of all experiments. Electrophysiological and morphologic tests were done in separate measurement sessions (Table 3.1): binocular STR and ERG (n = 7, Group I) recordings were collected during the first IOP elevation session, and sequential monocular ultrahigh resolution optical coherence tomogram (UHR-OCT) recordings (n = 6, Group II) were collected after two previous IOP elevation sessions, 2 days after the initial IOP elevation. Another group of rats underwent the same IOP-raising protocol as the rats used for OCT imaging, and their retinas were harvested either for histologic (n = 6, Group III) or for Western blot (n = 4, Group

IV) analysis.

All rats initially were anesthetized with 2.5% isoflurane in oxygen and maintained with approximately 2% isoflurane in oxygen. The body temperatures of the rats were maintained using heated platforms during anesthesia. Temperatures were monitored using a consumer digital thermometer placed under the abdomen, and breathing rate was assessed every 15 minutes. For all in vivo procedures, one drop 0.5% proparacaine hydrochloride (Alcaine, topical anaesthetic, #1001600; Alcon, Mississauga, ON, Canada) was applied to the eyes, followed by one drop of 0.5% tropicamide (pupillary dilator; Alcon). The rat corneas were lubricated with artificial tears throughout the duration of the experiments to ensure that the corneas stayed hydrated. Injections of 5 mL sterile saline (0.9% wt/vol NaCl in water) were administered subcutaneously approximately every 1.5 hours during the anesthesia to ensure proper hydration of the animals during the experimental procedures. Although isoflurane is known to reduce the electrophysiological responses when compared to ketamine:xylazine, Liu et al.[115] recently confirmed that it is possible to evoke STRs using isoflurane.

3.2.2 Protocol for dynamic IOP elevation

IOP was raised in one eye by placing an adjustable ligature around the eye anterior to the equator for 1 hour for each procedure[114]. The adjustable ligature consists of a 12-cm length of a medium-size vascular loop (Sentinal Loops; Sherwood-Davis and Geck, St. Louis, MO, USA) measuring 2.5 mm wide and 1.3 mm thick, which was inserted within plastic tubing with 3-mm internal diameter and 1.5-cm length. A light coating of silicone oil was applied to the vascular loop as needed to permit easy adjustment of the tubing and to produce the desired IOP elevation. Additional topical 0.5% proparacaine hydrochloride was applied to the right eye every 20 minutes

while the ligature was in place. The targeted IOP was 35 mmHg to represent an elevated but nonischemic level (Table 1). In the rat, an elevated IOP of 35 mm Hg is associated with an estimated 10% reduction in retinal blood flow, but not with a significant reduction in vessel diameter[116]. The fellow control eye for all rats was left untreated. The IOPs were measured using a rebound tonometer (Icare Tonolab; Icare Finland Oy, Helsinki, Finland). IOP was measured using the mean of 5 readings, which reported the best reproducibility indicator (Table 3.1). IOPs were monitored throughout the entire experiment and the loop adjusted when necessary.

Experiment	IOP Procedure	Treated eye IOP ± SD mmHg	Control eye IOP ± SD mmHg
STR	Pre	12.4 ± 1.5	13.1 ± 1.9
	During	39.7 ± 4.2	10.6 ± 1.1
	Post	8.9 ± 0.7	9.7 ± 0.8
ERG	Pre	12.4 ± 1.6	13.1 ± 2.1
	During	38.4 ± 2.7	10.4 ± 1.0
	Post	9.1 ± 0.5	9.8 ± 0.8
OCT	Pre	9.1 ± 0.6	9.4 ± 0.3
	During	32.1 ± 2.9	10.9 ± 0.6
	Post	6.3 ± 0.3	8.9 ± 0.7

Table 3.1 IOP values attained for each procedure.

3.2.3 STRs and ERG

Before electrophysiological testing, the animals were dark adapted for at least 12 hours before being transferred in lightproof boxes to the appropriate procedure room. All preparations were done under red illumination (631 nm, <10.9 lux). Anesthetized rats were placed onto a water-heated platform maintained at 38°C (TP650, HHP05; Gaymar, Orchard Park, NY, USA), located in a large box built for dark-adapting animals. The head of the rat was placed into a custom-made

head holder and held in place using Velcro straps. A nose cone attached to the head holder allowed continuous delivery of the isoflurane anesthetic to the rats while they underwent the STR and ERG recording procedures.

One drop of artificial tears (Refresh Tears; Alcon) was administered to each eye before placement of a custom-made monopolar silver–silver chloride circular loop electrode onto the limbus of each eye. Reference electrodes were placed under the skin just above the ears[117], such that the tip of electrode was approximately 2.5 mm away from the lateral canthi of each eye. The ground electrode was placed at the back of the head. A commercial handheld Ganzfeld stimulator (Espion Colorburst; Diagnosys LLC, Lowell, MA, USA) was placed immediately in front of each eye. Binocular STRs and ERGs were recorded before increasing the IOP, 45 to 50 minutes into the 1-hour raised IOP procedure, and 30 minutes after the loop removal. STRs were recorded from 7 rats over 500 ms at a 1 kHz sampling rate with the system's built-in filter of 0.3 to 30 Hz, similar to the protocol of Bui and Fortune[118]. Following 10 minutes in the light-proof box, the rats were exposed to binocular uniform flashes of light with step-wise increases in luminance. Twelve luminance levels were used for the STR recordings (-6.64 log cd·s/m^2 to -3.04 log cd·s/m^2), with each luminance level consisting of 60 one-millisecond white flashes, separated by a 2-second dark interval. STR protocols were identical for rats, regardless of the targeted IOP. ERGs were recorded from the same rats that underwent STR recordings (n=7) at a 2 kHz sampling rate with the built-in filter set to 0.3 to 500 Hz immediately following the STR luminance series, that is, within the 1-hour of IOP elevation. The ERG luminance series consisted of 14 single 1 ms white flashes (-2.79 log cd·s/m^2 to 1.46 log cd·s/m^2) that were separated by progressively longer dark intervals (10–95 seconds).

3.2.4 Ultrahigh-resolution optical coherence tomography (UHR-OCT)

Morphologic images of the retina were acquired in vivo (n=6 rats) using a research-grade UHR-OCT system designed and built by our group specifically for imaging of rodent retinas. In brief, the UHR-OCT system operates in the 1060 nm spectral range (Superlum Ltd., λ_c=1020 nm, Δk= 110 nm, P_{out}=10 mW). The UHR-OCT imaging probe consists of 3 broadband NIR achromat doublet lenses (f_1=10 mm, $Ø_1$=6 mm, f_2=60 mm, $Ø_2$=25 mm, f_3=30 mm, and $Ø_3$=25 mm; Edmund Optics, Barrington, NJ, USA) and a pair of galvanometric scanners (Cambridge Technologies, Bedford, MA, USA), and is designed to deliver a collimated infrared beam with 1.5-mm diameter and optical power of 1.7 mW to the rat cornea, thus providing approximately 3 µm axial and better than 5 µm lateral resolution in the rat retina at an imaging rate of 47,000 lines/second[119]. The digital axial resolution is 1.6 µm. For the UHR-OCT imaging procedure, the rats were placed onto a heated stage. The treated and untreated control eyes were imaged sequentially. The imaged eye was kept open using a custom-made lid retractor and artificial tears were administered every few minutes to keep the cornea hydrated. Three dimensional (3D) stacks of cross-sectional OCT images (1024 lines/frame × 1024 pixels/line) of the retina were acquired from an approximately 2×2 mm^2 area in the retina centered at the ONH. Pre loop UHR-OCT images were collected monocularly on the future control eye, followed by recordings of the future treated eye. The IOP was then raised in the treated eye and images from this eye were collected 30 minutes into the raised IOP procedure. Recordings for the control eye were collected immediately thereafter, while the loop still was on the treated eye. At the end of the 1-hour raised IOP procedure, the loop was removed and recordings for the control and then the treated eyes were likewise sequentially collected 30 minutes after the removal of the loop.

3.2.5 Histology and immunocytochemistry

Five days after the initial IOP elevation, the rats were killed, and then perfused with heparinized saline followed by 4% (wt/vol) paraformaldehyde (#158127; Sigma-Aldrich Corp., St. Louis, MO, USA) in PBS. Eyes were enucleated and the orientation of the globe was indicated using a suture at the nasal limbus. The globes were postfixed for 2 days in 4% (wt/vol) paraformaldehyde in PBS and then briefly stored in PBS.

The globes that were used for histologic analysis were embedded in paraffin. Eyes from all 6 rats were serially sectioned in the sagittal plane passing through the optic nerve at a thickness of 6 lm. Representative sections on either side of the optic nerve were stained with hematoxylin (SL90; Statlab, Lewisville, TX, USA) and eosin (C.I. 45380; EMS, Hatfield, PA, USA) for light microscopy. On other sections, also from either side of the optic nerve, antigen retrieval was performed using boiling citric acid treatment (1.8 mM citric acid, 8.2 mM sodium citrate) for 10 minutes. Sections were allowed to cool at room temperature for 30 minutes. Retinal sections were treated with 3% (vol/vol) hydrogen peroxide (20 minutes) to quench endogenous eroxidase and then additionally quenched in 0.3% (vol/vol) sodium borohydride (# S678-10; Fisher Scientific, Pittsburgh, PA, USA) in PBS for 30 minutes before placing them in 5% (vol/vol) normal goat serum in PBS (1 hour) to prevent nonspecific binding. Two primary antibodies were used: rabbit polyclonal anti-poly (ADP-ribose) polymerase (PARP) p85 fragment (1:100; #G7341, Promega, Madison, WI, USA) to evaluate for apoptosis, and rabbit monoclonal anti–microtubule-associated protein light chain 3 (anti-LC3A/B [N-terminus]; 1:100; #MABC176, Millipore, Billerica, MA, USA) to evaluate for autophagy. All sections were incubated with primary antibody overnight at 48C before incubation with Cy3-conjugated AffiniPure Goat Anti-Rabbit IgG (1:200; #111-165-

144, HþL chains; Jackson Immuno-Research Laboratories, Inc., West Grove, PA, USA) at room temperature for 1 hour. Sections then were rinsed in water and allowed to air dry before mounting with Aqua-Poly/Mount (#18606-20; Polysciences, Inc., Warrington, PA, USA) under a coverslip. Retinal sections were examined using a Zeiss LSM510 Meta confocal microscope (Carl Zeiss Meditec, Jena, Germany).

3.2.6 Analysis of STR and ERG data

The positive STR (pSTR) amplitude was considered to be the peak positive change in voltage from the baseline voltage to the first peak in the STR recording. Since we were interested in RGC function, we examined pSTRs, which are considered to involve RGCs[120], [121]. We did not examine negative STRs (nSTRs), since they were not consistently present in the records and more likely involve amacrine cells[120], [121]. An absence of nSTRs also has been observed in other rodent studies[115], [122]. For ERG traces, a-wave amplitudes were measured as the maximum change in voltage from the baseline to the first negative trough, while b-wave amplitudes were measured as the change in voltage from the a-wave to the peak positive change following the a-wave. For all three measures (pSTR, a- and b-waves), implicit times were measured from the light stimulus onset to the peak amplitude. A few of the ERG recordings were noticeably translated by the recording system, where the beginning of the waveforms were not recorded until just before the a-wave appeared, indicating a failure in the trigger timing of the recording software. However, the intervals between the a- and b-waves, as well as their amplitudes were unaffected, therefore, only the implicit times for ERGs that were improperly recorded were adjusted. For each shifted ERG recording, the a-wave implicit time was matched to the average of those recordings at the same luminance level, same IOP state, and same eye (n=6). The rest of the waveform was shifted

by the same correction factor. Oscillatory potentials (OPs) were isolated from ERG recordings by applying a customized SigmaPlot bandpass filter (100–300 Hz). For each recording, the RMS value for the OP amplitudes were determined for a 60 ms window starting from the a-wave implicit time.

3.2.7 Analysis of UHR-OCT data

Cross-sectional images of the retina were generated from the raw morphologic UHR-OCT data using a custom MATLAB based software (Mathworks, Natlick, MA, USA). Three-dimensional reconstruction of the cross-sectional images (Amira; FEI Company, Hillsboro, OR, USA) was used to generate a 3D view of the imaged retinal area at and around the ONH. The unique pattern of the surface retinal blood vessels was used as a marker to align all 3D image data sets acquired before, during, and after IOP elevation to allow for direct comparison of the morphologic changes in the rat retina at all the time points of the study. By collapsing the 3D image to a 2D *en-face* projection image, and fitting the end points of the Bruch's membrane at the ONH with an ellipse, we were able to determine the center of the ONH in a consistent manner for image data sets acquired at different time points of our study. For our analysis, we considered the end points of the Bruch's membrane to be the points at which the Bruch's membrane/RPE interface terminates on either side of the optic nerve in a cross-sectional image[9], [123]. Once the ONH center was determined, the B-scan passing through it was used for the calculation of the cross-sectional Bruch's membrane opening (xBMO) depth, defined here as the average depth orthogonal to the plane connecting Bruch's membrane/RPE interfaces at the edges of the cross sectional image (Fig. 3.1). Cross-sectional BMO depths were analyzed as a function of loop wear by the same two

experimenters for all images.

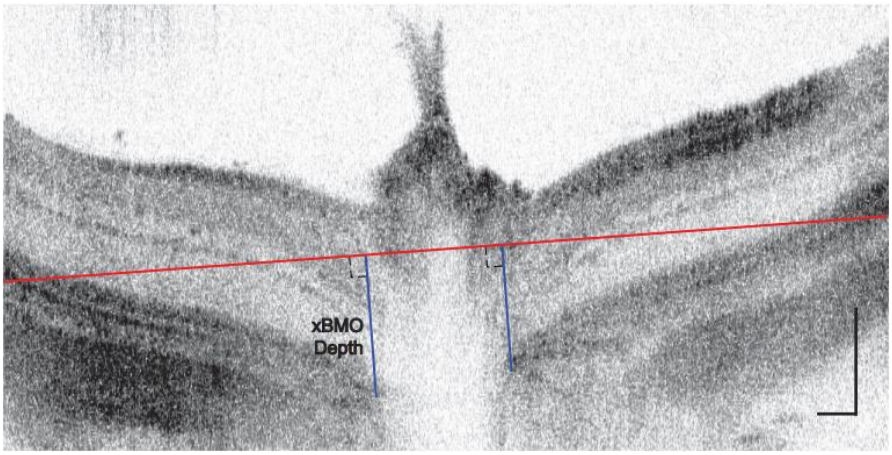

Figure 3.1 Representative ONH-centered B-scan demonstrating the method used to determine cross-sectional, xBMO depth. Each xBMO depth (blue line) was determined relative to the orthogonal plane connecting Bruch's membrane/RPE interfaces at the edges of the cross- sectional image (red line) and averaged. Vertical and horizontal scale bars = 100 µm.

3.2.8 Statistical Analysis

For all data, 2-way repeated-measures ANOVA (Statistica 8.0, Statsoft, Boston, MA, USA) was used to determine differences in the amplitudes, implicit times, and xBMO depths, with the eye used (treated versus control) as one factor and the loop condition (pre-, during, and postloop wear) as the second factor. Interaction between the two main effects also was tested. Greenhouse-Geisser corrections were used for epsilon values less than or equal to 0.75. Bonferroni-corrected multiple comparison tests were used post hoc to determine any differences between the loop conditions. For all tests, differences were considered significant for $P < 0.05$. All means are reported with the SD unless otherwise noted. For all tests, differences were considered significant for $P < 0.05$. All means are reported with the SD unless otherwise noted.

3.3 Results

3.3.1 STR and ERG amplitudes

Peak amplitudes and implicit times were measureable from the STR recordings (Fig. 3.2A) elicited with luminance levels greater than -4.24 log cd·s/m^2; responses were most consistently observed for pSTRs elicited by the highest stimulus luminance (-3.04 log cd·s/m^2). Although there were exceptions among the individual eyes, higher stimulus intensities were, on average, associated with higher pSTR amplitudes ($P<0.0001$). Loop-associated elevations in pSTR amplitudes were consistently observed at luminances greater than -4.24 log cd·s/m^2. Increasing the IOP led to enhancement of the pSTR peak amplitudes (Figs. 3.2A, 3.2B). In treated eyes, the mean pSTR amplitudes (±S.D.) during loop wear (86.4 ± 51.9 µV) were significantly higher ($P<0.0001$) than those before loop wear (7.9 ± 5.1 µV) and higher ($P<0.0001$) than those after loop removal (20.5 ± 11.3 µV). Positive STR amplitudes before and after loop wear were not significantly different ($P=1.000$). No differences in pSTR amplitudes were detected in the control (untreated eyes) as a function of loop wear ($P=1.000$ for all comparisons), indicating an absence of an IOP-associated fellow eye effect. Pre- and postloop pSTR amplitudes were not statistically different between the treated and control eyes before loop placement (7.9 ± 5.1 vs. 8.1 ± 6.1 µV, respectively, $P=1.000$) or postloop placement (20.5 ± 11.3 vs. 11.3 ± 6.4 µV, respectively, $P=1.000$). However, during loop wear, the pSTR amplitudes were higher in the treated eyes than in the control eyes (86.4 ± 51.9 vs. 9.3 ± 5.2 µV, respectively; $P<0.0001$; Figs. 2A, 2B). In the treated eyes, implicit times during loop wear (131.8 ± 16.6 ms) were longer than those during the pre- (112.4 ± 13.4 ms; $P < 0.0001$) or postloop (118.9 ± 16.2 ms; $P<0.0001$) conditions (Fig. 3.2B, inset). Moreover, differences were detected between the preloop and postloop conditions in these treated eyes

(P=0.0299). Within the control eyes, no implicit time differences were detected as a function of loop wear (P=1.000 for all comparisons). Like the patterns observed for the pSTR amplitudes, the implicit times were similar between the treated and control eyes for the preloop (112.4 ± 13.4 vs. 113.8 ± 14.9 ms, respectively, P=1.000) and post loop (118.9 ± 16.2 vs. 116.5 ± 16.5 ms, respectively; P=1.000) time-points. However, implicit times were longer for treated eyes than control eyes (131.8 ± 16.8 vs. 115.3 ± 19.5 ms, respectively; P<0.0001) during loop wear.

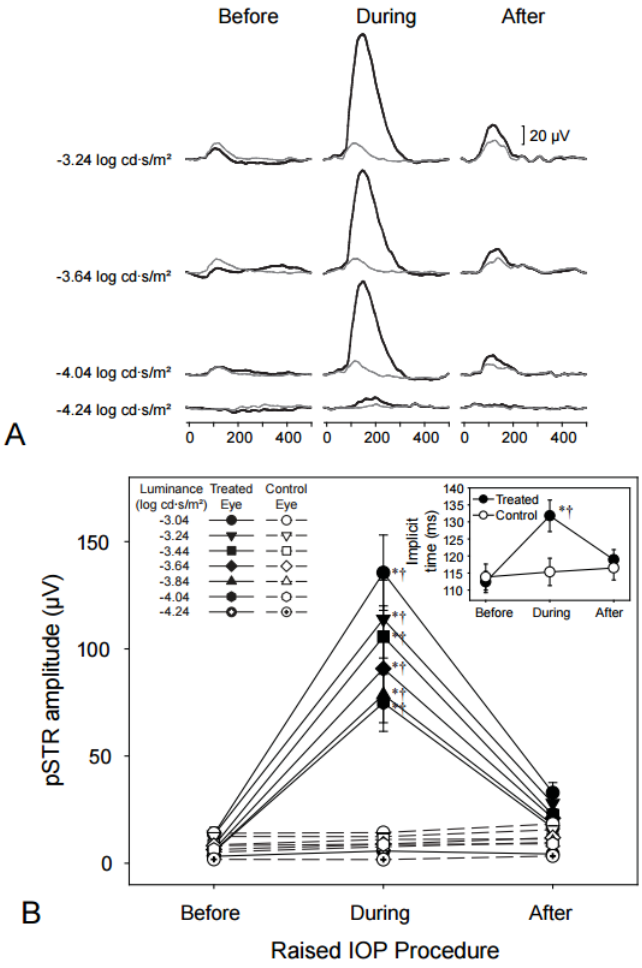

Figure 3.2 (A) Sample STRs from a treated eye (thick black lines) and its control eye (thin grey lines) prior to, during, and following 35 mmHg IOP elevation. (B) Mean pSTR amplitudes ± S.E. of STRs for the treated eyes (filled symbols) and control eyes (empty symbols) during the various stages of loop-wear. STRs were evident at flash intensities greater than -4.24 log cd·s/m² up to -3.04 log cd·s/m². Inset: Mean implicit times ± S.E. of the treated (filled symbols) and control (empty symbols)

eyes during the various stages of loop-wear. Asterisks (*) denote significant differences (P < 0.05) relative to the respective pre-loop condition. Daggers (†) represent differences (P< 0.05) between eyes for the specific loop condition. Please refer to text for overall and all other comparisons.

All ERG waveforms consistently showed a- and b-wave amplitudes and OPs on the rise of the b-wave at luminances greater than -0.54 log cd·s/m^2 (Fig. 3.3A). Like the pSTRs, amplitudes generally were greater with higher luminance levels (P=0.0011) and during elevated IOP (Figs. 3A–C). Specifically, a-wave amplitudes during loop wear (-228.4 ± 29.7 µV) were significantly greater in magnitude than those during the preloop (-31.4 ± 9.9 µV; P<0.0001) and postloop (-49.0 ± 12.6 µV; P<0.0001) conditions (Fig. 3.3B). Similarly, b-wave amplitudes during loop wear (747.9 ± 74.5 µV) were significantly greater than those before (123.8 ± 29.0 µV; P<0.0001) and following (200.0 ± 56.0 µV; P<0.0001) loop wear (Fig. 3.3C). In the treated eyes, there were no differences between the pre- and postloop conditions in the a-wave amplitudes (P=0.4602), but b-waves amplitudes during postloop condition were greater than those before loop wear compare 200.0 ± 56.0 vs. 123.8 ± 29.0 µV, respectively; P=0.0081). The enhanced a-wave and b-wave amplitudes in the treated eyes were significantly greater than those in the control eyes (P<0.0001 for both; Figs. 3B, 3C). A- and b-wave amplitudes in control eyes did not differ as a function of contralateral loop wear (P=1.000 for both ERG components). A-wave implicit times also were longer during loop wear (31.6 ± 2.4 ms) than those during preloop (27.8 ± 2.6 ms; P<0.0001) and postloop (27.8 ± 1.8 ms; P<0.0001) conditions (Fig. 3.3B, inset). Similarly, b-wave implicit times were also longer during loop wear (78.9 ± 5.6 ms) than those during pre- (68.9 ± 5.6 ms; P<0.0001) and postloop (73.5 ± 5.2 ms, P=0.0223) conditions (Fig. 3.3C, inset). There were no differences between pre- and postloop a-wave implicit times (P=1.000), however, b-wave implicit times for postloop conditions were longer than those for preloop (73.5 ± 5.2 vs. 68.9 ± 5.6 ms respectively;

P=0.0247) conditions. Implicit times during loop wear for a- and b-waves were greater than control eyes (31.6 ± 2.4 vs. 28.5 ± 2.0 ms, P=0.0008 for a-waves; 78.9 ± 5.2 vs. 72.5 ± 3.8 ms, P=0.0054 for b-waves; insets of 3B and 3C). For both a- and b-wave implicit times, control eyes did not change for all comparisons (P>0.1275). Oscillatory potential amplitudes were greater in the treated eyes during loop wear (Fig. 3.4A) and the RMS values the OPs during IOP elevation (33.1 ± 10.1 µV) increased significantly compared to pre- (7.0 ± 1.3 µV; P<0.0001) and postloop (8.4 ± 2.9 µV; P<0.0001) wear conditions (Fig. 3.4B). For treated eyes, pre- and post-RMS values did not significantly differ (P=1.000). RMS values did not change for control eyes for all loop conditions (P=1.000).

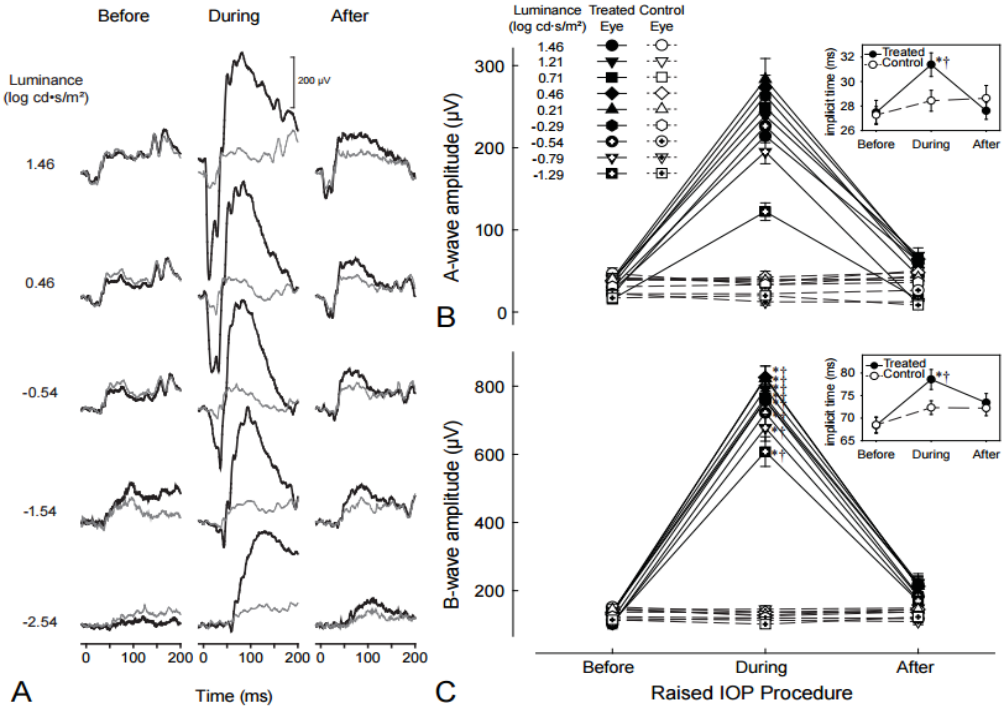

Figure 3.3 (A) Sample ERG from a treated eye (thick black lines) and its control eye (thin grey lines) prior to, during, and following 35 mmHg IOP elevation of the treated eye. Enhanced responses occur with IOP elevation. (B) Mean peak amplitudes ± S.E. of the a-waves and (C) b-waves for the treated eyes (filled symbols) and control eyes (empty symbols) during the various stages of loop-wear. Inset: Mean (B) a-wave, and (C) b-wave implicit times ± S.E. of the treated (filled symbols) and control

(empty symbols) eyes during the various stages of loop-wear. Asterisks (*) denote significant differences (P<0.05) relative to the respective pre-loop condition. Daggers (†) represent significant differences (P<0.05) between eyes for the specific loop condition. Please refer to text for overall and all other comparisons.

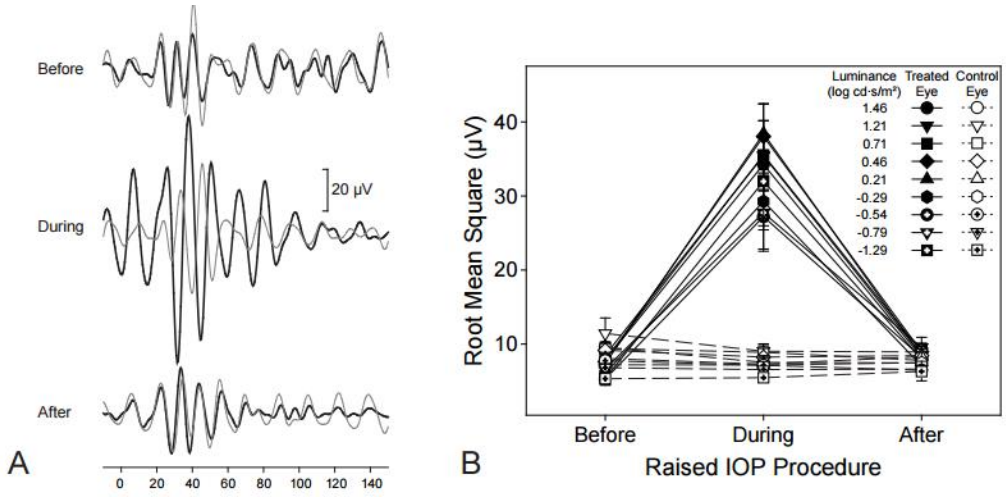

Figure 3.4 (A) Sample OPs (isolated via a 100-300 Hz bandpass filter) from a treated (thick black lines) and its control (thin grey line) eye prior to, during, and following 35 mmHg IOP elevation of the treated eye at a luminance of 2.88 log cd·s/m². (B) Mean RMS values ± S.E. for OPs prior to, during, and following 35 mmHg IOP elevation of the treated (filled symbols) and control (empty symbols) eyes. Please refer to text for comparisons.

3.3.2 Morphology changes (both OCT and histology)

Ultra-high resolution OCT imaging indicated that IOP elevation had an effect on physiological cup morphology; 3-D and 2-D cross-sectional images of the ONH indicated a ‘‘backward bowing"[124], [125] of the retina (Fig. 3.5). The xBMOs during IOP elevation (147.1 ± 30.3 µm) were significantly deeper than before loop wear (59.5 ± 25.0 µm, P=0.0134, Table 3.2), but not significantly deeper compared to postloop wear (80.9 ± 16.1 lm; P=0.0701). However, pre- and postloop xBMO depths for the treated eye also were not significantly different (P=1.000), indicating a partial recovery after 30 minutes of the xBMO depths to their preloop values. The xBMO depths during IOP elevation were greater in the treated eye compared to depths in the

control eyes (compare 147.1 ± 30.3 vs. 67.3 ± 11.2 lm, respectively; P=0.0238, Table 3.2), while preloop xBMO depths between the eyes were similar (treated versus control, 59.5 ± 24.9 vs. 68.0 ± 38.6 µm; P =1.000, respectively). The control eye xBMO depths did not change as a function of contralateral eye loop wear. Hemotoxylin and eosin (H&E) staining of retinal sections revealed no apparent differences (Figs. 3.6A, 3.6B) between the treated and control eyes. An absence of a difference between the eyes also was noted for specific cell death markers in the retinas. While the retinas of the treated and control eyes were moderately labelled with anti-LC3A/B, an autophagy marker, in many of the cells within the GCL, and in the IPL and OPL, there appeared to be no difference in the intensity or location of labeling between eyes (Figs. 3.6C, 3.6D). Similarly, no differences were detected between the control and treated eyes for poly (ADP-ribose) polymerase (PARP) p85 fragment (Figs. 3.6E, 3.6F), a marker for apoptosis. Fragment-labeling of PARP p85 was absent in the inner retina of the treated and control eyes, and labeling resembled that of the negative control (Fig. 3.6G). A positive early glaucoma control for PARP p85 fragment shows that this marker localizes to the cytoplasm of cells in the GCL (Fig. 3.6H; Joos, unpublished data). Thus, the analysis using immunocytochemistry indicated that short-term IOP did not result in apoptosis within 5 days of the initial IOP elevation.

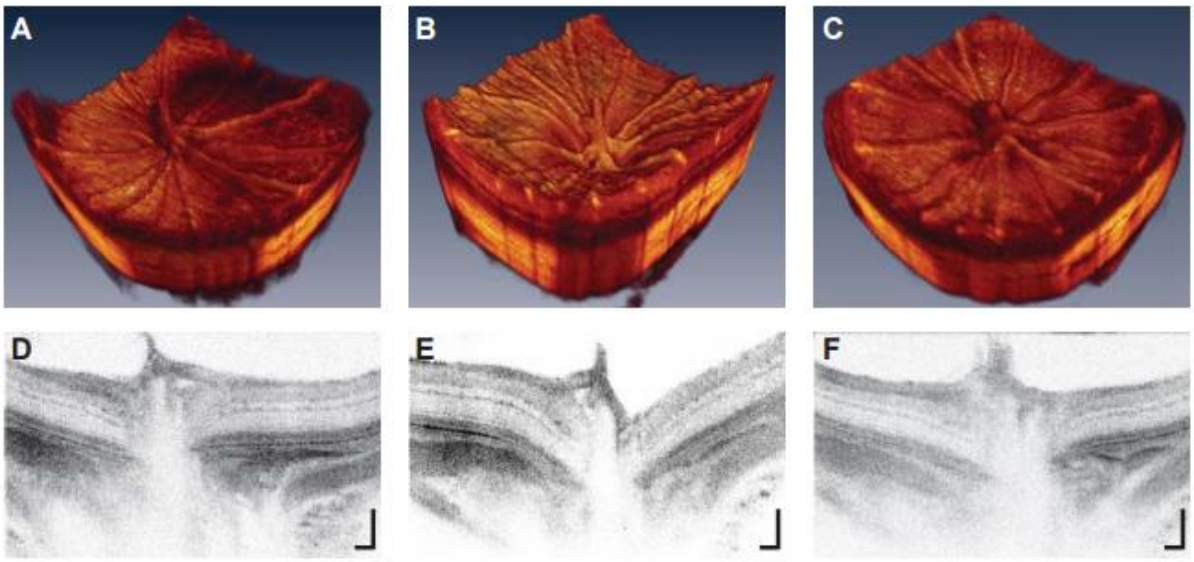

Figure 3.5 OCT images of the treated eye (A, D) prior to, (B, E) during and (C, F) following loop-wear centered about the ONH. Note "posterior bowing" of the ONH in both the (B) three dimensional and (E) cross-sectional images. 2-D image scale bars = 100 µm.

IOP Procedure	Treated eye BMO Depth ± SD	Control eye BMO Depth ± SD
Pre	59.5 ± 24.9 µm	68.0 ± 38.6 µm
During	147.1 ± 30.3 µm *†	67.3 ± 11.2 µm
Post	80.9 ± 16.1 µm	68.4 ± 19.8 µm

Table 3.2 Mean Bruch's membrane opening (BMO) depth derived from morphological OCT images of rats *in vivo*. Asterisks (*) denote significant differences ($P < 0.05$) relative to the respective pre-loop condition. Daggers (†) represent differences ($P < 0.05$) between eyes for the specific loop condition. For more comparisons, please see text.

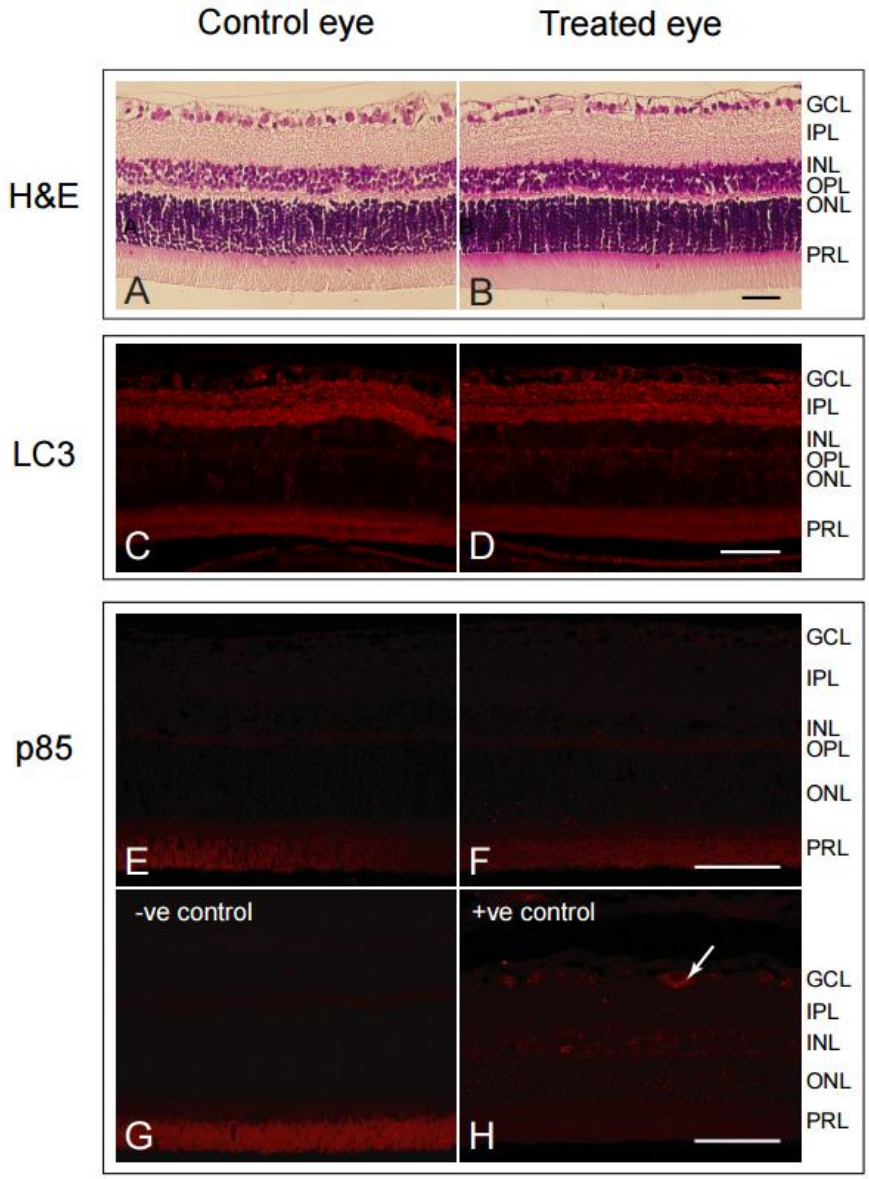

Figure 3.6 Histological cross-sectional images of the retina from (A) a control and (B) a treated eye. No gross differences in the retinas were observed. Scale bars = 50 µm. Micrographs of retinas from (C) a control and (D) a treated eye labelled for LC3A/B. LC3A/B was detected in the GCL, IPL, and OPL. No differences in the labelling were detected. Autofluorescence was present within the photoreceptor layer (PRL) as demonstrated by the primary antibody negative control (not shown). Scale bar = 50 µm. Micrographs of retinas from (E) a control and (F) a treated eye labelled for poly (ADP-ribose) polymerase (PARP) p85 fragment. Only autofluorescence was detected within the photoreceptor layer, as demonstrated by the primary antibody negative control (G). A positive control from a 6-week intermittently elevated IOP glaucomatous rat {unpublished data from Joos et al. \, 2010 #90} shows the PARP p85 fragment in the cytoplasm of an apoptotic cell in the RGC layer (arrow) (H). Scale bar = 50 µm.

3.4 Discussion

This study was done to determine whether early changes to retinal function in response to acute moderately-raised IOP was detectable electrophysiologically and morphologically. In eyes with IOPs elevated to approximately 35 mm Hg, the pSTR and ERG a-wave and b-wave amplitudes were increased compared to those before loop wear, and also compared to the control eyes (Figs. 3.2, 3.3). Other investigators typically show reductions in the ERG and pSTR amplitudes, usually at IOPs greater than 50 mm Hg, with a consistently low amplitude starting at approximately 80 mm Hg and above[53], [112]. Our study examined acute, nonischemic moderate levels of IOP that were elevated using a vascular loop, while most other studies use cannulation into either the anterior or vitreous chamber[53], [126]. The increase, rather than decrease, in pSTR amplitude that we observed in this experiment is likely related to the moderate level of IOP and cannot be related solely to the use of the vascular loop to increase IOPs, as opposed to IOP elevation based on cannulation or microbead injections. Using the same STR protocols, pilot data indicated that pSTR amplitudes were unaffected when the loop was on the treated eye without an increase in IOP (Fig. 3.8A). However, when IOP levels were elevated with the vascular loop to ischemic levels (80 mm Hg), at which blood flow and vessel diameter decrease by 80%[116], a severe reduction, rather than an increase, in the pSTR amplitudes was observed (Fig. 3.8B), a finding that is similar to the results presented by Bui et al.[112], who show an inflection point at 80 mm Hg, IOPs above which result in all ERG components (except for the a-wave) unable to ‘‘with- [stand] this pressure level."[112] It also should be noted that in other studies examining the incremental effects of acutely elevated levels of IOPs on the pSTR amplitudes, the data for IOPs at or below 30 mm Hg imply slight increases in pSTR responses[53], [112] despite the difference in method of IOP

elevation. Given that the rats were anesthetized with ketamine, the increase in the pSTR amplitudes that was observed in these studies suggest that the increase in amplitudes in our study are independent of the anesthetic used. Finally, the different rat strains used in other studies may also be a contributing factor when comparing our study to previously published literature.

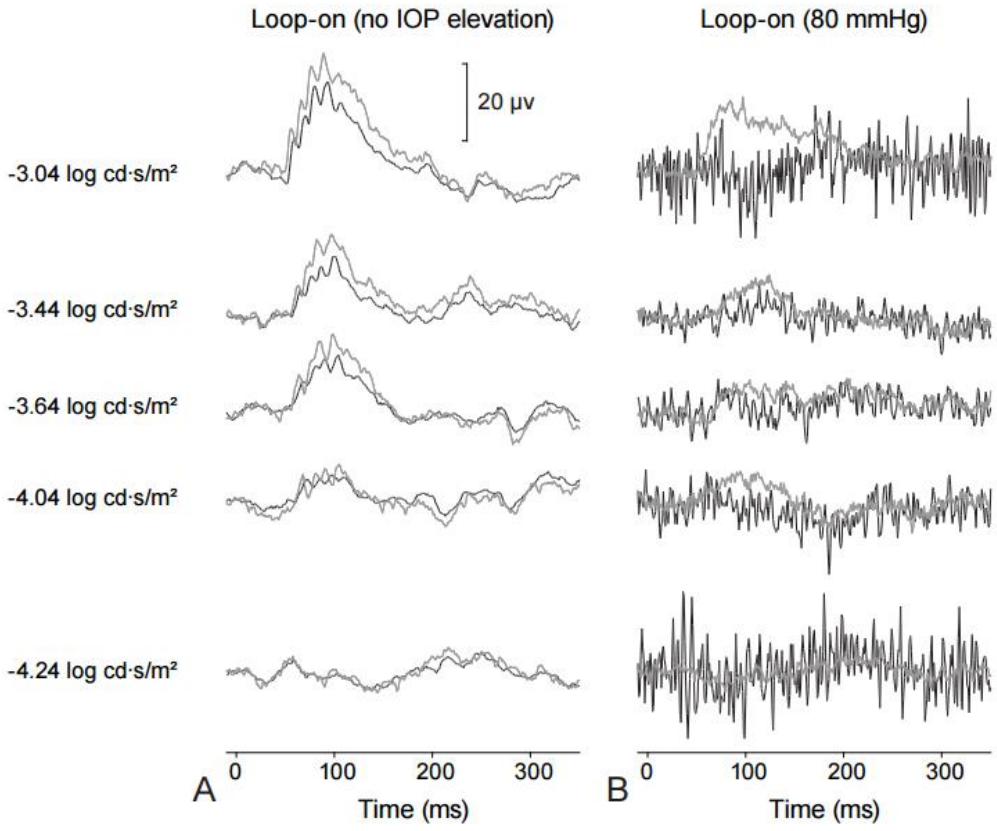

Figure 3.7 STRs during loop-wear in the treated (thick black lines) and control (thin grey lines) eyes (A) with no increase in IOP (10 mmHg) and (B) at 80 mmHg.

It is possible that using the vascular loop might change the global shape of the eye with backward bowing and, therefore, potentially affect the signals received at the cornea. However, as observed by Westall et al.[127], reductions rather than the observed increases in ERG amplitudes would be expected for longer eyes, while enhancement of the signal would be expected for shorter eyes. The

posterior bowing of the retina observed in our experiments, must be related, at least in part, to the increase in IOP. Backward bowing of the posterior pole following IOP elevation has been known for decades and for a number of structures, including the optic disc in infant humans[128], the retina in rats[116], the retinal pigment epithelium Bruch's membrane[124] in primates, and the lamina cribrosa in primates[9] and humans[129]. While most of these studies involve cannulation of the anterior chamber[60], [116], [124] or vitreous chamber[129], [130] as the means of elevating IOP, Gramlich et al.[76] qualitatively showed that posterior bowing deepened with increasing levels of IOP in rats whose IOPs had been raised using a loop around the equator of the eye, and Ivers et al. [15] showed deepening of the anterior lamina cribrosa surface following laser treatment of the trabecular meshwork in rhesus monkeys. The xBMO depth changes observed in our study are comparable to those of the aforementioned investigators. Although morphologic responses were measured in rats with IOPs raised before the final assessment, our acute, moderately-elevated IOP model revealed no changes to cell death marker levels in the treated eyes relative to the control eyes (Figs. 6, 7). This result is consistent with an acute, nonpathologic response, despite IOP elevation for the prior 2 sessions. These markers are important because their presence has been reported in previous investigations that are more chronic in nature[131]. It is probable that additional IOP elevations over longer periods of time would lead to effects on the xBMO depths; however, the finding that the control eye preloop xBMO depths (from eyes that had no IOP elevation) were not different from the treated eye preloop xBMO depths (IOPs had been elevated before the UHR-OCT imaging session; Table 5.2) would seem to indicate that the eye can tolerate a small number of IOP elevations. Elevation of the a-wave, b-wave, and OPs in the scotopic ERG implies that the outer retina also is affected by moderately elevated IOP. Electrophysiology has

demonstrated reduction of these components in animal models with chronic ocular hypertension (OHT) including Swiss mice with histologic abnormalities of rod bipolar and horizontal cells.39 DBA/2NNia mice with thinning of the GCL, IPL, OPL, and rods[132], and DBA/2J mice with synaptic abnormalities of outer retinal cells[133]. In humans with advanced glaucoma, reductions in scotopic ERG amplitudes for the a-wave[134], b-wave[134], [135], and OPs[135], [136] have been reported, as well as loss of the positive peak of the STR[134], and reduced focal ERG amplitudes[137].

Chen et al.[138] have suggested that a decrease in b-wave ERG amplitudes are indicative of ischemia but supranormal ERGs also are suggestive of pathology, rather than a normal variant.47 Supranormal scotopic a-wave and b-wave amplitudes with normal implicit times have been noted in specific conditions, including loss of retinal dopaminergic amacrine cells[139], [140], blockage of retinal dopamine receptors[141], [142], gestational low level lead exposure in rats[143] and humans[144], loss of a mitochondrial ATP transporter in Ant1/mice[145], and in a microbead occlusion mouse model, with an approximate 20%increase in b-wave amplitude present up to 48 weeks with a 3 to 5 mm Hg mean IOP elevation[111], [146]. Supranormal a-wave and b-wave scotopic and photopic ERGs with shortened implicit times also have been found in the Fat-1 mouse with deletion of n-6 and accumulation of n-3 fatty acids in the retina[147], and amplitudes were likewise increased with implicit time variance in the <6-week-old retinopathy, globe enlarged (rge) chicks[148], whereas the scotopic b-wave is supranormal with prolonged implicit times in a human cone dystrophy with a genetic mutation in the KCNV2 potassium channel gene[149]. While we are not certain what mechanism is responsible for the increase in the amplitudes of all the electrophysiological signals, studies by Ward et al.[150] showed an approximately 2-fold increase

in the spontaneous firing of excitatory signals in RGCs following IOP elevation by microbead injection into the anterior chamber of mouse eyes compared to eyes that had been injected with saline only. The increased retinal activity was postulated to be mediated by the transient receptor potential vanilloid family of cation channels that is activated in response to IOP-associated stress[150]. The enhanced pSTR amplitudes that were observed in the present study may reflect a similar elevated IOP-induced increase in RGC electrical activity.

Nitric oxide (NO) is another possibility for a rapidly acting agent that can mediate the increase in electrophysiological signals that we observed. Vielma et al.[151] showed that low level intravitreal injections of NO donors into rat eyes were associated with increases in the amplitudes of ERG a- and b-waves, OPs and pSTRs. These enhancements were reversible, with ERG amplitudes decreasing to match those recorded before the exogenous NO injections. Nitric oxide has a role in basic physiological functions such as visual signal processing in the inner retina and in photoreceptors[152]–[158], but it also has been associated with dysfunctional retinas of various mammalian species[159]–[164]. Several investigators have shown that chronic elevation of IOP to less than 35 mm Hg in the rat eye is associated with NO production in the retina[165], [166] and the optic nerve[167], [168]. An acute increase in IOP to 35 mm Hg potentially could increase NO levels, which presumably would lead to an enhancement of the electrophysiological responses. The finding that pathologic markers were not enhanced in this study following acute elevations of IOP (Figs. 6, 7) supports the idea of a physiological, rather than pathologic, response to the mechanical stress associated with a short-term moderate IOP elevation. Alternatively, pathologic changes may not have been captured, given the relatively short time course of the experiment.

We also note that should a biochemical factor be responsible for mediating the enhanced pSTR

and ERG amplitudes, the factor appears to be transient. Although postloop responses were not significantly different from those before loop wear, the means were slightly higher after loop removal (Figs. 2, 3), suggesting that electrophysiological responses were collected before retinas could fully recover to their preloop physiological state. We also have observed that the pSTR amplitudes 45 to 50 minutes after loop removal, which is longer than the 30 minutes we used for this experiment, return to those of the preloop conditions (data not shown).

3.5 Conclusion

In summary, our results indicated measurable changes in the physiological response of retinal cells to visual stimuli during acute moderate IOP elevation using a vascular loop. Our study showed that IOP elevation to 35 mm Hg in the rat is associated with an increase in the electrophysiological response as well as a backward bowing of the ONH. The electrophysiological responses observed may have been mediated by transient biochemical factors released in response to the elevated IOP. The ability to observe changes in electrophysiological and morphologic responses with UHROCT might present a model for detection of moderate, fluctuating IOP elevations. Further work is required to fully understand the mechanisms involved in mediating the observed effects and whether the early detectable changes are relevant for humans.

Chapter 4 The effect of the IOP elevation levels (ischemic vs non-ischemic) on the rat retina structure, function and blood perfusion

Notes and Acknowledgement

This chapter describes the optical design of a combined OCT+ERGs system that was developed for simultaneous acquisition of OCT morphological images, Doppler OCT blood flow data and ERG recordings. The OCT+ERG system was used in a rat model of glaucoma to investigate the effect of ischemic and non-ischemic acute IOP elevation levels on the rat retinal morphology, blood flow and perfusion and the retinal response to visual stimulation. The content of this chapter is based on the following journal manuscript that was submitted to *Scientific Reports*:

B. Tan, B. Maclellan, E. Mason and K. Bizheva. "The effect of acute intraocular pressure elevation to ischemic and non-ischemic levels on the rat retinal structure, function and blood perfusion, evaluated with a combined OCT + ERG system."

Author contributions

Bingyao Tan and **Kostadinka Bizheva** conceived the study.

Kostadinka Bizheva provided the study materials.

Bingyao Tan designed, built and tested the combined OCT+ERG probe.

Bingyao Tan collected the OCT and ERG data, and **Benjamin Maclellan** helped with the animal handling and monitoring.

Bingyao Tan wrote the algorithm for *en-face* TRBF calculation, the microvascular density calculation and the OCTA image extraction; **Bingyao Tan, Erik Mason and Benjamin Maclellan** wrote the algorithm for the microvascular map generation.

Bingyao Tan analyzed the data and wrote the first draft of the manuscript.

Kostadinka Bizheva contributed to the interpretation of the results.

All authors contributed to the final version of the manuscript.

4.1 Introduction

Raised IOP is a well-known risk factor in open angle glaucoma and therefore it is the most studied pathogenic characteristic of glaucoma. In the past, multiple studies have reported separately the effect of IOP elevation on retinal blood flow or retinal function. Blood flow detection methods included laser Doppler flowmetry[169], [170], ultrasound[25], and MRI[171], adaptive optics OCT[172] and adaptive optics scanning laser ophthalmology[173]. Visually evoked changes in the retinal function were typically assessed with ERG or VEP. Previous studies on animal models of elevated IOP-induced changes in retinal blood flow and retinal function showed large variability of results and conclusions within and between different studies, most likely due to use of different imaging systems or focusing on different animal study related parameters such as blood pressure[174], animal age[27], [37] and strain[175]. To date, only a few studies have reported assessment of both retinal blood flow and function during IOP manipulation[176]. In all of those studies, either separate groups of animals were used, or the same animals were re-anesthetized and the retinal function and blood flow were measured separately during two successive acute IOP elevations. A combined OCT and ERG system would enable simultaneous imaging and assessment of retinal morphology, blood flow and function, which will reduce the variance in the acquired data and minimize the effect of additional anesthesia on the retinal function and blood flow. Such a combined OCT+ERG system has been used recently to assess simultaneously and correlate[119], [177] visually evoked intrinsic optical signals and ERG recordings with retinal morphology in chicken. The same system was also used to assess neurovascular coupling in the rat retina by

measuring simultaneously and correlating visually evoked changes in the retinal blood flow and function[178]. Therefore, the OCT+ERG technology combined with various scanning protocols for Doppler OCT and OCTA could be serve as a very useful research tool to investigate the dynamic correlation between morphological, blood flow and functional changes in the retina for various retinal diseases, including glaucoma.

In animal models of glaucoma, both acute and chronic IOP elevation are well-documented to cause both reduction in the retinal blood flow and decrease in the retinal functional response to visual stimulation. Specifically, in rodents[53], [179], monkeys[46], [180], and rabbits[24], acute IOP elevation is associated with temporary impaired retinal cell function, assessed by ERG, for IOP levels of 50 mmHg and higher, while in other studies, reduced retinal blood flow[25], [57]–[59] was detected at IOP levels as low as 30 mmHg. The difference in the ways retinal blood flow and retinal function are resistant to changes in their responses to acute IOP elevation was partially explained by a mathematical model[176] which proposed that increased oxygen extraction ratio compensates for the relative ischemia caused by the reduced blood flow in order to sustain retinal function. This model was validated through studies on rodents with normal and abnormal blood pressure[181] and with/without diabetes[182] where the IOP was elevated using cannulation. In those studies, all animals exhibited more preserved retinal function compared to retinal blood flow for IOP elevation to moderate levels, while both attenuated retinal function and blood flow were observed for ischemic IOP levels (>60 mmHg).

Recent studies[175], [183], [184] by our research group also examined changes in the rat retinal function in response to IOP elevation in different rat strains and under different types of anesthesia. The IOP in those studies was elevated to a non-ischemic level of 35 mmHg using a vascular

loop[114]. In one of the studies, the IOP was also raised to an ischemic level of 80 mmHg using the same method. Results from all of those studies showed temporary increase in the ERG a-wave and b-wave magnitudes by ~ 5x to 7x (supra normal ERG) during IOP elevation to 35 mmHg, compared to baseline and post-loop measurements, while no significant ERG response was observed for IOP elevation to 80 mmHg. Given the close relationship between retinal function and retinal blood flow, it is worth investigating what is the retinal blood flow response to acute IOP elevation, induced by the vascular loop, as well as what is the correlation between the retinal blood flow and functional changes for different levels of IOP spanning from non-ischemic to ischemic ones. In this study, we used a combined OCT + ERG system, as well as DOCT and OCTA image acquisition protocols to measure simultaneously changes in the rat retina structure, blood flow, blood perfusion and function in response to step-wise IOP elevation from 10 mmHg (normal level for healthy rat retina) to 70 mmHg (ischemic level).

4.2 Methods

4.2.1 OCT+ERG system and data acquisition

The combined OCT+ERG system used for this study was developed recently by our research group for investigating the neurovascular coupling in the rat retina[177], [178], [185] and the effect of acutely elevated IOP on the retinal morphology and function. Briefly, the OCT system operates in the 1060 nm spectral region and provides ~3.5μm axial and ~5 μm lateral resolution in retinal tissue with ~100 dB sensitivity for 1.7 mW optical power of the imaging beam incident on the cornea. Ultra-sensitive OMAG protocol was utilized to generate OCTA images of the retina around the ONH (3.4 mm x 3.4 mm; 512 A-scans × 512 positions × 4 scans/position). DOCT images were acquired with highly overlapped scans from a relatively smaller area centered at the

ONH (2 mm x 2 mm, 3000 A-scans x 200 B-scans). The camera image acquisition rate was set to 92 kHz, resulting in blood flow velocity detection range of [-17.4, 17.4] mm/s. A commercial ERG system (Diagnosys LLC, Lowell, MA, USA) was integrated with the OCT system and the data acquisition for the two systems was synchronized. A custom visual stimulator was designed and integrated with the OCT imaging probe[177], [178]. During the OCT+ERG imaging procedure, light from the visual stimulator was focused at the pupil plane of the rat eye in order to generate a wide angle, almost uniform Maxwellian illumination of the retina. For this study, five scotopic ERG traces, separated by 1-minute dark period, were recorded with white light, single flash stimuli of 1 ms duration and 1.23 log scotopic cd·s/m² illumination level.

Because the vascular loop introduces mechanical deformation of the eye ball that can cause changes in the axial length of the eye and corneal curvature, and therefore affect the magnitudes of the ERG metrics such as the a-wave, b-wave and oscillatory potentials, we used a swept source OCT system (SS-OCT) with sufficiently long scanning range (7 mm in free space) to evaluate those changes. Since the SS-OCT system was originally designed for imaging of the human cornea, its optical design and performance was described in an earlier publication from our group[186]. Briefly, the SS-OCT system utilizes a tunable laser (Axsun Technologies, Inc.) with sweep range centered at 1040 nm, sweep rate of 100 kHz and 50% duty cycle. It provides 7 μm axial and 15 μm lateral resolution and imaging range of 7 mm in free space. To evaluate changes in the shape of the rat eye during IOP elevation to levels ranging from 10 mmHg to 70 mmHg, SS-OCT volumetric scans were acquired from a 7 mm x 7 mm area centered at the corneal apex (700 A-scans × 700 B-scans). Because the optical length of the rat eye is larger than 7 mm, the rat eye images were wrapped around the SS-OCT zero delay line so that for each measurement the corneal

apex overlapped with the RPE layer of the retina, which provided sufficient contrast to allow for precise alignment. The axial eye length was then computed as 2x the distance from the top edge of the SS-OCT image (corresponding to the zero delay line) and the location of the corneal apex. Changes in the corneal curvature were evaluated by measuring the height of the anterior chamber (distance between the pupil plane and the corneal apex) and the anterior chamber angle.

4.2.2 Animal preparation and IOP elevation protocol

Eleven-week-old, male Brown Norway rats (~300g) were used in this study (n=6 for retina structure and function measurement with the OCT+ERG system; n=2 for axial eye length measurement with the SS-OCT system). All experiments described here were approved by the University of Waterloo Animal Research Ethics Committee and adhered to the ARVO statement for use of animals in ophthalmic and vision research. Prior to the experiment, the rats were dark-adapted for at least 12 hours and all experiments except for the imaging with the SS-OCT system were conducted in a scotopic environment (631nm, <0.9 lux). The rats were anesthetized with isoflurane and oxygen mixture maintained at 1.5-2.5% throughout the experimental procedures. Afterwards, the rats were placed in a custom stereotaxic animal holder that allowed for XYZ and angular adjustment of the animal eye with respect to the stationary OCT+ERG imaging probe. Furthermore, the anima holder was designed for 360° rotation in a plane perpendicular to the OCT imaging beam, which allowed for easy switch between the left and right eye under the stationary OCT+ERG imaging probe. The base of the animal holder was lined with a thermal pad (Kent Scientific, Torrington, CT, USA) in order to keep the animal body temperature between 36° and 38 °C. One drop of 0.5% proparacaine hydrochloride (Alcaine, Alcon, Mississauga, ON, Canada) was applied to each eye, followed by one drop of pupil dilator

(0.5% tropicamide, Alcon, Mississauga, Canada). Artificial tears were used frequently to hydrate the animal cornea in order to sustain optimal optical clarity of the cornea for the OCT imaging and decrease the electrode impedance of the ERG corneal electrode. The positive ERG electrode in the form of loop with 4 mm diameter was gently placed on the rat cornea to avoid any IOP fluctuations. The negative ERG electrode was placed under the skin behind the ear and the ground electrode was placed into the scalp between the ears.

An adjustable vascular loop (Sentinal Loops; Sherwood-Davis and Geck, St. Louis, MO, United States) was placed anterior to the equator of the eyeball of the right eye to provide controllable IOP elevations, while the left eye served as a contralateral control. Topical anesthesia (0.5% proparacaine hydrochloride, Alcaine, Alcon, Mississauga, Canada) was applied onto the cornea to reduce the rats' sensation to the vascular loop. Different levels of elevated IOP were achieved by manually adjusting the tightness of the vascular loop, and the IOP was measured with a pre-calibrated corneal rebound tonometer (TonoLab, Finland). The IOP was raised unilaterally in steps from baseline (~10 mmHg) to 30 mmHg, 50 mmHg, 60 mmHg and 70 mmHg and then normalized by loop removal. At each IOP level, the rats were stabilized for ~10 minutes and the IOP was measured 3 times prior to the monocular OCT+ERG recordings, and the treated eye was always imaged before the control eye.

4.3 Data Analysis

TRBF was evaluated using the Doppler angle irrelevant *en-face* method proposed by Srinivasan et al[187], [188], and TRBF of the retina was calculated as an average of the absolute total venous and arterial flow around the ONH. The procedure utilized for quantification of the microvascular density in different retinal layer involved three steps. First, the morphological OCT images were

flattened and the flattening index was used to flatten the corresponding OCTA images. Then, all the flattened OCTA images were assembled into a 3D stack. The following retinal layers: the NFL together with the GCL, the IPL and the OPL were segmented manually from the morphological OCT data. Second, MIP was used to generate microvascular maps for each of these three layers. Third, to quantify the vascular density, the microvascular maps were Frangi filtered[189] and binary filtered using MATLAB's Otsu's threshold function[190]. Capillary density was calculated as the number of bright pixels in each layer. Note that the microvascular densities for the IPL and OPL were calculated excluding any areas with shadowing artifacts from major blood vessels on the retinal surface, where the blood vessels with diameters larger than 36 μm were removed from the microvascular density calculation.

The ERG traces were analyzed in terms of three metrics: amplitude and latency of the a-wave and b-wave and the RMS of the OP. The a-wave amplitude is defined as the voltage difference between baseline and the negative peak, while the b-wave amplitude was defined as the voltage difference between negative a-wave peak and the positive b-wave peak. The OPs were filtered using a bandpass filter (100-300 Hz), that was applied to the averaged ERG traces (average of 5 consecutive recordings), then the OP RMS was calculated as the difference of the RMS within a time window from t = 20 ms to t = 70 ms post flash and RMS of the background (t = -50 ms to t=0). Since mechanical stress from the vascular loop at elevated IOP levels changes both the axial length and the corneal curvature of the rat eye, it will alter the coupling of the visual stimulus light into the eye and correspondingly, the illuminated area at the retina surface. Since the amplitude of the ERG a-wave is directly proportional to the number of stimulated photoreceptors, it is therefore dependent on the illumination spot at the retina. Because we are interested in evaluating

physiological changes in the retina associated with the IOP elevation, and separating those from any changes induced by the change in the axial length of the eye that may affect the ERG metrics, in our study we discussed both the raw, unscaled versions of the b-wave amplitude and OPs RMS, as well as their normalized versions, scaled by the a-wave amplitude.

4.3.1 Statistical Analysis

One-way repeated-measures ANOVA was used to determine differences in normalized TRBF as a function of IOP elevations, and two-way repeated-measures ANOVA was used to determine differences in retinal microvascular densities, ERG components, as a function of IOP elevations and eyes. Greenhouse-Geisser corrections were used for epsilon values less than or equal to 0.75. Bonferroni-corrected multiple comparison tests were used post hoc to determine any differences between the loop conditions.

4.4 Results

4.4.1 Morphological Changes

Figure 4.1A shows a morphological OCT image overlaid with its corresponding Doppler OCT image at normal IOP. Surface blood vessels (BV) are color coded, where red color represents veins and blue color represents arteries. Capillaries appear as white dots in the inner retina (white arrows), and bidirectional blood flow is also observed in large choroidal blood vessels. A wide angle 3D image of a healthy rat retina is shown in Fig. 4.1B, while Fig. 4.1C shows a representative 3D image of the anterior rat eye with a vascular loop. Figures 1D-1F show the retinal microvasculature for the three segmented retinal layers: NFL+GCL, IPL, and OPL, color coded in red, green and blue colors respectively.

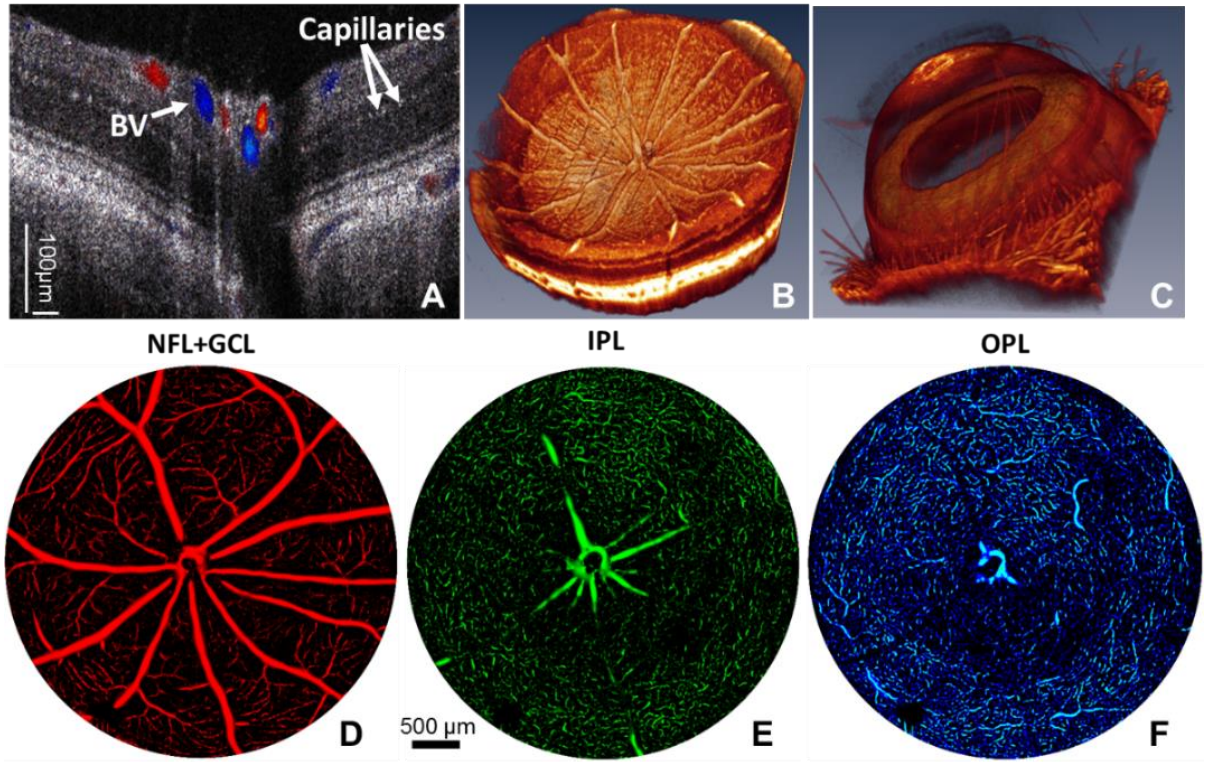

Figure 4.1 Representative morphological OCT, DOCT and OCTA images of the rat eye. (A) Cross-sectional morphological OCT image of the rat retina overlaid with DOCT to show the retinal vasculature with arteries marked in blue and veins in red color. (B-C) Volumetric 3D OCT images of the rat retina and anterior eye chamber respectively. (D-F) OCTA images of the retinal vasculature (IOP = 10 mmHg) of the NFL+GCL, IPL, and OPL layers respectively.

Figure 4.2 shows a series of cross-sectional morphological OCT images acquired through the center of the ONH for different levels of the IOP. The step-wise IOP elevations caused progressive deformation of the ONH. The mechanical deformation of the rat eye ball also caused a focal shift of the OCT imaging beam from the surface of the retina toward the posterior retina which is noticeable for IOPs > 50 mmHg or higher, resulting in lower contrast of the retinal images. Within 30 minutes from removal of the vascular loop, the ONH recovered to its original shape, indicating possibly no permanent damage to the ONH structure. Morphological images acquired from the control eye did not show any significant changes associated with the IOP elevations (data not

shown here).

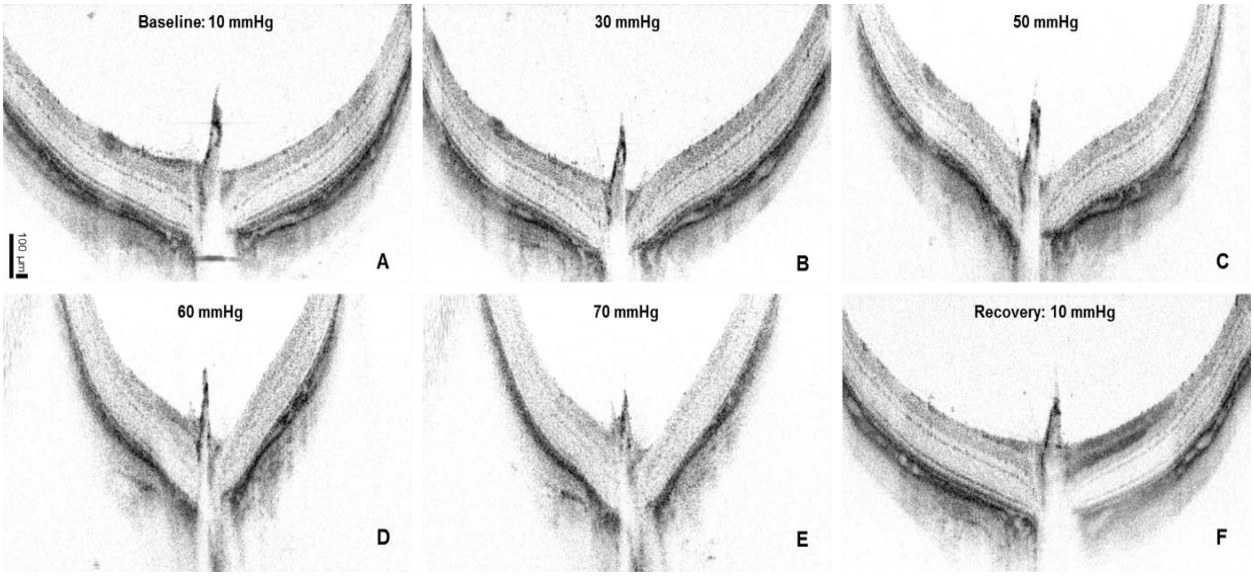

Figure 4.2 Representative cross-sectional OCT images of the ONH showed progressive deformation of the ONH associated with elevated IOP (A-E). (F) ONH morphology recovered 30 minutes after loop removal. Image contrast decreased due to a shift of the focal plane of the eye beyond the RPE layer when IOP was elevated to higher than 50 mmHg.

4.4.2 Axial eye length changes

Analysis of the SS-OCT data showed IOP associated changes in the shape of the rat eyeball. Figure 4.4 demonstrates the relationship between IOP and the axial eye length. A linear fit of the data shows a strong correlation between the IOP and the axial eye length (*r-square* = 0.95). Further analysis of the SS-OCT images showed no significant and measurable changes of the anterior chamber depth, suggesting that there were negligible changes to the curvature of the rat's cornea.

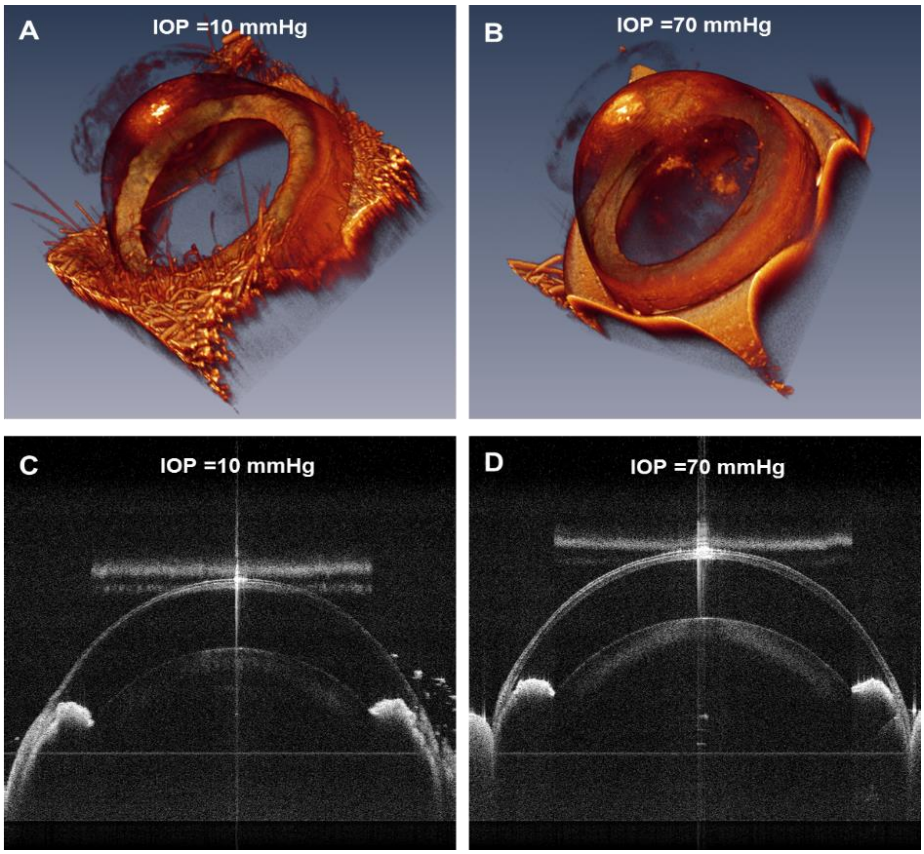

Figure 4.3 Representative anterior chamber 3D volumes and cross-sectional B-scans across the cornea apex when IOP was at baseline (10 mmHg) and ischemic level (70 mmHg).

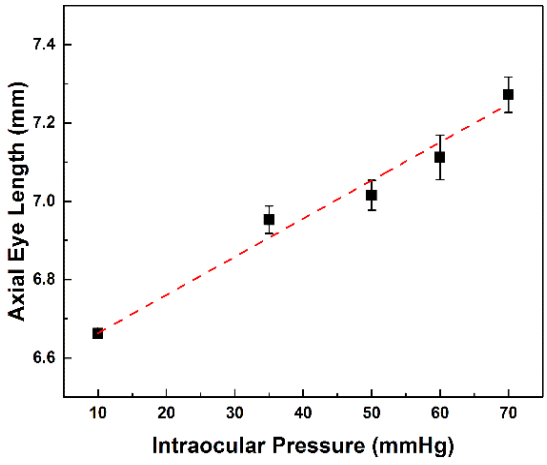

Figure 4.4 Correlation of IOP and the axial eye length.

4.4.3 TRBF changes

Figure 4.4 shows maximum projection Doppler OCT images of the retinal blood flow at the ONH

and its vicinity. Blue and red color correspond to arteries and veins respectively based on the phase polarities. The green arrows in Figure 4.5A-B indicate the apparent loss of blood flow in a small vessel for IOP of 30 mmHg, without apparent significant alteration of the blood flow in the larger retinal blood vessels. When the IOP was elevated to 50 mmHg and higher, significant reduction of the retinal blood flow was observed, and the blood flow in the peripheral area was affected more strongly compared to the ONH as shown in Figure 4.5D-E. Pulsation of the retinal arteries associated with the cardiac cycle can be observed as dark lines across the blue colored arteries in all images in Figure 4.5. For IOP elevation of 70 mmHg, the pulsation in the retinal arteries even caused an apparent retinal blood flow direction change, seen as change between blue and red color in Figure 4.5E (yellow arrow). The same effect was also observed by Zhi et al.[57] in a retinal blood flow study, where anterior chamber cannulation method was used to elevate the IOP in rats.

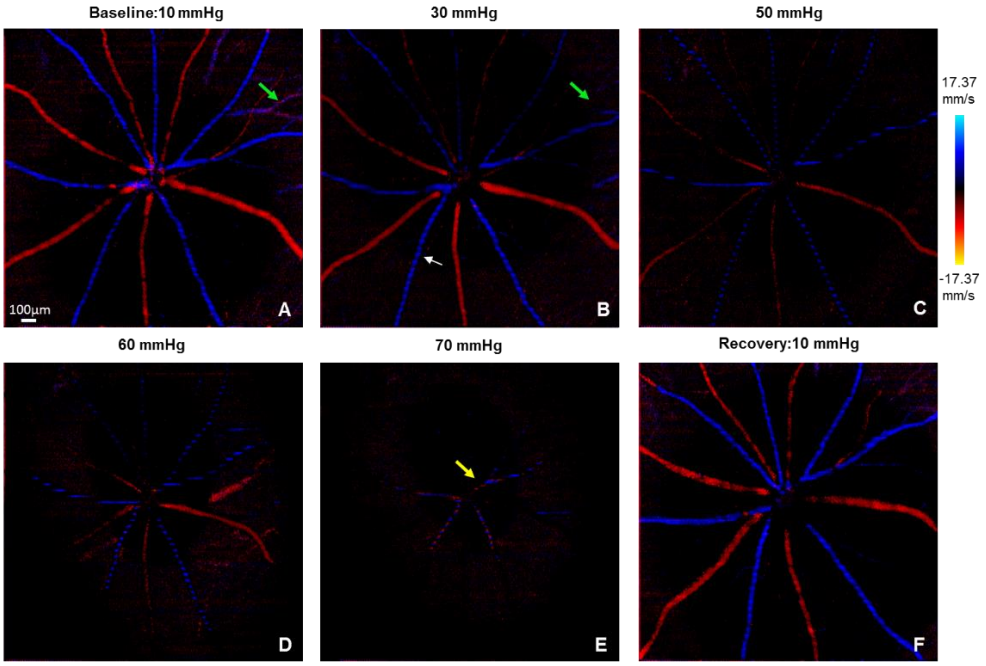

Figure 4.5 Representative *en-face* max projected DOCT images in response to different IOP levels. Blue and red color represent arteries and veins. White arrow: cardiac pulsation effect on the retinal blood flow. Yellow arrow: pulsatile flow direction change at highly ischemia level IOP. Green arrows: difference of small blood vessel with IOP elevation to 30 mmHg. Scale bar= 100µm.

Statistical results for the TRBF measured for different levels of IOP are shown in Fig 4.6. TRBF change in the treated eye was normalized to the control eye, as the existence of large variance of retinal TRBF among animals is well known[191], [192]. Normalized TRBF was significantly lower at IOP of 30 mmHg ($p<0.01$) and decreased monotonically with higher IOP. Specifically, TRBF at 30 mmHg and 50 mmHg IOP had a steep decrease from baseline and was at about 70% and 20% of baseline compared to the control eye ($p <0.01$). When the IOP was raised above 50 mmHg, the decrease gradient was smaller, though the change in the TRBF between those three data points was not significant ($p=1.00$). Note that the blood flow at 70 mmHg is close to the detection threshold of our OCT system due to the significantly altered geometry of the eyeball at

that IOP level. The TRBF measured during the recovery phase (30 min after removal of the vascular loop), had a significant increase relative to the measurement at 70 mmHg ($p<0.01$) and fully recovered to the pre-loop level ($p=1.00$).

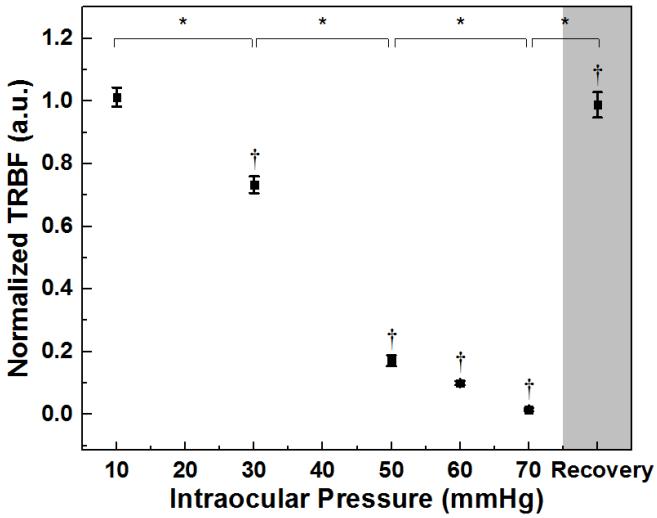

Figure 4.6 Effect of IOP on TRBF (Mean ± SE). Data are presented as normalized to the control eye. †Significant difference compared to baseline ($p<0.01$). *Significant difference compared to the previous step ($p<0.01$).

4.4.4 Blood perfusion changes

Representative retinal blood perfusion maps for the OPL, generated for normal and elevated IOP are shown in Figure 4.7. For better visualization of the IOP induced changes, the microvascular maps were overlaid with their corresponding blood vessel density maps. Shadow artefacts from the surface retinal blood vessels were filtered out by excluding the blood vessels with size lager than 36 μm (blood vessel size was determined by Euclidean distance transform).

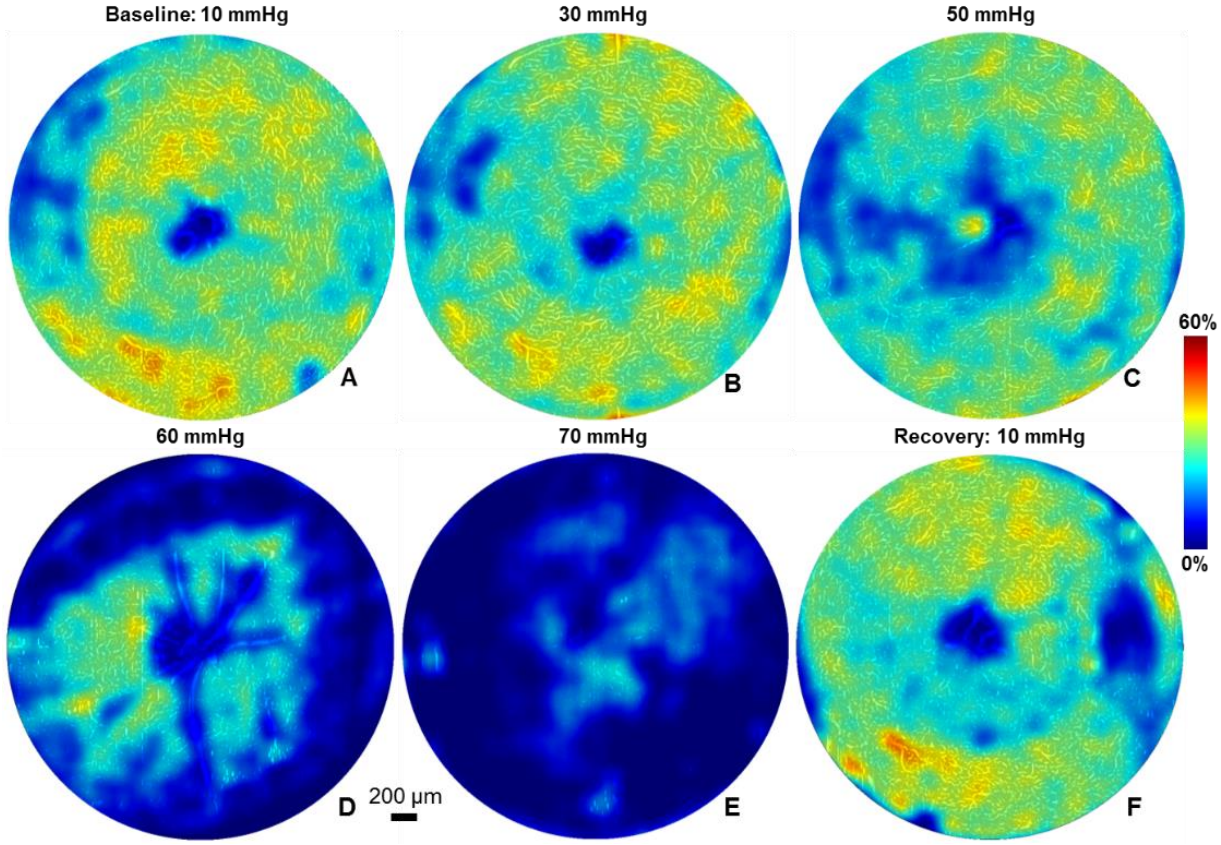

Figure 4.7 Representative microvascular map overlaid with density map in OPL at different IOP levels. Different colors denote the microvascular density from 0% to 60%.

Statistical results summarizing the retinal blood perfusion changes in the three segmented retinal layers (NFL+GCL, IPL and OPL) associated with the IOP elevation are shown in Figure 4.8. Overall, in all three layers, the microvascular densities changed significantly with the elevated IOP ($p<0.05$). Microvascular density in the control eye remained unchanged in all three layers for normal and elevated IOP ($p=1.00$). In the treated eye, in all three layers, the microvascular density was significantly lower than the control eye when the IOP was raised to 60 mmHg or 70 mmHg ($p<0.05$). When the IOP was raised to 50mmHg, the significant interocular differences were only detected in IPL and OPL. Thirty minutes after loop removal, recovery of microvascular density to the baseline in all three retinal layers were observed ($p=1.00$).

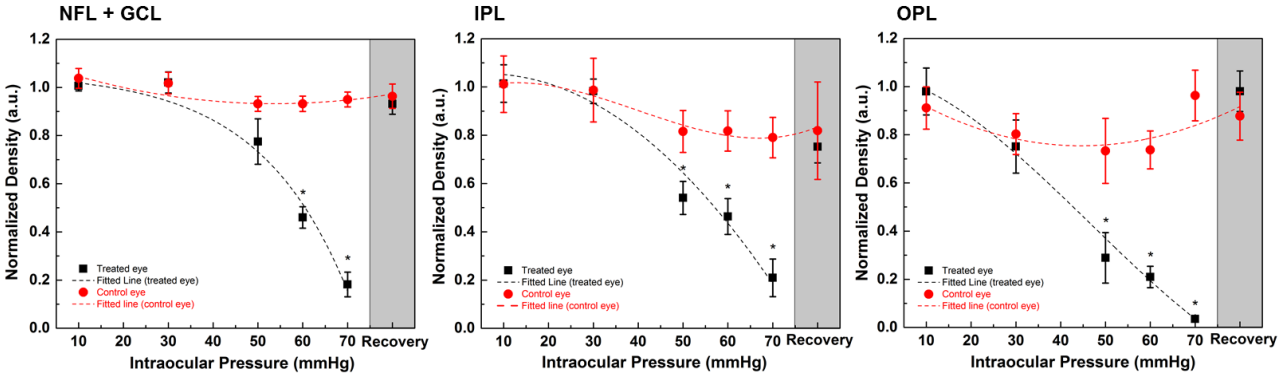

Figure 4.8 Microvascular density in (A) NFL+GCL, (B) IPL, and (C) OPL at different IOP levels. Density data in both eye are represented in Mean ± SE with fitted polynomial function (dashed lines). Recovery data in the treated eye is excluded from fitting. *Significant difference between two eyes.

4.4.5 Retinal function changes

The ERG a-wave, b-wave and OP correspond to visually evoked responses from photoreceptors, ON bipolar and Müller cells, and amacrine cells, respectively[101]. Representative ERG traces and the extracted OPs for different IOP elevation levels, acquired from one animal are presented in Figure 4.9A. Black and grey colors correspond to the treated eye and control eye, respectively. The control eye response exhibited good stability during the loop-on procedure, indicating lack of fellow-eye effect for elevated IOP. Figures 4.9B-D summarize statistical data for the ERG metrics (a-wave, b-wave and OPs RMS) from a group of 6 rats. The a-wave amplitude increased significantly from baseline to 60 mmHg ($p<0.01$), but there was no significant statistical difference between the data acquired at 30 mmHg, 50 mmHg, and 60 mmHg in the treated eye. When the IOP was elevated to 70 mmHg, the a-wave amplitudes measured in the treated eye were on average lower than those in the control eye ($p=1.00$). The ERG b-wave amplitude behaves in a different manner. It increased significantly from baseline and peaked for IOP of 30 mmHg ($p<0.01$), then progressively declined to the same value measured in the control eye at ~55 mmHg. For IOP of 60

mmHg and 70-mmHg, the b-wave magnitude was significantly lower than the control (both $p<0.01$). Similar to the ERG b-wave amplitude, OPs RMS increased at IOP of 30mmHg ($p<0.01$), and returned to baseline when the IOP reached 50 mmHg ($p=1.00$). Afterward, it continued to decrease to a level significantly lower than the control for IOP of 60 mmHg and 70 mmHg (both $p<0.01$). After loop removal, all ERG components (a-wave amplitude, b-wave amplitude and OP RMS recovered to values higher than the control, but the differences were not statistically significant (all $p>0.05$).

The normalized versions of the ERG b-wave amplitude and the OPs RMS are presented in Figure 4.9E and 4.9F respectively. In contrast to the unscaled versions, the normalized b-wave amplitude and the OPs RMS decreased monotonically with the IOP elevation, and for IOP levels of 50 mmHg to 70 mmHg, both the normalized b-wave amplitude and the OPs were significantly lower than the ones measured from the control eye ($p<0.01$ in all comparisons), while no significant intraocular difference was detected at 30 mmHg (b-wave: $p=1.00$; OP: $p=0.12$). After loop removal, the a-wave recovered to a value higher than the one measured in the control eye, while the normalized b-wave and OP recovered to values lower than the control ones; however, these differences were not statistically significant (for all comparisons, $p>0.05$).

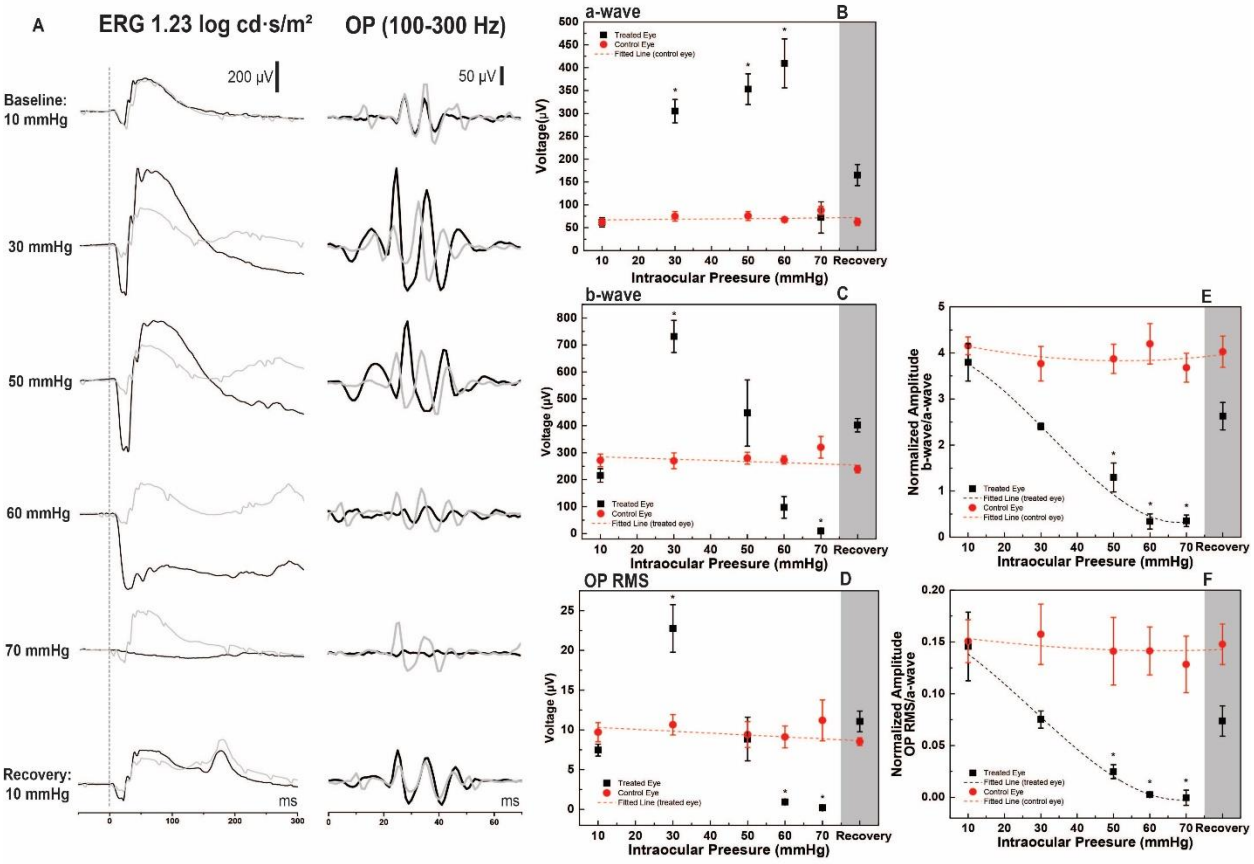

Figure 4.9 (A) Representative ERG and the respective OP at different IOP levels. (B-D) Statistics of ERG a-wave, b-wave, and OP RMS amplitudes at different IOP levels. (E and F) Normalized b-wave and OPs RMS respectively. *Significant difference between two eyes. Data is presented as: Mean ± SE.

4.5 Discussion

Morphological data from our study showed that the ONH depression increased progressively in magnitude with increasing of the IOP level. Similar changes in the ONH depression depth with elevated IOP was observed in a number of studies that utilized different IOP elevation methods, including the vascular loop technique, as well as different IOP levels[44], [183], [193]. In our study, we also observed a recovery of the ONH to its original shape at about 30 min after loop removal even after an IOP insult to an ischemic level of 70 mmHg. This result suggests that a short

term, acute elevation of IOP to ischemic levels causes no permanent damage or possibly minimal damage to the ONH tissue that is below the detection threshold of the OCT system. Other groups have also shown that the ONH shape recovers after acute IOP elevation to 100 mmHg[116], and 30 minutes after elevating IOP to 70 mmHg for 60 minutes[60], both of which used anterior chamber cannulation to raise the IOP. In a recent study, our group showed that IOP elevation to a moderate level of 35 mmHg for 1h/day, 6 days/week for 8 weeks is necessary to observe significant and reproducible changes in the shape and depression depth of the ONH (data not shown, though included in the next chapter of this thesis and the corresponding manuscript).

By cannulating the anterior chamber to elevate IOP[57], retinal blood flow was reported to decrease significantly when the IOP was raised to 30 mmHg, and drop to lower than 50% of baseline for IOP higher than 60 mmHg. Our results obtained with the vascular loop method showed somewhat similar behavior of the TRBF: significant decrease in the TRBF was observed when the IOP was elevated to 30 mmHg. However, for IOP of 50 mmHg, the TRBF was at ~20% of its baseline value, or compared to the TRBF of the control eye. One possibility is that the ONH deformation was larger for IOP higher than 50 mmHg when the IOP elevation was induced with the vascular loop compared to the anterior chamber cannulation method[59], due to the additional total eye length change resulting from the mechanical compression of the eye ball during loop wear. Therefore, the larger stress applied on the ONH could result in ONH ischemia. One possible explanation is that vascular loop-induced IOP elevation by compressing the episcleral vein may have a similar effect on the retinal and choroidal flow as sclera buckling or encirclement. Sclera bucking and encirclement have been well documented to affect the retinal blood flow and choroidal flow[84], [194]–[197]. Specifically, Ogasawara[197] and Regillo[196] reported up to 53%

decrease of arterial flow velocity in patients after scleral buckling and circling procedures, and Sugawara[195] reported a sustained reduced choroidal flow from 2-4 weeks after sclera buckling. Therefore, compression of the ocular tissue with the vascular loop could affect the blood circulation in the eye and alter significantly the retinal blood flow and choroidal blood flow.

Decrease in the capillary density of the IPL and OPL has been observed previously for IOP elevation to levels higher than 60 mmHg with the cannulation method[198]. In that study, microvascular density in the OPL measured at IOP of 60 mmHg was at 60% of the baseline value. In contrast, results from our study showed that with the vascular loop method, the OPL microvascular density for the same IOP level was at ~20% of baseline value. Since both studies were conducted on the same strain of rats, there are 2 major factors that can contribute to the discrepancy in the results from the 2 studies. One factor is the method of IOP elevation. As mentioned above, similar to the sclera bucking and encirclement methods, the vascular loop may affect blood flow and perfusion in the retina more strongly than fluid pressure in the posterior chamber of the eye induced by cannulation. Furthermore, the loop-induced mechanical deformation of the eye and resulting increase in the axial eye length cause both shift of the focal plane of the eye beyond the RPE layer and possibly larger depression depth of the ONH. It is also noted that the Frangi filter may have an effect of quantifying capillary density. The combined effect of these factors could cause loss of visibility of capillaries in the capillary maps. A second factor to consider is the difference in the OCT systems' design and performance. Although both systems are SD-OCT and provide sensitivity of ~ 100dB, the one used by Wang's group had an image acquisition rate of 240 kHz, while the image acquisition rate for the system used in our study was 92 kHz. The OCT systems' design and image acquisition rate will affect the sensitivity

of the OMAG method utilized both research groups to detect microvessels in the OPL layer. Measurements of the retinal function for a moderate IOP elevation level (IOP=30 mmHg) and a highly ischemic IOP level (70 mmHg) agreed with results from a previous study with a vascular loop by Choh et al[183] and also extended the observation of retinal function transit to multiple level IOP elevations. The ratio between the b-wave and the a-wave considers photoreceptor's activity as an input and post-synaptic neuronal activity as an output[101].The ERG b/a ratio has been proven to serve as a good indicator of diseases caused by retinal ischemia[199], such as central retinal vein occlusion[200], [201] and retinal artery occlusion[202]. Moreover, Kong and his colleagues[54] used cannulation to raise the IOP acutely in rats, and reported reduction of the a-wave and b-wave amplitudes and the OPs RMS with IOP elevation, where the gradient of the b-wave amplitude and OPs RMS reduction was faster than that of the a-wave amplitude. Results from our study are in agreement with Kong et al.: the b-wave/a-wave ratio in our study decreased monotonically with IOP and correlated well with the IOP-associated reduction in the TRBF. Furthermore, an IOP of 70 mmHg is highly ischemic and results in blockage of the metabolic supply to the inner retinal cells. This process can explain the absence of b-wave for IOP of 70 mmHg. OPs are also sensitive to retinal ischemia[101]. Sperous[203] showed attenuated OPs with mild retinal ischemia and OPs were also regarded as an indicator of background retinopathy[204], [205], when only small blood vessels are damaged. The RMS of the normalized OPs in our study decreased monotonically with increase of the IOP and that response correlated well with the observed decrease in the normalized b-wave amplitude and the TRBF. Therefore, normalized b-wave amplitude and OP RMS, could serve as sensitive markers to study IOP-associated retinal ischemia. Our results also showed that half an hour post-loop recovery phase is not sufficient for

complete recovery of the retinal function to baseline. For example, at the end of the 30 min recovery phase, the a-wave amplitude reached only ~ 50% of its baseline value. Similarly, the normalized b-wave amplitudes and the OPs RMS in the treated eye were still ~35% and ~50% lower compared to baseline and to the control eye. He et al.[55] found that the recovery time for retinal function is dependent on the peak IOP level. He et al. elevated the IOP to 70 mmHg for 30 minutes by anterior chamber cannulation and observed that retinal function, evaluated by negative scotopic threshold responses (nSTR), and recovered only to 50% of its baseline value for a recovery time of ~ 30 minutes.

4.6 Conclusion

In summary, we used a combined OCT + ERG system to study the retinal structure, function, blood flow and blood perfusion in response to acute IOP elevation to ischemic and non-ischemic levels. Significant and progressive TRBF reduction was observed for IOP levels as low as 30 mmHg and as high as 70 mmHg, while microvascular density in the inner retina was more resistant to IOP-induced changes for moderate levels of IOP elevation. Analysis of the normalized b-wave amplitude and OPs RMS showed good correlation to the retinal ischemia, while supernormal a-wave amplitude was detected for IOP levels lower than 70 mmHg.

Chapter 5 Morphological and functional changes in the rat retina and optic nerve head associated with chronic intermittent IOP elevation

Notes and Acknowledgement

This chapter summarizes results from a chronic study in a rat model of glaucoma that was conducted with the combined OCT+ ERG system. In this study, the IOP of one eye was elevated for 1h/day on 6 days of the week over a period of 8 weeks. Morphological images (UHR-OCT) and functional retinal data (ERG) were acquired simultaneously from the treated eye and then the control eye of all animals at baseline (week 1 of the study) and subsequently at weeks 5 and 9 of the study. The content of this chapter is based on a journal manuscript:

B. Tan, A. Gurdita, V. Choh, K. M. Joos, R. Prasad and Bizheva, Kostadinka. "Morphological and functional changes in the rat retina associated with 2 months of intermittent moderate intraocular pressure elevation, measured with a combined OCT and ERG system," submitted to the *Journal of Biomedical Optics.*

Author contributions

Kostadinka Bizheva, Vivian Choh and **Karen M Joos** conceived the study and provided the materials for the study.

Bingyao Tan collected the OCT, ERG and STR data, and **Akshay Gurdita** helped with the animal handling and monitoring.

Bingyao Tan wrote the OCT image processing algorithms and analyzed all OCT, ERG and STR data.

Ratna Prasad conducted the histology.

Kostadinka Bizheva, **Vivian Choh**, **Karen Joos** and **Akshay Gurdita** contributed to the interpretation of all results.

Bingyao Tan wrote the first draft of the manuscript.

All authors contributed to the final version of the manuscript.

5.1 Introduction

Glaucoma is a chronic, degenerative optic neuropathy associated with elevated IOP, resulting in morphological changes of the ONH such as size and shape alterations of the ONH cup[13], [28], [206], progressive loss of RGC axons[28], [207], RGC death[208] and visual field loss[207]. It is the second leading cause of blindness and in 2010 was estimated to have affected over 60.5 million people worldwide, with this number projected to reach ~80 million by 2020[1]. High IOP has been well documented as one of the main risk factors associated with open-angle glaucoma and previous studies have shown that diurnal fluctuations in the IOP may also be a risk factor for glaucoma[74], [209], [210]. Previous studies have revealed a link between the cumulative exposure to moderately elevated IOP over an extended period of time leading to the progressive dysfunction of RGCs and morphological changes of the ONH. In those studies, various methods such as laser photocoagulation[39] of the trabecular meshwork, injection of saline into the anterior eye chamber (cannulation)[36], injection of ICG dye into the anterior chamber combined with laser treatment[211], injection of polystyrene microbeads to block the trabecular meshwork canals and to impede the aqueous humour flow in the anterior chamber [64], [65], and surgical circumlimbal suture[34], [72], [73], [212] were used to elevate the IOP. All of these methods allow for static IOP elevation; however, more recent studies suggest that progressive damage to the ONH and glaucomatous vision loss are also associated with intermittent IOP spikes over a prolonged period of time[18-23]. A headstand yoga posture (Sirsasana) was reported to elevate IOP immediately[110], and routine practitioners could eventually develop glaucoma[77], [213]. In other studies, recurrent uveitis and its treatment can cause intermittent IOP spiking that can lead to glaucoma uveitis[214].

In order to examine the effect of intermittent IOP elevation on the retinal structure and function, Joos et al.[30] used an adjustable vascular loop to elevate the IOP to 35 mmHg for an hour per day on 6 days of the week over a period of 6 weeks, and reported up to 25% thinning of the RNFL, 7%–10% loss of RGC somas, and axonal degeneration in the optic nerve in the treated eye. Gramlich used suction-cup oculopression[215] to elevate the IOP to 30-35 mmHg for one hour a day, and reported significant loss of RGC density in the treated eye after 30 repeated procedures over a period of 6 weeks. Both of these studies focused on quantifying structural changes to the ONH caused by the chronically elevated IOP by utilizing histopathology. Since IOP can affect the retinal function as well, a number of studies explored the effect of acutely elevated IOP on the retinal function. Specifically, Abbott[216] utilized 4h and 8h long acute and moderate ($\leq$ 50 mmHg) IOP elevation in rodents, and showed no evidence of permanent structural damage or functional changes in the retina after the stress. More acute IOP elevation studies[29], [54], [55], [217] confirmed that the retinal function recovers within several hours after normalization of the IOP, and the recovery rate is linearly related to acute IOP exposure[55] and can be affected by age[217]. More recently, our research group used a combined OCT+ERG probe to examine and correlate structural and functional changes in the rat retina in response to acute, moderate level IOP elevation in different rat strains[175], [183].

One question that has not been answered yet is whether intermittent IOP spiking to moderate levels for a few hours a day over a prolonged period would cause temporary or permanent changes in the retinal structure and function during subsequent stress events. Therefore, the purpose of this study was to measure and correlate morphological and functional changes in the rat retina and ONH associated with intermittent, daily IOP elevations to a moderate level during a 2-month period.

5.2 Methods

5.2.1 Animals, anesthesia and IOP elevation

All experiments described here were approved by the University of Waterloo Animal Research Ethics Committee and adhered to the ARVO Statement for the use of animals in ophthalmic and vision research. Six 11-week-old male Sprague-Dawley rats (Harlan Laboratories Inc., Indianapolis, IN, USA), weighing ~350 g were used in our study. The animals were fed ad libitum and maintained in climate-controlled rooms with a 12-hour light/12-hour dark cycle. An adjustable vascular loop (Sentinal Loops; Sherwood-Davis and Geck, St. Louis, MO, USA), placed anterior to the equator of one eye, was used to elevate the IOP, following a procedure developed by Joos et al.[30]. For the daily, short-term IOP elevation, the rats were placed in a custom, Broome-type rodent restraint. One drop of 0.5% proparacaine hydrochloride (Alcaine, Alcon, Mississauga, ON, Canada) was applied to the cornea prior to placement of the vascular loop and elevation of the IOP to 35 mmHg, and afterward every 10 min for the duration of the loop wear. The IOP was measured with a corneal rebound tonometer (Icare® Tonolab, Tuike, Finland) before placement of the vascular loop, immediately after loop placement, every 30 minutes during the loop wear, and at 1 min and 30 min after removal of the loop. Viscous lubricating eye drops (Liquigel, Allergan, Inc., Unionville, ON, Canada) were applied frequently to hydrate the cornea.

Morphological UHR-OCT images and single flash ERG were acquired on weeks 1, 5 and 9 of the study. On the experimental days, the rats were dark adapted for at least 12 hours before they were transferred in light impermeable cages to the research lab for the OCT imaging and ERG recordings. Only a dim, red headlight (631nm, <10.9 lux) was used by the researchers to manipulate the animals and the equipment during the experimental procedures and that light was

switched off during the OCT and ERG data acquisition. The animals were placed on a heated custom animal holder with translational and rotational alignment capabilities to allow for alignment of the rat eye under the stationary OCT+ERG imaging probe. During the experimental procedures, the isoflurane level was kept at 2 - 2.5% and the animal vital signs, such as temperature, breathing rate, and heart rate were monitored every 10 minutes. Subcutaneous injections of 5 ml saline were administered immediately after anesthesia and every 1.5 hours throughout the experimental procedures to hydrate the animals. One drop 0.5% proparacaine hydrochloride (Alcaine, topical anesthetic, Alcon, Mississauga, ON, Canada) was applied to both eyes, followed by one drop of 0.5% tropicamide (Alcon, Mississauga, ON, Canada) for pupillary dilation. The IOP of the right eye was raised to 35 mmHg for 1 hour using the vascular loop and OCT and ERG recordings were acquired at 3 time points: immediately before the IOP elevation, after 40 minutes of loop wear and 30 minutes after loop removal on two experimental days. The UHR-OCT imaging and ERG recordings took ~ 20 minutes.

5.2.2 ERG and STRs

ERG (Diagnosys LLC, Lowell, MA, USA) recordings were acquired sequentially from each eye. In addition to the positive loop electrode placed on the cornea, a negative electrode was placed in the skin behind the ear and a ground electrode was inserted into the scalp between the ears. The calibrated custom visual stimulator generated white light flashes of 7 ms duration and 1.14 log scotopic cd·s/m^2 intensity[183]. Five ERG traces separated by 30 s intervals were acquired from each eye. The duration of each ERG recording was 1 s with a 500 ms pre-stimulus period. The ERG recordings were acquired following the order (pre-loop treated, pre-loop untreated, loop-on untreated, loop-on treated, post-loop untreated, post-loop treated). The amplitudes of the ERG a-

wave and b-wave were measured as the maximum change in voltage from baseline to the first negative peak, and as the change in voltage from the a-wave peak to the peak positive change following the a-wave respectively. Implicit times for the ERG a- and b-waves, were measured from the onset of the light stimulus to the respective peak amplitude. Oscillatory potentials (OPs) were extracted from the ERG recordings using a Fourier bandpass filter (75-300 Hz) and the OPs root mean square (RMS), a metric for the OP amplitude, was calculated for the time period between t = 20 ms and t = 70 ms post flash onset. For intraocular comparison, all ERG components (a-wave, b-wave and OP RMS) were analyzed relative to the untreated eye (treated - untreated).

5.2.3 UHR-OCT

Morphological images of the ONH were acquired *in vivo* with a research-grade UHR-OCT system, that was developed by our research group for various animal retinal studies[175], [177], [178], [183]. Briefly, the UHR-OCT system operates in the 1060 nm spectral region and provides ~3 µm axial and ~5 µm lateral resolution in the rat retina at an image acquisition rate of 92 kHz. The OCT imaging probe was designed to deliver a collimated imaging beam of 1.5 mm diameter and optical power of 1.7 mW to the rat cornea, resulting in ~ 5um lateral OCT resolution in the rat retina. The OCT imaging probe was integrated with a custom visual stimulator connected to the commercial ERG system (Diagnosys LLC, Lowell, MA)[178]. The visual stimulator was designed to focus the light from a white LED onto the pupil plane of the rat eye, thus generating a while angle, almost uniform Maxwellian illumination of the rat retina. Detailed description of the optical design of the integrated OCT imaging probe and visual stimulator is included in a recent publication from our research group[178]. While under isoflurane anesthesia, a custom eyelid retractor was used to keep the imaged eye open. Artificial tears were administered every 5 minutes to keep the corneas

hydrated. Volumetric OCT images (1000 frames x 1000 lines/frame x 512 pixels/line) of the ONH were acquired over an area of ~2 mm^2 first from the untreated and then from the treated eye. Cross-sectional OCT images of the retina were generated from the raw morphological data using a custom Matlab-based (Mathworks, Natlick, MA, USA) code. Volumetric UHR-OCT images of the rat retina were generated from the stacks of 1000 cross-sectional images by using commercially available software (Amira, FEI Visualization Sciences Group; and ImageJ software (http://imagej.nih.gov/ij/; provided in the public domain by the National Institutes of Health, Bethesda, MD, USA). A custom Matlab-based sub-pixel registration algorithm was used to compensate misalignment between B-scans caused by eye motion. The method we used for quantifying the depression of the ONH during loop wear[183] was adapted from an approach first proposed by Burgoyne[9], [123]. Briefly, an *enface* image of the ONH was generated from the 3D imaging stack, and the ONH area was pre-segmented using a region growing method[218], then the cross-sectional image from the center of the ONH was selected by fitting an ellipse to the boundary of the pre-segmented ONH area. Next, the ONH depression was calculated as the distance between the terminations of the Bruch's membrane at the ONH and the line that connects the end points of the Bruch's membrane at the left and right sides of the B-scan. For intraocular comparison, the relative ONH depression (treated-untreated) was calculated over weeks and loop procedures.

5.2.4 Histology

After the last IOP elevation, the rats were anaesthetized with isoflurane until they were unresponsive to toe pinches. Rats underwent cardiac perfusion with saline followed by 4% (w/v) paraformaldehyde in phosphate-buffered saline (PBS) and the optic nerves

were harvested. Six-millimeter long segments of the myelinated optic nerve about 2 mm behind the globe were post-fixed in 1% glutaraldehyde and 4% paraformaldehyde in phosphate-buffered saline for 24 hours. Specimens were postfixed in 2% osmium tetroxide (Sigma-Aldrich, St. Louis, USA) for 1 hour and then embedded in Spurr's low-viscosity embedding media (Electron Microscopy Sciences, Hatfield, PA). Semi-thin 700 nm sections were obtained and stained with 1% p-phenylenediamine (Sigma-Aldrich, St. Louis). A montage of the entire cross-sectional nerve was produced using a computer-driven motorized stage with a 100x oil-immersion objective (Provis AX70, Olympus, Melville, NY, USA). ImageJ software (http://imagej.nih.gov/ij/; provided in the public domain by the National Institutes of Health, Bethesda, MD, USA) was used to measure the nerve cross-sectional area. A fixed grid overlay was used to sample 20% of the total nerve cross-sectional area. All axons within the grid squares were manually counted by a masked person (RP) using ImageJ software to estimate axon density in the nerve (axons/mm^2) and were categorized as "normal" or "degenerating" axons based upon their appearance. Normal axons were defined as possessing a defined myelin sheath surrounding clearly visible pale cytoplasm of the axon, and degenerating axons were defined as containing unraveling myelin sheaths or cytoplasm that were darkened or containing cellular debris. Total number of axons was estimated as the product of the mean axonal density and the nerve cross-sectional area following published protocols[219], [220].

5.2.5 Axial eye length measurement

Because the loop wear causes deformation of the globe that can alter the amount of light

from the visual stimulus that reaches the retina and therefore can affect the metrics of the ERG recordings, we conducted additional measurements and developed a simple mathematical model to evaluate quantitatively this effect. A swept-source OCT system with a 7-mm long scanning range, originally developed by our research group for imaging the human anterior segment[186], was used in this study to measure precisely the rat axial eye length at normal and elevated IOP. Since the optical path length in the rat eye is longer than 7 mm, the OCT images of the rat eye were wrapped around the OCT zero delay line and aligned in such a way that the corneal apex overlapped with the retinal pigmented epithelium. Therefore, the axial eye length was computed as 2x the distance from the top edge of the OCT B-scan to the location of the corneal apex.

5.2.6 Statistical Analysis

Repeated-measures analysis of variance (ANOVA) was used to detect significant differences in all data collected from our study. Greenhouse-Geisser adjustment was applied for epsilon values < 0.75. Bonferroni-corrected multiple comparison post hoc tests were used for determining differences between measurement weeks and loop procedures. Differences were considered significant for p value $\leqslant$ 0.05. All data are presented in the manuscript as mean ± standard deviation and in the figures as mean ± standard error.

5.3 Results

5.3.1 IOP elevations

The average pre-loop IOP was 12.5 ± 0.9 mmHg compared to 12.6 ± 1.0 mmHg of the

untreated eye (p=1.000). The IOP on the treated eye measured immediately after placement of the loop was 40.3 ± 1.1 mmHg and dropped to 34.7 ± 1.4 mmHg (p<0.001), and 32.3 ± 0.8 mmHg (p<0.001) after thirty minutes and one hour of loop wear respectively (Fig. 5.1A). The IOP of the untreated eye stayed fairly constant during loop wear (0 min: 13.0 ± 4.3 mmHg; 30 min: 12.4 ± 3.6 mmHg; 60 min: 11.8 ± 3.4 mmHg) (Fig. 5.1B). Immediately after loop removal, the IOP of the treated eye dropped to 7.8 ± 0.3 mmHg, a value significantly lower than the IOP of the untreated eye at the same time point (11.4 ± 0.5 mmHg, p<0.001), and recovered to 11.2 ± 0.7 mmHg 30 minutes after loop removal. This was not significantly different from the IOP of the untreated eye (11.9 ± 0.6 mmHg, p=1.000) (Fig. 5.1A).

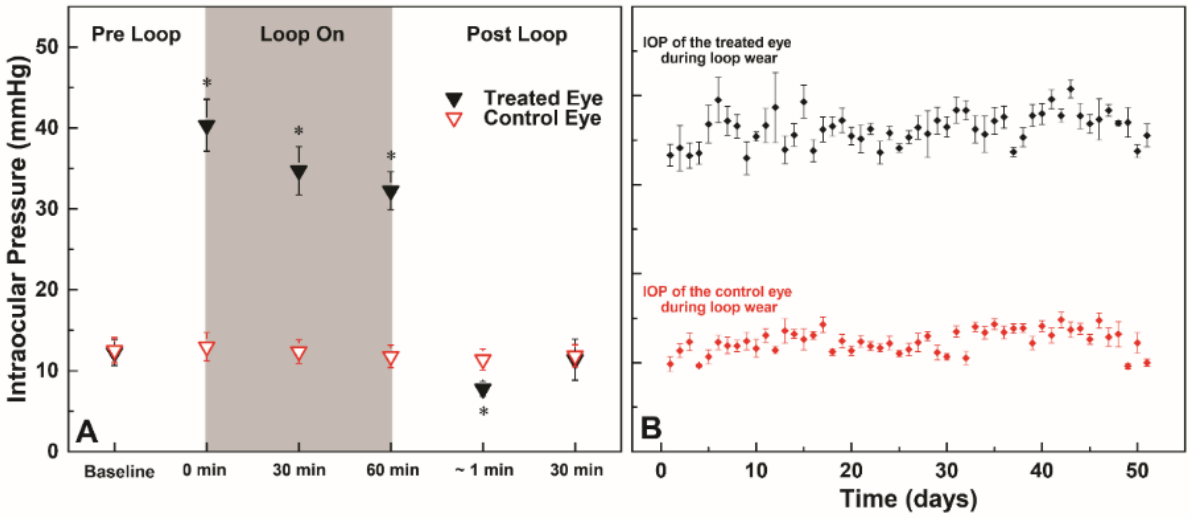

Figure 5.1 IOP data acquired during the ERG and UHR-OCT experimental procedure on weeks 1, 5 and 9 of the study as a function of loop-wear (A) and during the daily IOP elevation for the duration of the study. Each data point is an average of three measurements acquired from each rat. (B). *Significant differences between the treated and control eyes.

5.3.2 Morphological changes

The UHR-OCT images (Fig. 5.2) show that temporary IOP elevation is associated with

backward bowing of the ONH and after loop removal, the shape of ONH recovers to a form very similar to that of the pre-loop measurement.

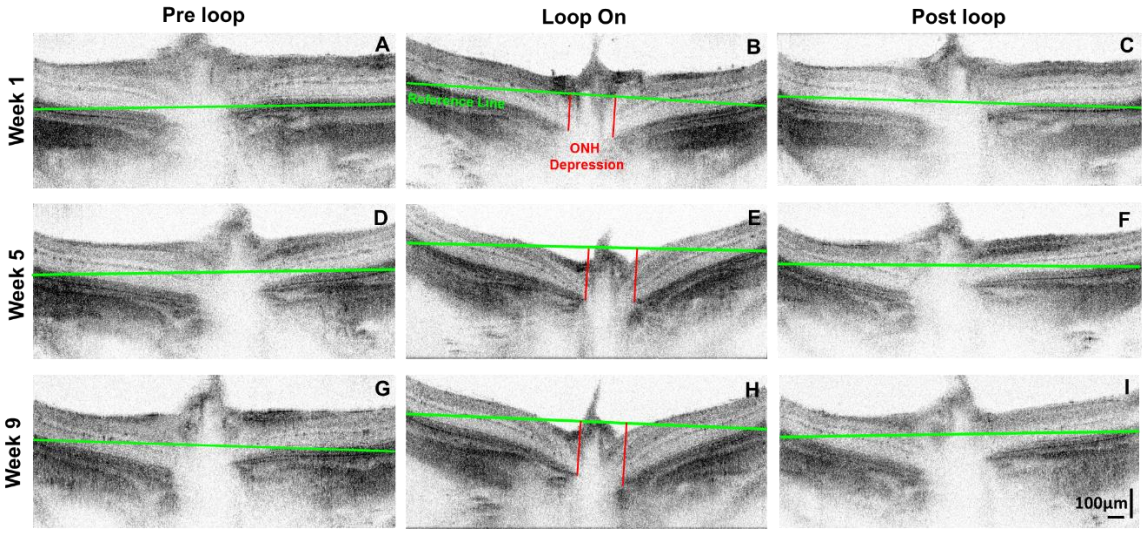

Figure 5.2 Representative cross-sectional morphological UHR-OCT images of the ONH, acquired from the treated eye of a rat at baseline (week 1) and weeks 5 and 9 of the study. Yellow line: reference for the ONH depression was calculated as the distance between the termination of the Bruch's membrane at the ONH and the ends of Bruch's membrane at the left and right edges of the selected cross-sectional image. Red line: depression of the ONH defined as the average distance from the terminations of the Bruch's membrane to the reference line.

The depression depth of the ONH associated with loop-wear increased over time from week 1 to week 9 of the study. Quantitative analysis of the ONH depression (Fig. 5.3) showed that at week 1 of the study, loop wear caused a relative ONH depression of 57.7 ± 31.9 µm compared to the pre-loop (2.1 ± 26.8 µm, p=0.036) and post-loop (20.0 ± 14.1 µm, p=0.555) values, and no significant difference between pre-loop and post-loop conditions was detected (p=1.000). Loop wear-associated relative ONH depression increased over time with chronic elevation of the IOP. Specifically, loop wear-associated, relative ONH depression measured at week 5 and week 9 of the study increased by 119% and 172% respectively, compared to week 1 (week 1 vs week 5, p=0.057; week 1 vs week 9, p=0.011, week 5 vs week 9, p=1.000).

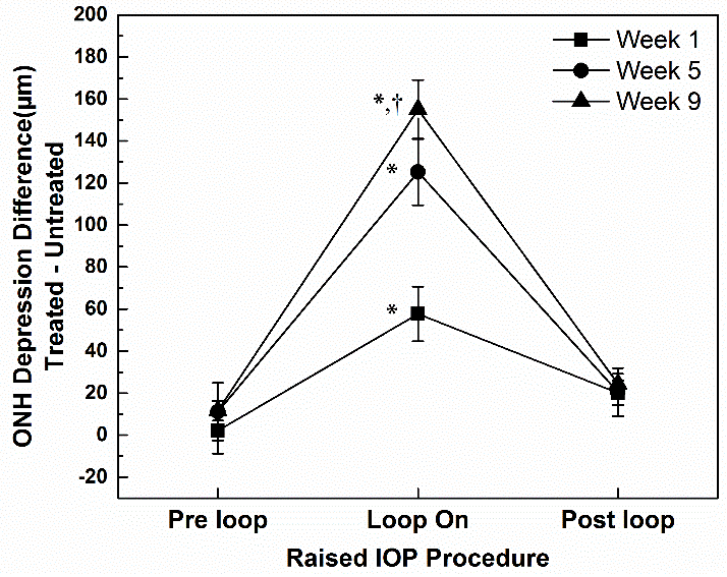

Figure 5.3 ONH depression as a function of IOP. *Significant difference relative to respective pre-loop and week measurement ($p<0.05$). †Significant difference compared to the week 1 loop-wear measurements on the treated eyes ($p<0.05$).

5.3.3 Axial eye length

Analysis of the SS-OCT images showed 4.3 ± 0.9% increase in the axial length of the rat eye during IOP elevation to 35 mmHg. No significant changes were observed in the anterior chamber depth or the iris corneal angle.

5.3.4 Retinal function changes

Figure 5.4A shows typical ERG recordings acquired pre-, during and post loop-wear with stimulus intensity of 1.14 log scotopic cd·s/m^2. Temporal increases in the ERG a-wave, b-wave and OP amplitudes were observed during elevated IOP in the treated eyes relative to the pre- and post-loop conditions. The relative loop-associated enhancements decreased progressively from week 1 to week 9 of the study although not significantly (interaction between weeks and loop procedures; a-wave: $p=0.369$, b-wave: $p=0.511$, OP: $p=0.885$; shown in Fig. 5.4B). The relative a-wave latencies did not change significantly as a function of the loop wear ($p=0.601$) or across weeks ($p=0.329$;

inset of Fig. 5.4B). Although the relative b-wave latencies did not change significantly across weeks (p=0.186; inset of Fig. 5.4C), relative b-wave latencies increased significantly during elevated IOP in the treated eyes compared to the pre- and post-loop values (loop vs pre, p<0.001, loop vs post, p=0.001).

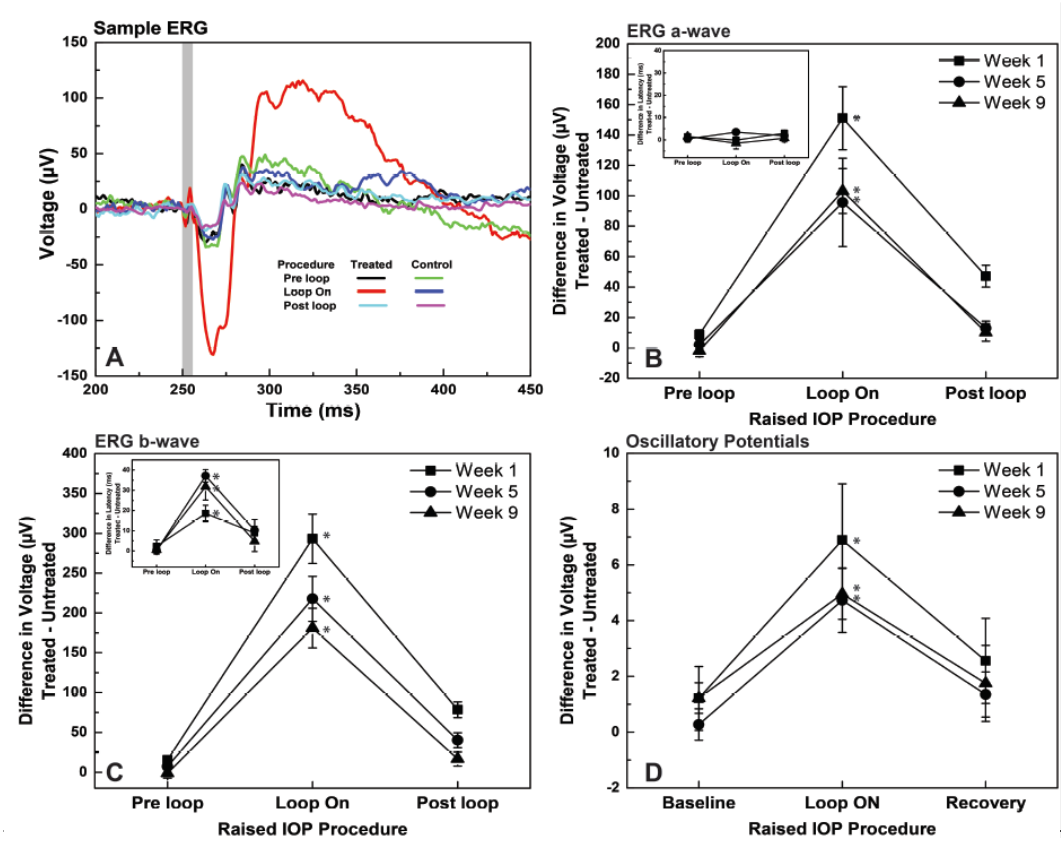

Figure 5.4 Representative ERG traces (1.14 log cd·s/m2) acquired from the treated and untreated eyes of a rat pre-, during, and post-loop wear at baseline (A). The vertical grey line marks the timing and duration of the visual stimulus. ERG a-wave amplitude (B) and latency (Inset in B) and ERG b-wave amplitude (C) and latency (Inset in C), and OP RMS (D) measured pre-, during, and post-loop wear at weeks 1, 5 and 9 of the study. *Significant difference relative to pre loop measurements averaged over weeks.

5.3.5 Optic Nerve Histology

Four animals from our study were adequately perfused postmortem in order to examine quantitatively the loss of axons in the optic nerve after 8 weeks of intermittent IOP elevation. The

total number of axons (Fig. 6B) was significantly lower in the treated eyes (80,397 ± 2620) than the untreated eyes (84,440 ± 2553, p=0.039), which constitutes ~5% loss of total number of axons. The cross-sectional area of the optic nerve was also assessed (Fig. 5.6C); however, no significant change was detected between the treated (0.221 ± 0.010 mm^2) and untreated eyes (0.224 ± 0.019 mm^2, p=0.817). The number of degenerated axons in the treated eyes was 2.9x higher than in untreated eyes (Fig. 5.6D) and the difference was significant (9.4 ± 1.0% vs 3.3±0.4%, p=0.001). Furthermore, in the cross-sectional area, the total number of non-degenerated axons (Fig. 5.6E) in the treated eyes (72,847 ± 1865) was significantly smaller than in the untreated eyes (81,648 ± 2179, p=0.0016).

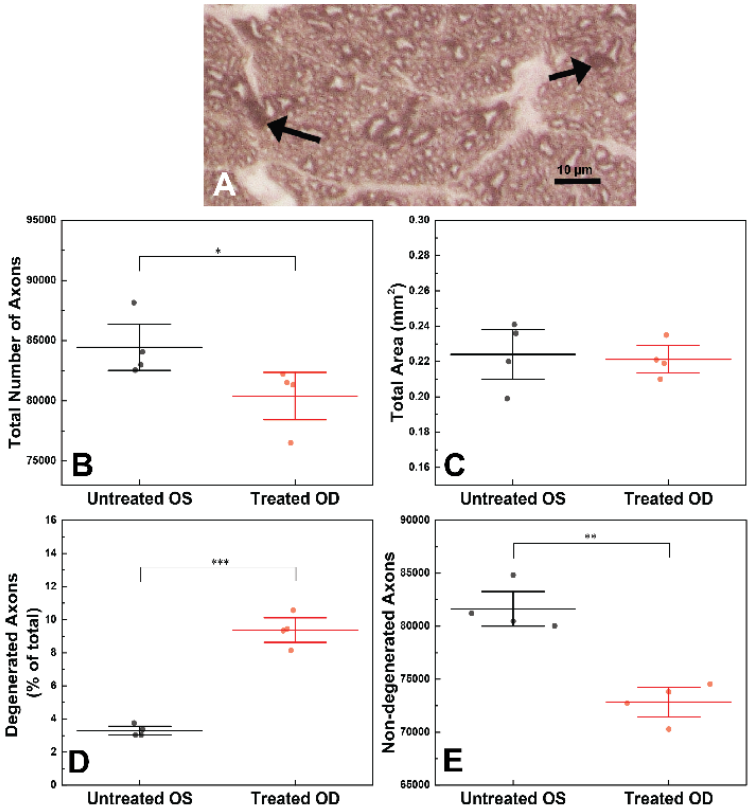

Figure 5.5 Histological images of the optic nerve axonal cross-section, obtained from the untreated and treated eye of one rat (A-B). Statistical results for the total number of axons (B), the total axonal area (C), the percentage of degenerated axons (D) and the total number of non-degenerated axons (E). *p<0.05, **p<0.05, ***p<0.001.

5.4 Discussion

For all measurement points of this chronic study, elevation of the IOP to a moderate level of ~35 mmHg for 1h per day caused a temporary increase in the ONH depression, similar to what we observed in earlier acute IOP elevation studies[29], [183]. The fact that the ONH depression recovered to pre-loop values after removal of the loop indicates that the mechanical deformation of posterior segment structures caused by the elevated IOP did not reach the tissue elastic limit, associated with permanent extracellular matrix change[13]. In this 2-month study, we observed that the ONH depression during IOP elevation increased over time and was on average ~172% larger on week 9 compared to baseline (week 1). This increase in compliance during the loop wear suggests possible permanent changes in the mechanical properties of the posterior segment tissues that include the retina, ganglion cells axons, as well as the supporting connective tissues, and the peripapillary sclera[13]. This hypothesis is supported in part by the axonal degeneration (5.7%) and axonal loss (~5%) observed in the histological optic nerve preparations obtained from 4 animals at the end of our chronic study (Fig. 5). The 5% axonal loss we measured agrees well with the 7% axonal loss observed in other studies after 6 weeks of intermittent IOP elevation using the loop method shown by Joos et al.[30]. Likewise, deformation of the optic nerve head and changes in the peripapillary scleral thickness associated with constantly elevated IOP have been reported in the past[9], [13], [44], [60]. Burgoyne et al.[221] showed higher ONH compliance after 5-9 weeks of constant IOP elevation by laser treatment of the trabecular meshwork, and early-stage ONH damage and ONH compliance as early as 1-2 weeks following constant IOP elevation. By

using confocal scanning laser tomography and 3D reconstruction, Ivers et al.[10] and Yang et al.[44] confirmed hyper-compliance of the ONH and the connective tissue in glaucomatous monkey, when IOP was elevated by laser treatment to the trabecular meshwork. Results from all of those studies are consistent with the progressive change in the ONH depression during continued intermittent 1 hr IOP elevation observed in our study non-invasively with the UHR-OCT system.

Recently, our group reported temporary increase of the scotopic ERG a-wave and b-wave amplitudes associated with acute, 1h elevation of the IOP to 35 mmHg in different strains of rats using the vascular loop procedure[183]. A different study from our group also showed that this temporary increase in the amplitudes of the scotopic ERGs is associated with acute elevation of the IOP in several rat strains[222]. Although the exact physiological origins of the several-fold increase of the amplitudes of the ERG is not exactly known, it is potentially related to increased cellular activity in the retina in response to IOP insults. A similar effect has been observed in other animal studies[111], [146], where ERG b-wave increased after acute IOP elevation with microbeads injection[111], and after chronic IOP elevation with combined microbeads and sodium hyaluronate[146]. Results from our 2-month study presented here confirm that both the ERG a- and b-wave amplitudes are significantly higher during IOP elevation relative to the pre-and post-loop measurements. Other research groups observed decreases in the amplitudes of scotopic ERG a- and b-waves, and OPs with a constant IOP elevation in rodents, sustained for a prolonged period of time[10,11-12,14–17]. Specifically, Grozdanic et al.[211] reported ~25% and ~40% decrease in the scotopic ERG a-wave and b-wave amplitudes respectively in mouse retinas after 6 weeks of sustained IOP elevation using laser treatment of the trabecular meshwork and ICG dye injection.

Liu el al.[34], [212] and Zhao et al.[73] used a circumlimbal suture to induce mild, constant IOP elevation. Two weeks showed no significant changes in the ERG photoreceptor a-wave and bipolar b-wave amplitudes; however, a significant reduction of the ERG photoreceptor a-wave and bipolar b-wave were observed as early as week 4[34] and week 8[212] of the study, respectively. Moreover, OP amplitudes did not change significantly after 12 weeks of IOP elevation between 19-33 mmHg by circumlimbal suture while photoreceptor a-wave and bipolar b-wave reduced significantly at the same time point[73]. These studies showed that there are permanent structural and functional changes of the retina associated with constant moderately high IOP elevation over a prolonged period of at least 4 weeks.

To investigate the potential effect of the loop wear associated increase in the axial eye length on the ERG metrics, a simple mathematical model of the rat eye was created. As a first approximation, the model assumed that under normal pressure (10 mmHg), the rat eye has a slight elliptical shape[224] with transverse length of 6.41 mm, and that the volume of the eye is conserved during elevated IOP. From the SS-OCT data, we determined that for IOP of 35 mmHg, the lateral eye length decreased to 6.26 mm. The optical design of the custom visual stimulator integrated with the UHR-OCT imaging probe focused the stimulus light at the pupil plane with an angular spread of ±45°. Based on our theoretical model of the rat eye and taking into account both the increase in the axial eye length and the change in the corneal curvature during loop wear, we determined that elevation of the IOP to 35 mmHg causes only ~11% increase in the illuminated area of the retina. However, since the energy of the visual stimulus beam was constant, the luminance level at the retina decreased with the increase of the illuminated area. The 11% increase in the visually stimulated area of the retina is insufficient to account for the approximately 4x increase in the

amplitudes of the ERG a-wave and b-wave amplitudes. This fact supports our hypothesis that the observed increase in the ERG amplitudes is most likely due to a physiological response of the retina to the mechanical stress introduced by the loop wear.

In this study, no significant change of the pre-loop retinal function was observed within the 9-week period of chronic intermittent IOP elevation. One possible explanation for these results is that the integral exposure time of the retina to elevated IOP in our study was 48h (8 weeks x 6 days/week x 1h/day) which was significantly less than the total exposure time for other studies[34], [36], [39], [64], [73], [211], [212] that demonstrated permanent structural and functional changes in the retina associated with elevated IOP, as cumulative IOP exposure time is closely related to the extent of retinal damage[225]. The fact that we observed a trend towards a decrease over time in the peak amplitudes of the ERG a-wave, b-wave and the OPs during the loop-on procedure (Fig. 5.4) suggests that there is a change of the retinal function that is more pronounced and therefore measurable when the retinal tissue is under mechanical stress (elevated IOP). This functional change may be related to the 5% axonal loss and reduced mechanical strength suggested by OCT. While the exact mechanism of attenuated retinal function in response to IOP elevation is not fully understood, He et al.[181], [226] suggested that changes in the retinal function susceptibility to acute IOP elevations maybe related to chronic hypertension and blood pressure. Although the relationship between IOP and arterial hypertension is complex, several studies have demonstrated that IOP elevation could modify the retinal blood pressure and indirectly affect retinal function[43], [227]–[229]. Results from our study showed that there were no differences across the weeks in the baseline recordings (prior to any IOP elevation) in both the treated and untreated

eye. However, it should be noted that the effect sizes were affected by the small samples observed and thus the results should be interpreted cautiously.

5.5 Conclusion

In conclusion, results from this chapter show that chronic intermittent IOP spiking to moderate levels over a limited period of time (8 weeks) leads to temporary changes in the retinal function and the ONH shape, that are observed only for the duration of the IOP elevation. The fact that the ONH depression assessed during loop wear change increases progressively with time suggests that there is some early damage to the retinal structure and function that is only pronounced and therefore measurable at elevated IOP when the retinal and ONH are under mechanical stress. This hypothesis is supported by the observed permanent degeneration and loss of ganglion axons in the ONH.

Chapter 6 Neurovascular coupling in the healthy rat retina

Notes and Acknowledgement

This chapter summarizes results from a study that investigated the neurovascular coupling (correlation of visually evoked changes in the retinal blood flow and function) in the healthy rat retina with the combined OCT+ERG system. The content of this chapter is based on a journal manuscript:

B. Tan, E. Mason, B. Maclellan and K. Bizheva. "Measurement of neurovascular coupling in rat's retina measured with combined Functional Doppler Optical Coherence Tomography (fDOCT) and electroretinography (ERG)," *Investig. Ophthalmol. Vis. Sci.*, 2017.58:1673–1681. DOI:10.1167/iovs.17-21543.

Author contributions

Bingyao Tan and **Kostadinka Bizheva** conceived the study.

Kostadinka Bizheva provided the study material.

Bingyao Tan collected all data, and **Erik Mason** helped with the animal monitoring.

Bingyao Tan and **Benjamin MacLellan** wrote the algorithm for temporal blood flow quantification.

Bingyao Tan analyzed the data and wrote the first draft of the manuscript.

Kostadinka Bizheva contributed to the interpretation of the results.

All authors contributed to the final version of the manuscript.

6.1 Introduction

Visual stimulation of the retina evokes neurovascular activity such as neuronal activation, which results in higher cellular metabolic demand and subsequent temporary vasodilation and blood flow

increase, termed functional hyperemia. Potentially blinding ocular diseases, such as glaucoma and DR can cause both temporary and permanent changes in the structure, blood perfusion and functional response of the retina[23], [230], [231]. Retinal blood flow (RBF) changes in response to visible light stimulation have been measured and studied in the past in both healthy and diseased retinas with a variety of optical methods such as the blue field entoptic method[232], scanning laser Doppler flowmetry[233], fluorescence based angiography[234] and fluorescence microspheres[235]. Because these methods have limited temporal resolution, they are not able to provide information about the rapid communication between visually stimulated retinal neurons and neighboring blood vessels. Two-photon microscopy[236] and functional magnetic resonance (fMRI-BOLD)[170] offer both high temporal and high spatial resolution and have been used in the past to image and quantify RBF changes in response functional stimuli. Because both methods rely on tracking the motion of red blood cells in individual blood vessels, measurements are limited to very small regions of the examined retinal tissue.

Recently, OCTA was used to investigate detectable changes in the retinal microvasculature density in response to visual stimulation in rodents and human subjects[91], [237]–[240]. Doppler OCT utilizes phase information to detect and quantify blood flow in retinal blood vessels and provides an alternative method for investigation of neurovascular coupling *in vivo*. In general, Doppler OCT averages multiple cross-sectional images (B-scans), acquired from the same location to measure blood flow rates in biological tissue. Therefore, by utilizing broad-bandwidth light sources and high speed cameras or tunable lasers, both high spatial and temporal resolution Doppler OCT imaging data can be acquired, which enables the investigation of the rapid vascular response of the retina to visual stimulation. Total axial RBF in the retina can be calculated from circular

Doppler OCT scans centered at the ONH by averaging over the blood flow in all retinal blood vessels in the B-scan. All of the previous Doppler OCT or OCTA studies mentioned above used very long duration (10s to 2.5 minutes) of either single flash or flicker stimuli. It would be of interest to determine what is the shortest possible stimulus duration that can evoke changes in the RBF that are measurable with Doppler OCT, to correlate the RBF changes with changes in the retinal neuronal activity, as well as to investigate any difference in the retinal response to flicker and single flash stimuli of the same intensity and color.

ERG records the electrical activity of visually stimulated retinas and therefore provides a way to measure the visually evoked cellular response from different types of retinal cells with millisecond scale time resolution. By combining information obtained from ERG recordings and Doppler OCT measurements, a more complete model of the neurovascular coupling in the visually stimulated retina can be generated. Previous studies have shown that flicker ERG traces and the first two harmonic components of ERG recordings are indirectly correlated to changes in the retinal blood flow in response to visual stimuli[241], [242]. However, the ERG and Doppler OCT data in those studies were not recorded simultaneously and the stimuli durations ranged from 10s to 2.5 minutes. In this study we used a combined Doppler OCT and ERG system (DOCT+ERG) to measure simultaneously with high spatial and temporal resolution visually evoked changes in the retinal neuronal activity and RBF, as well as to determine the shortest single flash stimuli that would induce a measurable change in the RBF. Furthermore, in this study we investigate the magnitude,

latency and recovery rate of the RBF as a function of the stimulus type, intensity and duration.

6.2 Methods

6.2.1 Animal and anesthesia

Eight-week-old, male, Brown Norway rats (n = 6, Harlan Laboratories Inc., Indianapolis, USA), weighing ~250 g were used for this study. The animals were kept at a 12h light/dark cycle and dark adapted for at least 12 hours prior to the experimental sessions. The rats were anesthetized with ketamine/xylazine cocktail (0.2ml/100g body weight) that was delivered intraperitoneally. Subcutaneous injections of 5ml sterile saline were administered immediately after the ketamine injection and about every 1 hour afterwards to keep the animal well hydrated. The rats were placed on a custom stereotactic stage to reduce head motion artefacts and allow for translational and rotational alignment of the imaged eye with respect to the DOCT+ERG system's imaging probe. During the experimental procedures the animals were kept at 38°C with a thermal pad placed under belly (Kent Scientific). One drop 0.5% proparacaine hydrochloride (topical anesthetic; Alcaine, Alcon) was applied to the imaged eye, followed by one drop of 0.5% tropicamide (pupillary dilator; Alcon). Artificial tears were applied every 5 minutes to keep the cornea well hydrated and optimize the impedance match between the cornea and the ERG corneal loop electrode. Metacam (2ml/100 body weight diluted in sterile water) was administered for pain relief after completion of the experiments to help with the animal recovery. All experiments described here were approved by the University of Waterloo Animal Research Ethics Committee and adhered to the ARVO

Statement for Use of Animals in Ophthalmic and Vision Research.

6.2.2 Doppler OCT+ERG system

A research-grade, spectral domain OCT system, designed and built by our group for various imaging studies of the rodent retina[185], [243], [244] was modified for use in this study (Fig. 6.1). Briefly, a broad bandwidth SLD (λ_c = 1020 nm, $\Delta\lambda$ = 110 nm, P_{out} = 10 mW, Superlum Ltd, Ireland) was used to achieve 3 µm axial resolution in retinal tissue and ensure that the Doppler OCT (DOCT) imaging beam does not visually stimulate the retina. The DOCT retinal imaging probe, comprised of 3 broadband NIR achromat doublet lenses (f_1 = 10 mm, f_2 = 60 mm, and f_3 = 30 mm; Edmund Optics, Barrington, NJ, USA) and a pair of galvanometric scanners (Cambridge Technologies, Bedford, MA, USA), was designed to deliver a collimated imaging beam of 1.5 mm diameter and 1.7 mW optical power to the rat cornea, thus achieving ~5 µm lateral resolution in retinal tissue. A high resolution spectrometer (P&P Optica, Waterloo, Canada) and a NIR line scan camera (1024-LDH2 92 KHz, Sensors Unlimited, USA) were used at the detection end of the DOCT system. A commercial ERG system (Diagnosys LLC, USA) was interfaced with the DOCT system and the data acquisition was synchronized to allow for simultaneous DOCT and ERG recordings. A new, custom built visual stimulator that utilizes a white light LED was integrated into the DOCT retinal imaging probe. Light from this LED was focused at the pupil plane (Fig. 6.1, green line) of the rat eye to generate almost uniform, Maxwellian illumination of the retinal surface. The illumination intensity and the temporal pattern of the LED were controlled from the

ERG system's console.

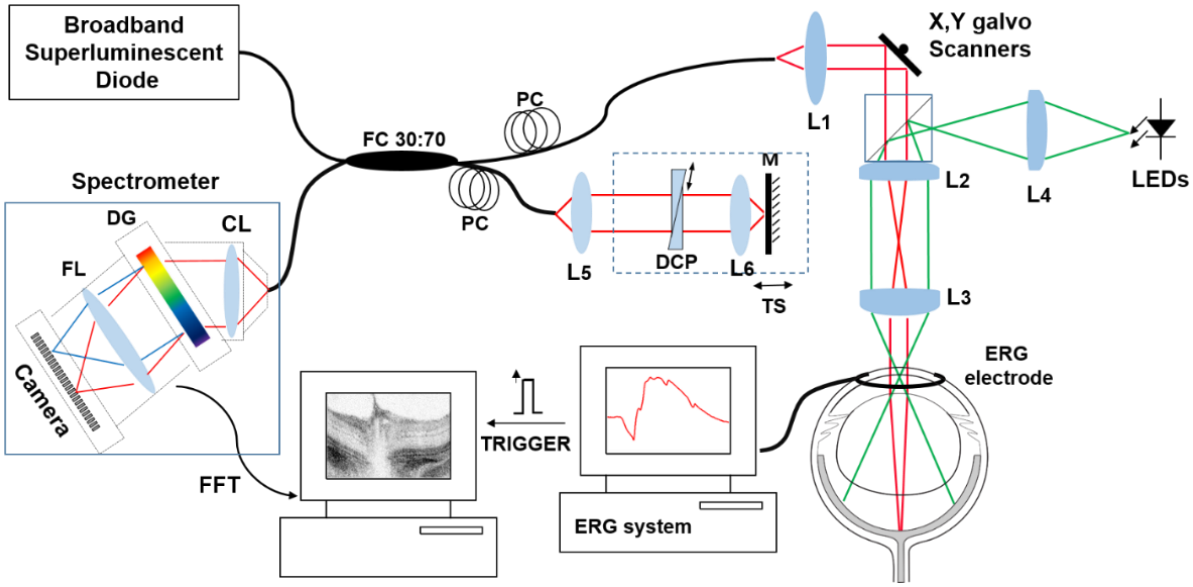

Figure 6.1 Schematic of the combined OCT+ERG system. L1-L6 achromatic doublet lenses; TS-translation stage; M-reference mirror; FC-fiber coupler; DCP-dispersion compensation prisms, PC-polarization controller, CL-collimator lens; DG-dispersion grating; PDA-linear photodiode array; FFT-Fast Fourier transform.

6.2.3 DOCT and ERG measurement protocols

A volumetric (1000 x1000 x 1024) morphological image of the rat retina was acquired from the region around the ONH in each animal prior to conducting the visual stimulus tests (representative image shown in fig. 6.2A). Subsequently, multiple DOCT cross-sectional images (4000 x 1024) were acquired continuously from a circular pattern centered at the retinal ONH at the rate of 12 fps. The diameter of the circular DOCT scan was set to ~0.8mm (Fig. 6.2B) to allow for visualization of cross-sections of the retinal arteries and veins in the vicinity of the ONH and to avoid the necessity of phase unwrapping in the calculation of the axial RBF. The axial RBF velocity was calculated from the phase difference between adjacent A-scans in the circular cross-sectional DOCT images. A representative cross-sectional circular OCT scan with color coded blood vessels is shown in Figure 2C. One hundred repeated OCT frames (total acquisition time of

~8.5s) were acquired to track the axial blood flow velocity over time in response to the stimuli. The DOCT data was acquired simultaneously with the ERG recordings.

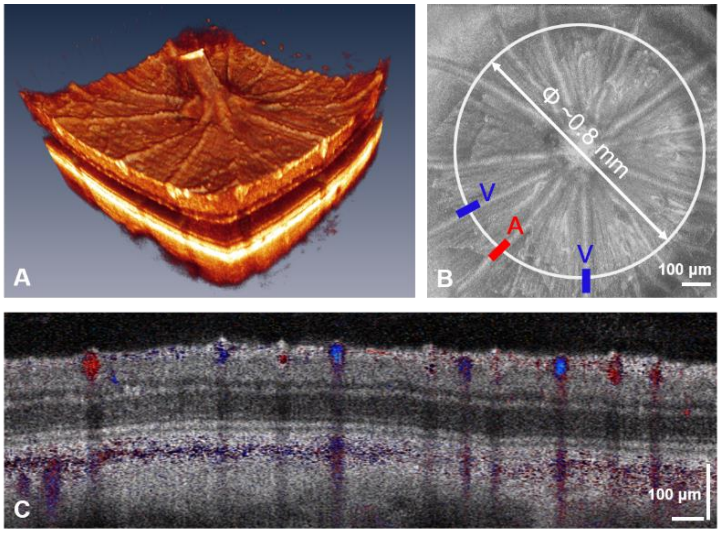

Figure 6.2 (A) Volumetric OCT image of the rat retina centered at the ONH. (B) Enface projection of the retinal OCT image. The white circle marks the DOCT scanning pattern with diameter Ø ~0.8 mm. The major retinal blood vessels are identified (V – vein and A – artery). (C) Circular cross-sectional OCT image of the retinal structure and blood vasculature.

The positive ERG electrode (a 4.5mm diameter silver wire loop) was placed gently on the rat cornea to ensure clear aperture for the DOCT imaging and visual stimulus beams. The negative and reference needle ERG electrodes were placed under the skin behind the rat's ears. Single flash (10 ms and 200 ms duration, 1.14 log scotopic cd·s/m^2) and flicker (10Hz, 20% duty cycle, 1s and 2s duration, 1.14 and 0.80 log scotopic cd·s/m^2) visual stimuli were projected onto the retinal surface. The duration of each ERG recording was 8.5s with 1s pre-stimulus baseline. For each type (single flash or flicker) of the visual stimulus and stimulus settings (intensity and duration), 5 ERG recordings were acquired with 5 min dark adaptation period in between. At least 15 min dark adaptation period was used between consecutive sets of recordings, acquired with different settings

of the visual stimulus

6.2.4 Doppler OCT data analysis

A sub-pixel registration algorithm[245] was used to correct for any bulk motion between neighboring OCT B-scans prior to segmentation of the retinal blood vessels. The retinal blood vessels were manually selected and the axial blood flow was calculated by integrating the blood velocity over the selected blood vessel area. Arterial and venal blood flow was calculated separately due to the different polarity of the respective phase changes. Total axial RBF was determined as an average of the magnitudes of the arterial and venal RBF. A moving window smoothing algorithm (Savitzky-Golay) was used to filter out oscillations in the temporal DOCT recordings due to pulsatile blood flow. Figure 6.3A shows a representative recording of the RBF measured from one retinal blood vessel over time (black line). The red line shows the filtered RBF recording after removal of the pulsatile oscillations. Figures 6.3B and 6.3C show the spatial distribution of the measured phase changes within the blood vessel's cross-section before (t = 0.8 s) and after (t = 3 s) application of the visual stimulus respectively. Fractional changes in the RBF induced by the visual stimuli were calculated relative to the pre-stimulus (baseline) part of the recording. A Student's t-test was used to determine the significant changes in the RBF peak

amplitude and latency for the different settings of the visual stimuli.

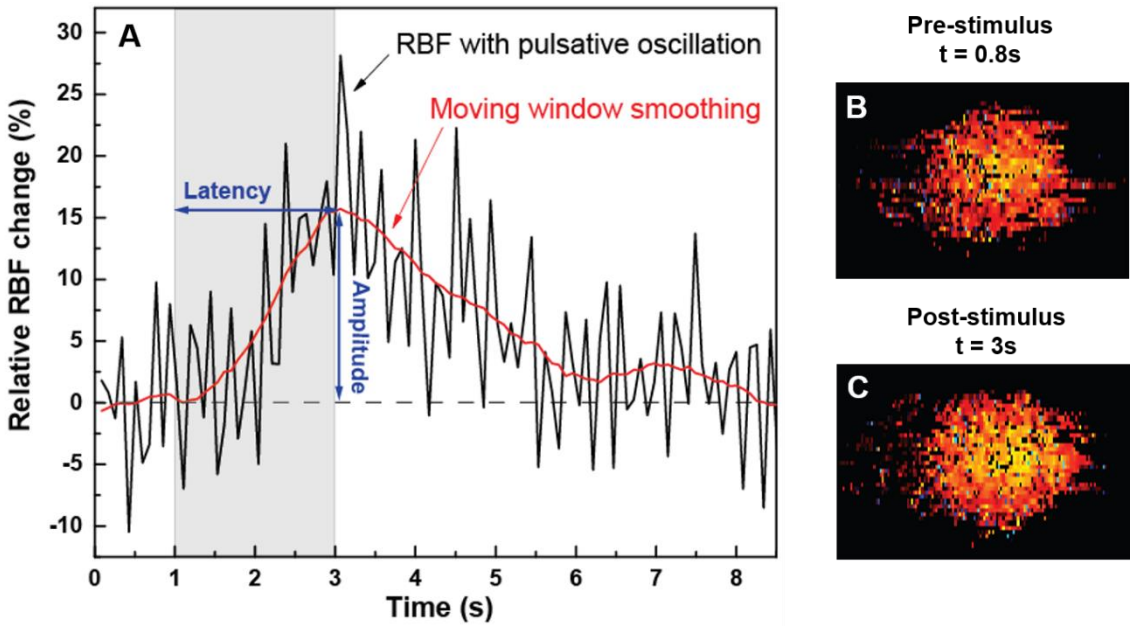

Figure 6.3 (A) Total axial RBF change as a function of time for a 2s flicker stimulus (grey area). The original RBF data (black line) shows pulsatile oscillations due to the animal heart rate. Filtered RBF data are shown in red. Spatial distribution of the DOCT signal within the cross-section of a retinal blood vessel at prior to (B) and post visual stimulation (C).

6.2.5 ERG data analysis

Analysis of the single flash and flicker ERG recordings followed the International Society for Clinical Electrophysiology of Vision (ISCEV) standards[246]. For single flash ERG recordings, the amplitude and latency of the a-wave and b-wave were determined. For flicker ERG, the amplitude was calculated as averaged voltage differences between peaks to troughs, excluding first two peaks.

6.3 Results

Figure 6.4 summarizes results from measurements conducted with the 10- and 200-ms single and continuous flash stimuli. Representative ERG traces are shown in Fig 6.4A with the gray and yellow marked areas corresponding to the duration of the visual stimuli. Fig 6.4B shows the total

axial RBF, averaged over all recordings from all animals, as a function of time. For the same stimulus intensity, the 200-ms flash resulted in 5X larger RBF peak magnitude compared to the 10-ms flash, though no significant change in the latency of the RBF peak between the two stimulus durations was observed. Although the 10-ms single flash stimulus generated measureable changes in the RBF, no reproducible changes in the RBF were measured with 10-ms single flash stimuli with intensity <1.14 log scotopic cd·s/m^2, or with stimuli with 1.14 log scotopic cd·s/m2 and duration shorter than 10 ms. Figure 6.4C presents normalized averaged total axial RBF for the two single flash stimuli, which shows that there are no significant differences in the stimulation and recovery rates of the RBF (positive and negative slopes of the RBF peak). Fig 6.4D shows statistical correlation between the changes in the RBF and the ERG b-wave magnitude for the 10- and 200-ms single flash stimulus durations. Although the RBF peak magnitude showed significant differences for the two flash durations (P = 0.023), the ERG a-wave and b-wave magnitudes showed no significant differences between the two flash durations (P=0.256 and P=0.056, respectively).

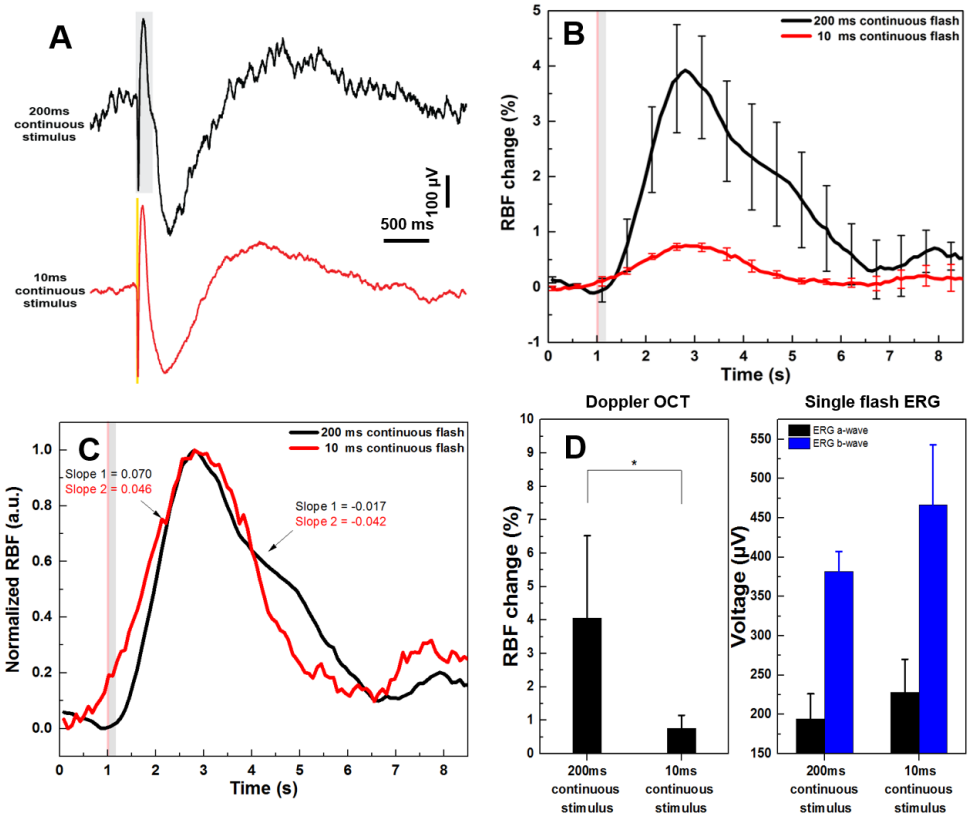

Figure 6.4 Effect of single flash stimulus duration. (A) Representative ERG traces acquired with 10 ms and 200 ms single flash stimulus duration. (B) Total axial RBF as a function of time for the 10 ms and 200 ms single flash stimuli, averaged over all recordings from all animals. (C) Normalized RBF data showing differences in the recovery rate for the 2 stimulus durations. (D) Comparative statistics for the maximum RBF change and the ERG b-wave magnitude data for the two stimulus durations. The "*" denotes significant difference between the two groups of data and the data is presented as mean ± SD.

Figure 6.5 summarizes results from the tests with flicker stimuli of different duration. The gray and pink shaded areas correspond to the duration of the visual stimuli. Figure 6.5A shows representative ERG traces for 1- and 2-second long flicker stimuli. Figure 6.5B shows the total axial RBF, averaged over all recordings from all animals, as a function of time. Although the 1-second flicker stimulus results in ~8% RBF peak change compared to ~10% for the 2-second flicker stimulus, the difference in the peak RBF magnitudes are not statistically significant (P=0.169, Fig. 6.5D). Statistical results also showed no significant differences in the ERG b-wave

magnitude (P=0.086). Also, there is no significant difference in the latency of the RBF peak for the 1- and 2-second flicker stimuli. Normalized RBF recordings for the 1- and 2-second flicker stimuli are shown in Figure 6.5C. Although there is no significant difference in the RBF rate of increase with the application of the visual stimulus, the RBF recovery rate is ~3X faster for the 1-second stimulus compared to the 2-second flicker stimulus of the same intensity.

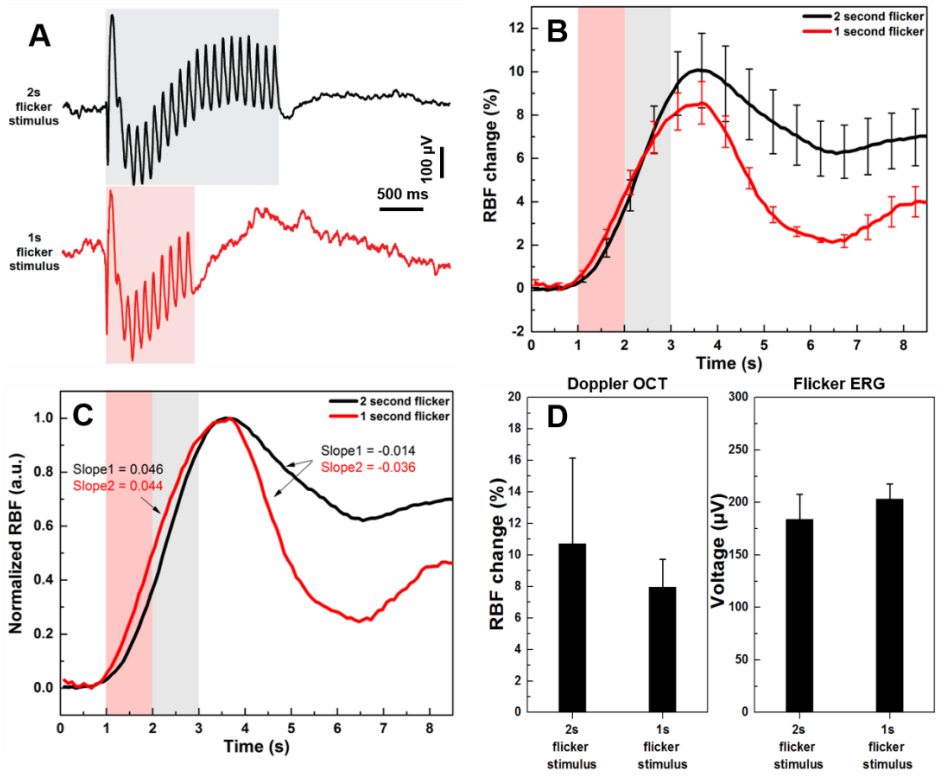

Figure 6.5 Effect of flicker stimulus duration. (A) Representative ERG traces acquired with 1s and 2s flicker stimulus duration. The pink and grey shaded areas mark the duration of the visual stimuli. (B) Total axial RBF as a function of time for the 1s and 2s flicker stimuli, averaged over all recordings from all animals. (C) Normalized RBF data showing differences in the recovery rate for the 2 stimulus durations. (D) Comparative statistics for the maximum RBF change and the ERG b-wave magnitude data for the two flicker stimulus durations. The data are presented as mean ± SD.

Figure 6.6 summarizes results from the tests with 2-second long flicker stimuli of different intensities (1.14 and 0.80 log scotopic cd·s/m^2). Figure 6.6A shows representative ERG traces for the flicker stimuli of different intensities. The total axial RBF, averaged over all recordings from

all animals, as a function of time, is shown in Figure 6.6B. The brighter flicker stimulus resulted in significantly higher RBF peak magnitude compared to the stimulus of lower intensity (P= 0.0471, Fig. 6.6D); however, there was no significant difference in the RBF peak latencies for the two stimuli. Statistics of the ERG data (Fig. 6.6D) shows that the flicker ERG magnitude is larger with higher flicker stimuli intensity (P=0.020). Normalized RBF recordings for the 1- and 2-second flicker stimuli are shown in Figure 6.6C. Although there is no significant difference in the RBF rate of increase with the application of the visual stimulus, the RBF recovery rate is ~50% faster for the low intensity stimulus.

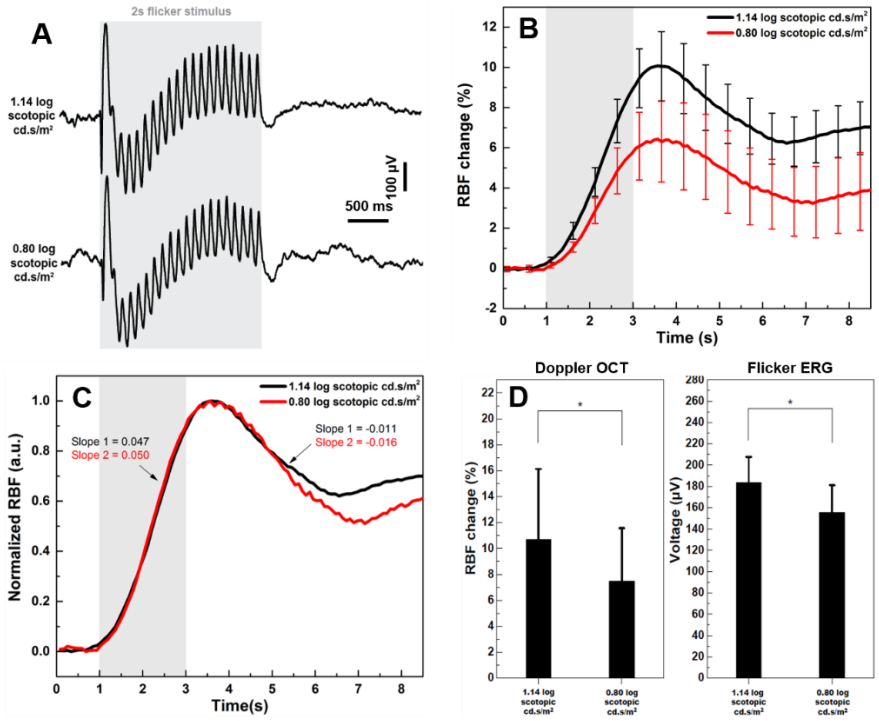

Figure 6.6 Effect of flicker stimulus intensity. (A) Representative ERG traces for the flicker stimuli with different intensities. (B) Total axial RBF change as a function of time, for the two stimulus intensities, averaged over all recordings from all animals. (C) Normalized RBF data showing differences in the recovery rate for the 2 stimulus intensities. (D) Comparative statistics for the maximum RBF change and the ERG b-wave magnitude data, presented as mean ± SD for the two flicker stimulus intensities. The "*" denotes significant difference between the two groups of data.

Figure 6.7 shows results from a comparative analysis between the 200-ms single flash and the 1-second flicker stimuli. Since in our studies we used 10-Hz flicker with 20% duty cycle, each cycle of the flicker stimulus corresponds to 20-ms long continuous flash. Therefore, the 1-second flicker has the same average photon energy as the 200-ms single flash. Figure 6.7B shows representative ERG traces for the 200-ms single flash and 1-second flicker stimuli. The total axial RBF, averaged over all recordings from all animals, as a function of time is shown in Figure 6.7B. The 200-ms single flash stimuli induced ~2X smaller RBF peak magnitude change compared to the 1-second flicker stimulus (4.1 ± 2.4% vs. 8.0 ± 1.7%, $P = 0.034$). Furthermore, the single flash stimulus had ~25% smaller latency (1.7 ± 0.2 seconds vs. 2.1 ± 0.1 seconds, $P < 0.001$). Figure 6.7C presents normalized RBF traces for the single flash and flicker stimuli. Although the single flash stimulus has ~2X faster rate of the RBF increase, it also shows ~2X lower recovery rate compared to the flicker stimulus. Statistical results for the RBF peak magnitude and latency for the two types of visual stimuli are presented in Figure 6.7D. These results show that regardless of the fact that the overall photon energy delivered to the retina by the 200-ms single flash and 1-second flicker stimuli is the same, differences in the RBF peak magnitude and latency for the different stimuli types are significant (marked with ‘‘*’’ and ‘‘†’’ in Figure 6.7D, respectively).

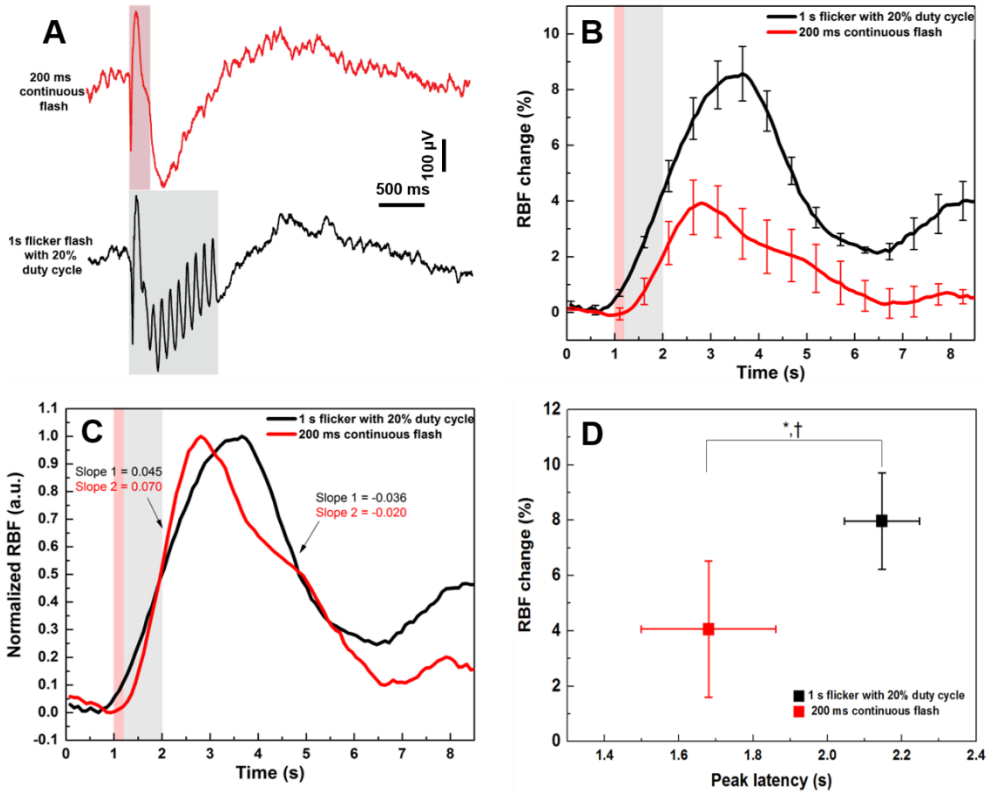

Figure 6.7 Comparison of the changes in the total axial RBF and the ERG b-wave magnitude resulting from 200 ms single flash and 1s, 10Hz, 20% duty cycle flicker stimuli of the same illumination intensity. (A) Representative ERG traces. The pink and grey shaded areas mark the duration of the visual stimuli. Original (B) and normalized (C) time recordings of the total axial RBF in response to the single flash and flicker stimuli. (D) Peak latency and amplitude statistics for the RBF data, where "*" and "†" denote significant differences in the RBF peak amplitude and latency respectively, between data acquired with the single flash and flicker stimuli. The data are presented as mean ± SD.

6.4 Discussion

Results from our study on the flicker-induced RBF changes agree in general with results from similar studies conducted by other research groups with different imaging methods. Specifically, Kornfield et al.[247] observed 11% increase in the superficial RBF following 2s flicker stimulation by using functional MRI (BOLD), which compares well with the ~10% increase we measured with DOCT for flicker stimulus of the same duration. Radhakrishnan et al.[248] reported ~12% blood flow increase for a 10s flicker stimulus using *en-face* Doppler OCT, while Werkmeister et al.[249]

detected over 30% increase of blood flow with 60s flicker stimulus using DOCT. Results from our study agree with the general trend established by all of these studies that longer duration of the flicker stimulus contributes to larger peak magnitude of the RBF and that the time of RBF return to baseline is directly proportional to the flicker stimulus duration. One new and significant result from our study is that we showed for first time that DOCT is able to measure reproducibly RBF changes in response to much shorter flicker stimuli (1s compared to 10s or 60s). Furthermore, we have shown for the first time correlation between the visual stimulus-induced RBF and the flicker ERG magnitude.

Results from our study also showed that DOCT is able to measure reproducibly changes in the RBF in response to continuous visual stimuli with duration as short as 10ms. However, as demonstrated by the results in Figure 6.7, single flash and flicker stimuli of the same lux generate different response of the RBF. Almost 2x larger RBF peak magnitude was measured with the flicker stimuli, which indicates that retinal neurons respond differently to the frequency content of the visual stimulus. Our results correlate well with results from other studies conducted with different imaging modalities, that also indicate that flicker stimuli have stronger effect on the neurovascular coupling and vasodilation[26], [233].

The DOCT imaging protocol used in our study was designed to emphasize blood flow measurement from retinal blood vessels located at the RNFL. By changing the image acquisition protocol, it is possible to measure changes in the capillary flux in the inner retina in response to visual stimulation by counting the number of red blood cells passing through the repeated cross-section area[250], [251].

In our study, we utilized ERG to investigate physiological responses of the retina to visual stimuli and to correlate those changes to the RBF changes. Functional OCT has been proven able to image intrinsic optical changes (intrinsic optical signal - IOS) in the retina in response to visual stimuli[177], [252]–[255] . Since the fast IOS changes occur on a millisecond scale, while changes in the RBF occur on the scale of seconds, the DOCT protocol we utilized for our current study was not suitable for simultaneous recording of both IOS and RBF changes with the OCT system. Future development of the OCT technology and image acquisition protocols could make simultaneous recording of stimulus-induced IOS and RBF changes in the living retina feasible.

6.5 Conclusion

In this chapter, we have developed a combined OCT+ERG system to allow for simultaneous measurement of the physiological and blood flow changes in the rat retina induced by visual stimuli. We showed that both single flash and flicker short duration stimuli induce measurable changes in the RBF and demonstrated that DOCT is capable of measuring reproducibly RBF changes from continuous single flash stimuli as short as 10ms.

Chapter 7 Neurovascular coupling in the rat retina with acute IOP elevation

Notes and Acknowledgement

This chapter summarizes results from a study that investigated the neurovascular coupling (correlation of visually evoked changes in the retinal blood flow and function) in the healthy rat retina for moderate level elevated IOP with the combined OCT+ERG system. This chapter is based on a journal manuscript:

B. Tan, E. Mason, B. MacLellan and K. Bizheva. "The Effect of Acutely Elevated Intraocular Pressure on the Functional and Blood Flow Responses of the Rat Retina to Flicker Stimulation," *Investig. Ophthalmol. Vis. Sci. (in revision).*

Author contributions

Bingyao Tan and **Kostadinka Bizheva** conceived the study.

Kostadinka Bizheva provided the study material.

Bingyao Tan conducted the study, and **Erik Mason** helped with the animal monitoring.

Bingyao Tan wrote the algorithm for TRBF and blood vessel size quantification.

Bingyao Tan analyzed the data and wrote the first draft of the manuscript.

Kostadinka Bizheva contributed to the interpretation of the results.

All authors contributed to the final version of the manuscript.

7.1 Introduction

Glaucoma is a chronic disease associated with progressive dysfunction of the RGCs[256], [257], reduction of the retinal blood flow[258], thinning of the RNFL[259] and deformation of the optical

nerve head (ONH)[13]. It is the second leading cause of blindness worldwide, with an estimate of 64.3 million people between the ages of 40 to 80 years affected in 2013, 76.7 million by 2020, and 111.8 million by 2040[1]. Currently, there is no cure for glaucoma and any clinically available pharmaceutical or surgical approaches to treating the disease can only slow its progression. Therefore, early detection and treatment are essential for managing the glaucoma progression elevated IOP is one of the most well studied and documented pathogenic risk factors for OAG[104], [106], [259], and as such, numerous animal models have been developed to study the acute and chronic IOP elevation effect on ONH structure[9], [27], [45], [46], [221], retinal blood perfusion[58], [176], [198] and ganglion cell function[35], [53], [73], [130].

Currently RNFL thinning and ONH deformation are used as some of the major markers for clinical diagnostics and treatment monitoring of glaucoma; however, these morphological retinal changes develop over a fairly long time to the extent that they are measurable by ophthalmic imaging modalities. More recent studies have shown that glaucoma patients exhibit reduced flicker-induced blood flow changes and vasodilation compared to healthy subjects[18]–[20], [22], [23]. Specifically, Riva[18] used laser Doppler flowmetry reported that the retinal blood flow (RBF) response at the optic disc rim to flicker stimulation is significantly reduced in early OAG and ocular hypertension patients. Similarly, Gugleta and colleagues[22], [23] conducted a study using a retinal vessel analyzer and reported attenuated flicker-induced vasodilation in early glaucoma and ocular hypertension patients. Garhöfer[19] used retinal vessel analyzer to show that vasodilation in retinal veins in response to flicker stimulation is greatly diminished in early glaucoma patients. Results from those studies suggest that visually-evoked retinal blood vessels vasodilation and changes in the retinal blood flow may serve as sensitive markers that would allow

for early diagnostics of glaucoma.

So far, various imaging modalities have been used to investigate the neurovascular coupling in the retina, including the blue field entoptic method[232], laser Doppler velocimetry[260], fluorescence microspheres[235] and functional MRI(BOLD)[247]. Over the past few years, Doppler OCT and OCTA have gained significant clinical importance for clinical diagnostics and treatment management of various retinal diseases including glaucoma[261]. Different OCT system designs and/or image acquisition protocols have been utilized in methods such as the *en-face* integration[187], the double concentric circle method[262] and the multi-directional beam[89], developed for accurate retinal total blood flow measurements in human subjects and animal studies.

Doppler OCT was also used to measure changes in the RBF in response to flicker stimulation in both humans and animals[237], [238], [248], [249], [263]. Recently, our research group has developed a combined optical coherence tomography and electroretinography (OCT+ERG) system that allows for examination of the neurovascular coupling in the rat retina[178]. A study conducted with this system in healthy rats under normal IOP, showed that flicker-induced changes in the RBF are time-correlated with amplitude and latency changes of the ERG traces.

Here we present results from a study that used the OCT+ERG system to examine the effect of acutely elevated IOP on the functional and blood flow responses of the rat retina to flicker stimulation.

7.2 Methods

7.2.1 Animal and anesthesia

All experiments described here were approved by the University of Waterloo Animal Research

Ethics Committee and adhered to the ARVO statement for use of animals in ophthalmic and vision research. Male Brown Norway rats (n = 11, Harlan Laboratories Inc., Indianapolis, IN), weighing~ 300 g, were dark adapted for at least 12 hours in a 12/12 light cycle room prior to the experiment. All the other animal preparation details have been discussed in the Section 6.2.1. It is to be noted that the motion artifact is minimized by the selection of anesthesia (ketamine/xylazine) and the stereotactic instruments.

7.2.2 IOP elevation protocol

An adjustable vascular loop (Sentinal Loops; Sherwood-Davis and Geck, St. Louis, MO, USA), placed anterior to the equator of the eye, was used to elevate the IOP in one eye to ~ 45 mmHg for a duration of 30 minutes, following a procedure developed by Joos et al.[30] The IOP was measured with a corneal rebound tonometer (Icare® Tonolab, Tuike, Finland) before placement of the vascular loop, about 10 minutes after placement of the loop, immediately before the OCT+ERG imaging procedure, and about 10 min after removal of the loop.

7.2.3 Doppler OCT+ERG System

A research grade, ultrahigh resolution spectral domain OCT system, combined with a commercial ERG system (Diagnosys LLC, Lowell, MA, USA) was used for this study. The system setup has been described before in Section 6.2.2. Briefly, the OCT system operates in the 1060 nm spectral region and provides ~3 µm axial and ~5 µm lateral resolution in the rat retina, at 92 kHz image acquisition rate. For this study, the camera data acquisition rate was reduced to 47 kHz in order to improve the SNR of the Doppler OCT signal and ensure maximum measurable flow velocity of 8.6 mm/s, sufficient for quantitative blood flow measurements in the rat retina. The OCT imaging

probe was designed to deliver a collimated imaging beam of 1.5 mm diameter and optical power of 1.7 mW to the rat cornea, and was integrated with a custom visual stimulator connected to the commercial ERG system. The visual stimulator was designed to focus the stimulus light at the pupil plane, thus providing a wide angle, uniform Maxwellian illumination of the retina. The intensity and duration of the visual stimuli were controlled from the ERG console and the OCT and ERG data acquisition were synchronized.

7.2.4 Data Acquisition

Doppler OCT and ERG data were acquired immediately after the IOP measurements for the 3 time points of the study: before IOP elevation (pre-loop), during IOP elevation (loop-on) and after loop removal (post-loop). A Doppler OCT scanning protocol based on 2 concentric circular scans centered at the ONH, similar to the protocol proposed by Shahidi[91], was used in our study to determine the Doppler angle necessary for the calculation of the TRBF. Figure 7.1A shows an *en-face* maximum intensity projection morphological image of the rat ONH and vicinity, with colored dashed lines marking the Doppler OCT concentric circular scan pattern ($Ø_1$=0.65 mm, $Ø_2$=0.85 mm). The size of each circular OCT scan was 4000 x 512 (A-scans x pixels) and 5 repetitive scans were acquired consecutively from the same location in the retina. Data with this protocol was acquired prior to the simultaneous Doppler OCT and ERG recordings for each loop phase to determine the Doppler angle between each retinal blood vessel and the OCT imaging beam. A continuously repeated single circle Doppler OCT scan pattern (Ø = 0.75 mm) was used for the simultaneous Doppler OCT and ERG recordings in order to achieve high temporal resolution of 85 ms, sufficient to track the blood flow pulsatile oscillations and the stimulus induced TRBF changes. Each synchronous Doppler OCT and ERG recording lasted 6 s seconds (1 s long pre-

stimulus, 2 s long flicker stimulus and 3 s long post-stimulus period). White light flicker stimulus (10 Hz, 2 s duration, 0.80 log scotopic cd·s/m^2) with 20% duty cycle and 100% modulation depth was used. Five OCT+ERG recordings were acquired for every loop phase, with a 3 minute rest interval between consecutive recordings. For the ERG recordings, the positive loop electrode (Ø = 4 mm) was placed onto the cornea, leaving clear aperture for the OCT imaging beam. Artificial tears (Refresh Tears; Alcon, Mississauga, ON, Canada) were applied to the imaged eye to ensure optimal impedance between the ERG loop electrode and the cornea. The negative electrode needle was placed subcutaneously behind the ear, and the ground electrode needle was placed in the skin between the ears. The ERG system has a 1.5 kHz sampling frequency and a built-in band-pass filter (0.3-300 Hz).

7.3 Data Analysis

7.3.1 OCT Doppler data

Retinal blood vessels in the vicinity of the ONH were manually selected from the single circle Doppler OCT scans and the axial blood flow was calculated by integrating the blood velocity over the selected blood vessel area. Doppler OCT images were calculated by arterial and venal blood flow was calculated separately due to the different polarity of the respective phase changes and only the magnitudes were used for evaluation of the TRBF. In order to compute the TRBF, knowledge of the Doppler angle between the OCT imaging beam and the orientation of each retinal blood vessel was required. In our study, individual blood vessel was segmented manually, and the Doppler angle θ was determined from the shift in location of the retinal blood vessels between the two concentric circular Doppler OCT scans：

$$\Theta = \arccos\left(\frac{\Delta z}{\sqrt{\Delta x^2 + \Delta y^2 + \Delta z^2}}\right)$$

Here, Δy and Δz are the lateral and axial displacements of the blood vessel between the 2 circular scans respectively, and Δx is the distance between the 2 circular scans (200 μm). Figure 7.1A shows on *en-face* maximum intensity projection image of the rat retina with colored dashed lines marking the Doppler OCT concentric circular scans centered at the ONH. Figure 7.1B shows an overlay of the 2 OCT circular tomograms, color coded in violet and green. Figure 7.1C-D show a magnified view of the location in Figure 7.1B marked with the yellow dashed line and demonstrate the shift in location of the major retinal blood vessels between the 2 concentric circular scans, used for the calculation of the Doppler angle. TRBF was calculated by integrating over the total blood flow data for all retinal arteries and veins. A moving window (Savitzky-Golay, window size: 15) smoothing algorithm was used to filter out oscillations in the temporal TRBF recordings arising from pulsatile blood flow. The blood vessel size for all retinal vessels was also determined manually by two researchers by measuring the shadow underneath each vessel in the Doppler OCT images[91]. The 5 repeated concentric circular OCT scans acquired from the same locations in the retina were aligned and averaged in order to reduce speckle noise and thus improve the precision of the BVS analysis.

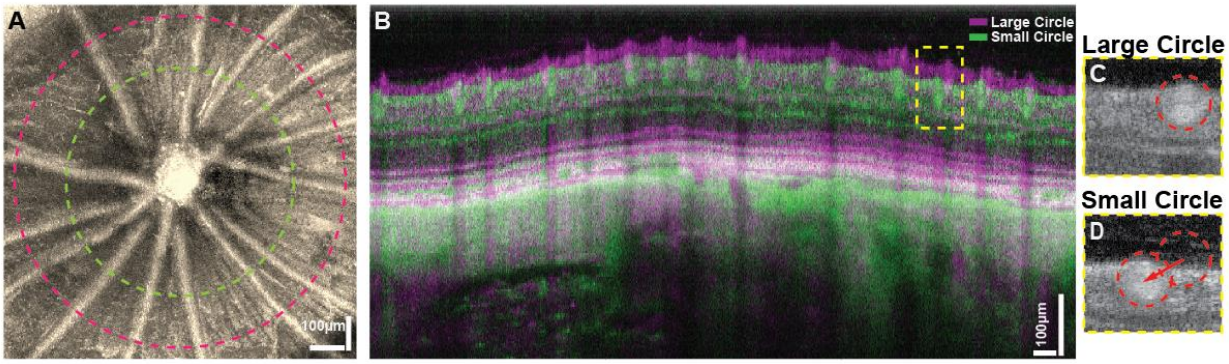

Figure 7.1 Total blood flow analysis. (A) *En-face* image of the ONH with violet and green dashed lines marking the double circle Doppler OCT scanning pattern. (B) Overlay of 2 representative concentric circular OCT scans. (C) and (D) present magnified views of the area in (B) marked with the yellow dashed line, from the large and small diameter circular scans respectively.

7.3.2 Retinal function

ERG traces were averaged over the five recordings for each loop phase. In accordance with the standard for processing ERG recordings[246], the first negative and positive peaks in the flicker ERG trace correspond to the a-wave and b-wave of a single flash response of the retina respectively. Since the magnitude of the second pair of positive and negative peaks can also be affected by the single flash response of the retina, in our analysis, the peak-to-trough difference for the last 8 peaks of the 10 Hz flicker ERG trace was averaged and defined as the flicker ERG amplitude. A Fourier transform was applied to the ERG recordings to extract the FHC (10 Hz) and the SHC (20 Hz), and explore their dependence on the elevated IOP.

7.3.3 Statistics

One-way ANOVA was used to detect any significant differences in all measured parameters such as the IOP, the TRBF, the BVS, the flicker induced changes in the TRBF and the ERG components. Bonferroni-corrected multiple comparison post-hoc tests were applied to determine any significance between the pre-, during, and post-loop conditions. Differences were considered

significant when $p<0.05$. All data in the text are presented as Mean ± SD, while data in all figures are presented as Mean ± SE.

7.4 Results

7.4.1 IOP

The pre-loop IOP was 9.6 ± 1.1 mmHg and when elevated, it stabilized at 43.1 ± 6.8 mmHg after 10 minutes of loop wear ($p<0.01$). After 10 minutes of post-loop recovery, the IOP decreased and stabilized at 7.1 ± 1.1 mmHg ($p<0.01$). There was no significant difference between the pre-loop and post-loop IOP values ($p=0.54$).

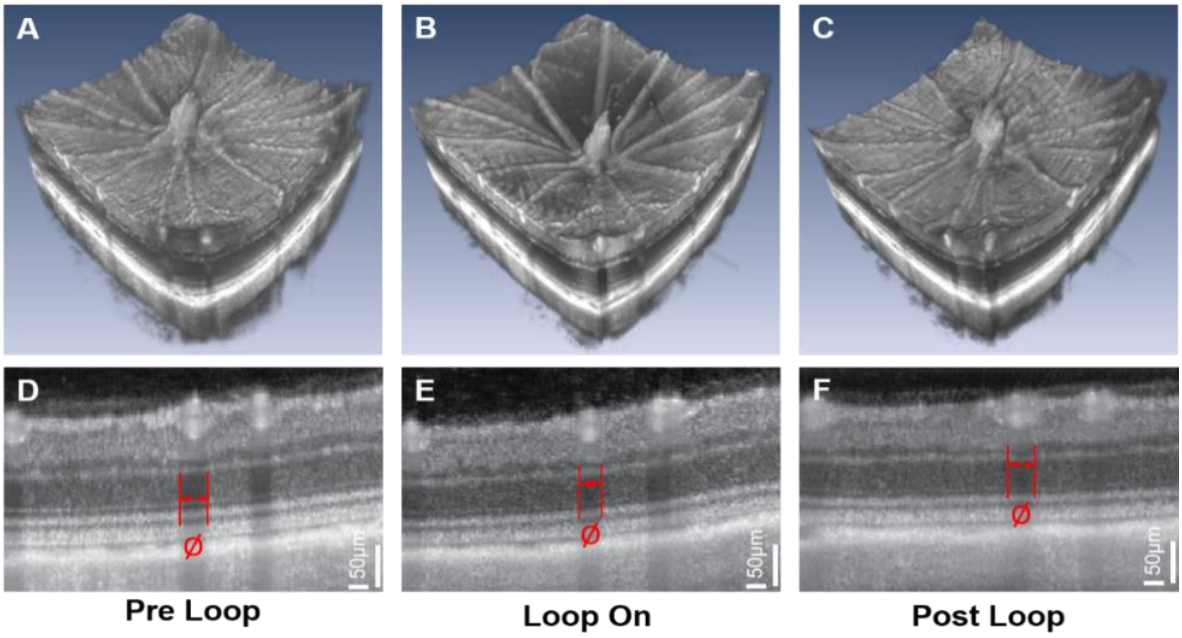

Figure 7.2 Morphological and vascular changes of the ONH induced by the elevated IOP (A-C) Volumetric morphological OCT images of the ONH acquired before, during and after IOP elevation. (D-E) Elevated IOP related changes to the retinal blood vessels diameter evaluated from the width of the blood vessel shadows in the circular OCT images.

7.4.2 TRBF and blood vessel size

Acute elevation of the IOP caused temporary shape changes of the ONH (Fig. 7.2A-C), as well as temporary constriction of the retinal blood vessels (Fig. 7.2D-F), observed in the volumetric and cross-sectional OCT images respectively. The red arrows in Figure 7.2 D-F show the change in blood vessels diameter with IOP elevation. Figure 7.3 shows statistical results for the TRBF and the BVS measured during the pre-loop, loop-on and post-loop phases in complete darkness (no visual stimulation). The TRBF decreased significantly from 5.6 ± 1.9 µL/min to 3.8 ± 1.2 µL/min during loop-wear ($p=0.02$) and recovered to 5.5 ± 1.2 µL/min after 10 minutes from loop removal ($p=0.02$ relative to loop-on). No significant difference between the pre-loop and the post-loop data was observed ($p=1.00$). On average (over all retinal arteries and veins and all animals), the elevated IOP had a significant effect on the retinal vessel size. The average retinal blood vessel diameter was 44.1 ± 4.5 µm at normal IOP (pre-loop), reduced significantly to 35.1 ± 2.6 µm (20.0 ± 4.7%, $p<0.01$) during the IOP elevation (loop-on), and recovered to 42.4 ± 3.3 µm within 10 min after loop removal ($p < 0.01$). There was no significant difference in the average blood vessels diameter between the pre-loop and post-loop measurements ($p=0.27$).

Elevation of the IOP also caused suppression of the visually evoked changes in the TRBF (Fig.7.4). At baseline (pre-loop), the TRBF showed 6.0 ± 3.3% increase in response to flicker stimulation. Elevation of the IOP to ~45 mmHg reduced significantly the magnitude of the visually evoked TRBF change to 0.1 ± 0.3% ($p < 0.01$). After loop removal, the flicker induced TRBF response recovered to 5.9 ± 1.7% ($p < 0.01$). No significant difference was detected in the visually evoked TRBF responses between baseline and recovery ($p=1.00$).

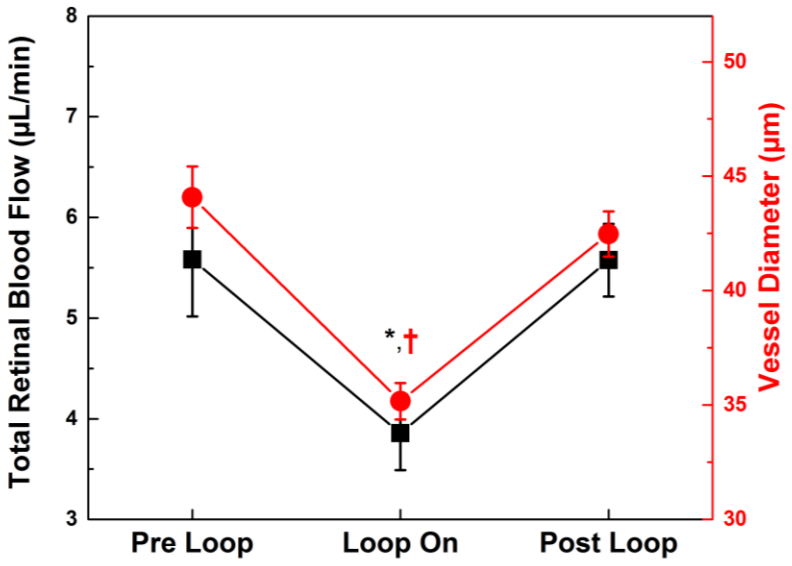

Figure 7.3 TRBF and retinal blood vessel diameter measured as functions of the IOP. *, † mark the significant differences of the "Loop on" data point compared to baseline and recovery data.

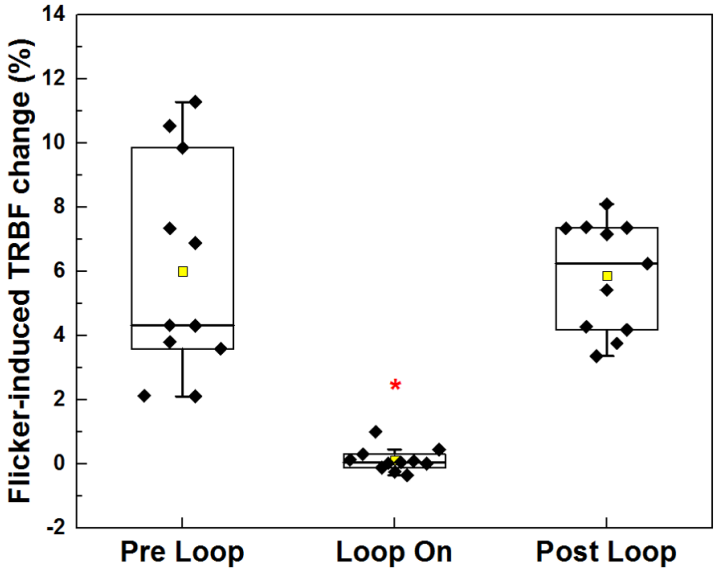

Figure 7.4 Statistics for the flicker-induced TRBF change in response to acute IOP elevation. Data is presented as box plot of 25 to 75 percentile with whisker marks outliers. Yellow squares mark the mean values, while "*" marks significant differences compared to the baseline and the recovery data.

7.4.3 Retinal function changes

Figure 7.5A shows a typical ERG trace acquired in our study, with its single-flash and flicker components marked with the red and green line boxes. Acute elevation of the IOP caused temporary increase in the a-wave and b-wave amplitudes and latencies of the ERG single flash component for the duration of the loop wear, and recovery of the ERG signal to normal after 10 min of the vascular loop removal (Fig. 7.5B). The magnitude of the ERG flicker component decreased during loop wear and returned to normal after loop removal (Fig. 7.5C). Synchronously, the flicker induced TRBF changes were suppressed during loop wear and recovered to normal within 10 min of loop removal (Fig. 7.5D).

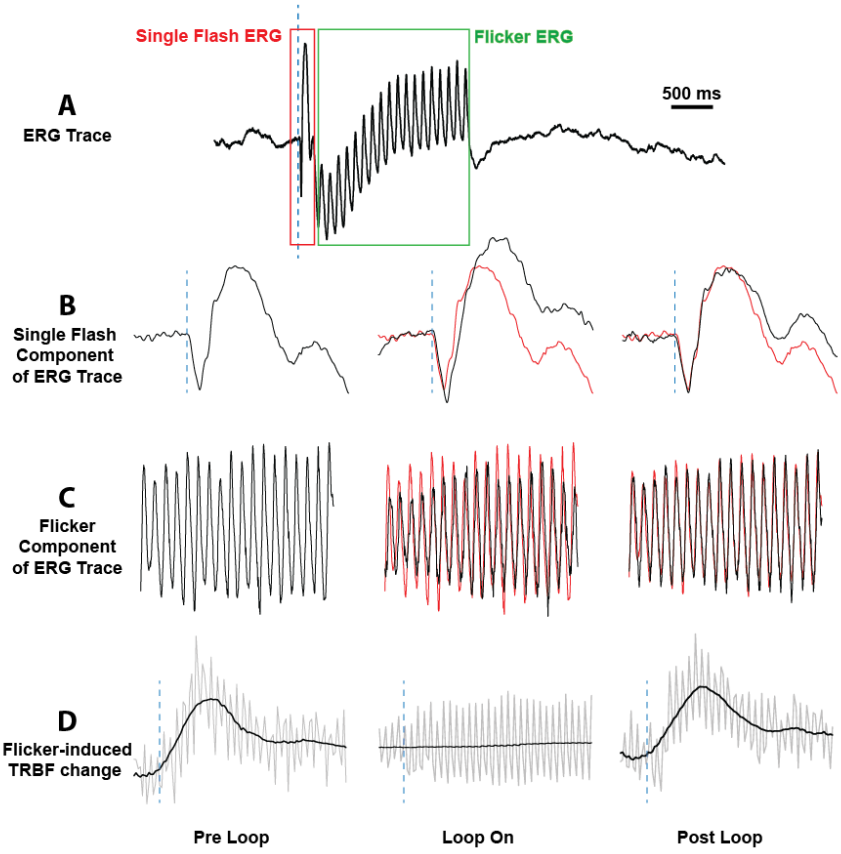

Figure 7.5(A) Representative ERG trace acquired with 2s flicker stimulus at normal IOP. Dashed line marks the stimulus onset. Red and green line boxes mark the single flash and flicker components of the ERG trace respectively. (B) Single flash component of the ERG trace evaluated before, during and the after the IOP elevation. (C) Flicker component of the ERG trace evaluated before, during and the after the IOP elevation. (D) Flicker induced TRBF changes evaluated before, during and the after the IOP elevation. Heartbeat induced oscillations in the TRBF are shown in grey, while the filtered TRBF is shown in black.

Increase of the single flash a-wave and b-wave magnitudes was observed during the IOP elevation (131.0 ± 21.3 µV and 166.5 ± 44.7 µV respectively), compared to the pre-loop value (a-wave 98.5 ± 22.9 µV, $p = 0.02$, b-wave 63.8 ± 29.1 µV, $p<0.01$) and at post loop value (a-wave 110.8 ± 21.2 µV, $p = 0.06$, b-wave 103.0 ± 17.5 µV, $p<0.01$) (Fig. 7.6A and 7.6B respectively). The FHC of the flicker ERG was not affected significantly by the loop wear ($p = 0.18$, Fig. 7.6C). However, the SHC decreased significantly from 26.7 ± 4.8 mV (pre-loop) to 12.4 ± 4.4 mV during loop wear

($p<0.01$), corresponding to a 55% reduction in amplitude, and recovered to 18.4 ± 2.8 mV after loop removal ($p<0.01$). The post-loop SHC value was significantly lower than the pre-loop measurement ($p <0.01$).

7.5 Discussion

The reduction of the flicker-induced TRBF change during acute IOP elevation observed in our study agreed well with findings from clinical studies conducted on high ocular tension glaucomatous patients[18]–[20], [22], [23]. Specifically, by using 15Hz green light flicker stimulation, Riva[18] found that the magnitude of the blood flow response to flicker stimulation at the neuroretinal rim of the optic disk reduced significantly in ocular hypertension and early glaucoma patients, Similarly, Gugleta[20], [22], [23] observed reduced flicker-induced vasodilation of retinal blood vessels in OAG patients (and ocular hypertension patients, for different ages and development stage of the glaucoma. Specifically, flicker-induced vasodilation in retinal veins was 0.8 ± 2.5% in early glaucoma patients, compared to 2.1 ± 2.1% in healthy subjects. In a different study, Garhöfer[264] used the ocular suction-cup method to elevate the IOP up to 43 mmHg for 60 seconds. ONH blood flow was measured by laser Doppler flowmetry and retinal vessel diameter was measured by a retinal vessel analyzer, and as a result, the response of retinal vessel diameter and ONH blood flow to the luminance flicker didn't change significantly, which contradicts the results from our study. One possible explanation is that 60s of IOP elevation to 43 mmHg may not be sufficient to induce measurable changes in the human TRBF.

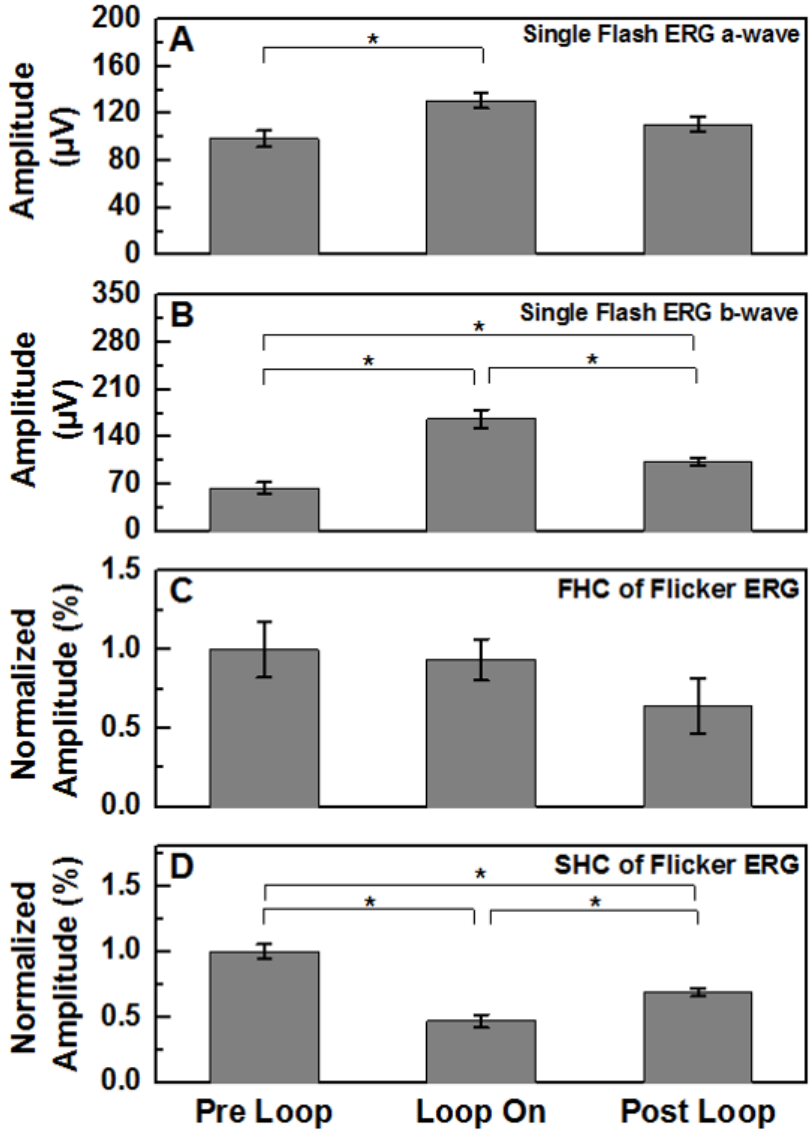

Figure 7.6 Metrics of the single flash component (a- and b-wave amplitudes) and flicker (FHC and SHC amplitude) components of the ERG traces as functions of the IOP. Data are presented as mean ± S.E. and any significant difference between the data in each column are marked with "*".

The effect of elevated IOP on the retinal blood perfusion and physiological response to visual stimulation is complex. Results from multiple studies suggest that the observed decrease in the TRBF and the vasoconstriction with elevated IOP could be associated with insufficient metabolic supply to the retina, caused by activated astrocyte[6], endothelial dysfunction[265] and excess of

nitric oxide (NO)[260], [266], though the exact physiological mechanism of these changes is unknown. The effect of elevated IOP on the functional response of the retina to visual stimulation has been studied extensively and more groups report decrease of the ERG's a-wave and b-wave amplitudes with elevated IOP[31], [53]. Our research group reported recently an initial pronounced increase of the ERG's a- and b-wave amplitudes in rats, during IOP elevation to a moderate level of 35 mmHg by use of a vascular loop[183]. Although such increase maybe counter intuitive, it was observed consistently both in the current study as well as in other studies conducted on rats of different strains[175]. Further increase of the IOP with a vascular loop to ischemic levels > 60 mmHg showed progressive decrease in the ERG's a-wave and b-wave amplitudes. Such supranormal scotopic a-wave and b-wave amplitudes with normal implicit times have been reported for specific conditions, including loss of retinal dopaminergic amacrine cells[139], [267], blockage of retinal dopamine receptors[141], [142], gestational low level lead exposure in rats[143] and humans[144], and loss of a mitochondrial ATP transporter in Ant1-/- mice[145]. Furthermore, Vielma et al.[151] showed that low level intravitreal injections of NO into rat eyes is associated with increases in the amplitudes of ERG a- and b-waves, OPs and pSTRs. Several groups have reported that chronic elevation of IOP to less than 35 mm Hg in the rat eye is associated with NO production in the retina[165], [166] and the optic nerve[166], [168].

The FHC and the SHC of flicker ERG could provide significant insight to the physiological mechanisms of reduced neurovascular coupling. It has been reported that in humans and monkeys, the FHC and SHC of the flicker ERG are affected mostly by the outer retina and inner retina, respectively[268]–[272]. Furthermore, strong correlation between flicker-induced retinal blood flow change and SHC was reported in both monkeys[273] and humans[241] though in those cases

the blood flow measurements and ERG recordings were acquired separately instead of synchronously. In this study, we observed synchronously a significant decrease in both the magnitude of the SHC of the flicker ERG and the flicker-induced TRBF change and during acute IOP elevation to a non-ischemic level of 45mmHg.Furthermore, the FHC of the flicker ERG remained unchanged during acute IOP elevation. As FHC is mostly affected by the outer retina, it is likely that the metabolic supply to the outer retina was not affected significantly by the IOP elevation. Most likely this is due to the fact that oxygen and nutrition to the outer retina are provided by the choroidal flow, which has been shown to resist changes in response to acute IOP elevation[58].

7.6 Conclusion

In this chapter, results from our study showed that acute IOP elevation to non-ischemic level of 45 mmHg causes significant decrease of both the flicker-induced TRBF change and the magnitude of the SHC of the ERG recordings. However, the ERG's a-wave and b-wave amplitudes showed several fold increase. Future studies in which the IOP is raised progressively from normal to ischemic levels and the respective changes in the retinal morphology, TRBF, BVS and ERG metrics are recorded simultaneously with the OCT+ERG system, may provide valuable information regarding the early stages of development of open-angle glaucoma. Such studies may prove more definitively that flicker-induced changes in the TRBF and the ERG metrics may be more sensitive markers to the early stages of glaucoma compared to markers based purely on morphological analysis such thickness changes in the NFL, GCL, IPL, or shape changes of the ONH.

Chapter 8 Method for accurate measurement of pulsatile retinal blood flow with Doppler optical coherence tomography

Notes and Acknowledgement

This chapter introduces a new scanning protocol and an automatic retinal blood vessel segmentation method to measure the pulsatile retinal blood flow. The robustness of this method was evaluated by repeated measurement in one rat, and statistics of pulsatile retinal blood flow metrics (mean blood flow, pulsatility index, and resistance index) were provided from 5 rats. This chapter is based on a journal manuscript:

Bingyao Tan, Zohreh Hosseinaee and K. Bizheva. "Dense concentric circle scanning protocol for measuring pulsatile retinal blood flow in rats with Doppler optical coherence tomography," *Journal of Biomedical Optics (accepted).*

Author contributions

Bingyao Tan and **Kostadinka Bizheva** conceived the study.

Kostadinka Bizheva provided the study material.

Bingyao Tan conducted the experiment and **Zohreh Hosseinaee** assisted with the animal handling and monitoring.

Bingyao Tan wrote the image analysis algorithms for the automatic blood vessel segmentation and the pulsatile blood flow quantification.

Bingyao Tan analyzed the data.

Kostadinka Bizheva contributed to the interpretation of all results.

Bingyao Tan wrote the first draft of the manuscript.

All authors contributed to the final version of the manuscript.

8.1 Introduction

Pulsatile retinal blood flow (BF) is associated with a number of ocular vascular related diseases, such as DR[274], central retinal venous occlusion[275], AMD[276] and glaucoma[258]. Recent studies indicated that metrics that characterize the pulsatility of retinal BF are sensitive to early pathophysiological changes in the retina, therefore accurate assessment of retinal BF pulsatility can aid the early diagnosis of potentially blinding diseases. Previously, different optical imaging modalities, such as scanning laser ophthalmology[277], laser Doppler velocimetry[92], and retinal vessel analyzer[278] have been used for assessment of the pulsatility of retinal BF. In comparison, DOCT offers higher sensitivity and provides simultaneously both structural and blood flow / blood perfusion information about the imaged object, which offers an opportunity to examine the relationship between morphological and BF changes in the retina induced by retinal diseases[261]. Since DOCT measures only axial BF along the imaging beam direction, precise knowledge of the angle between the incident beam and the blood vessel is necessary in order to assess absolute retinal blood flow. Dual beam DOCT[88], [279] utilizes two imaging beams incident on the same location in the imaged blood vessel in order to determine more precisely the absolute blood flow. However, this method requires more complex and expensive design of the OCT system, while precise alignment of the two imaging beams at the same location in the retina can be difficult and time consuming. An alternative approach to measuring absolute retinal BF with DOCT is to utilize a dual circle scanning pattern[92] and use the location displacement of blood vessels between the two circular OCT scans to calculate the Doppler angle. One limitation of this approach is that it is based on the assumption that the retinal blood vessel runs along a straight line between the two circular OCT scans, which is frequently not the case. A virtual concentric scan[90] method and an

OCT angiography based approach[280] have also been proposed for absolute blood flow assessment. Both of these methods utilize a raster-scanned volumetric OCT image stack of the retina and repeated circular OCT scans that are acquired separately, and later co-registered with the volumetric images in order to determine the Doppler angle of blood vessels. These approaches are very sensitive to eye motion artefacts and precise registration of retinal blood vessels between the circular scans and the volumetric image stacks can be problematic. *En-face* Doppler OCT[82], [83] offers a Doppler angle independent approach to calculation of the absolute retinal blood flow by integrating the axial blood flow from an *en-face* image. However, this approach requires ultrafast image acquisition or excellent synchronization of the OCT images with the cardiac cycle. Here we present a new scanning protocol that utilizes a dense concentric circular scan pattern over a doughnut-shaped area of the retina centered at the ONH, and an automatic retinal blood vessel segmentation algorithm, for more precise quantification of the absolute and pulsatile retinal BF. This new approach was tested in the rat retina and results were compared with the dual circle scan approach for absolute retinal blood flow measurement.

8.2 Methods

A research-grade, spectral domain OCT system, designed and built by our group for various imaging studies in the animal retina[177], [178], [243] was modified for use in this study. Briefly, a broad bandwidth SLD (λc = 1060 nm, $\Delta\lambda$ = 110 nm, Superlum Ltd, Ireland) was used to achieve 3.5 μm axial resolution in retinal tissue. The DOCT retinal imaging probe, comprised of 3 broadband NIR achromat doublet lenses (f1 = 10 mm, f2 = 60 mm, and f3 = 30 mm; Edmund Optics, Barrington, NJ, USA) and a pair of galvanometric scanners (Cambridge Technologies, Bedford, MA, USA), was designed to deliver a collimated imaging beam of 1.5 mm diameter and

1.7 mW optical power to the rat cornea, thus achieving ~5 μm lateral resolution in retinal tissue. A high resolution spectrometer (P&P Optica, Waterloo, Canada) and a NIR line scan camera (1024-LDH2 92 kHz, Sensors Unlimited, USA) were used at the detection end of the DOCT system.

Eleven-week old male Brown Norway rats (n = 10), weighting ~300 g were used in this study to test the new DOCT scanning protocol and automatic retinal blood vessel segmentation algorithm. All experiments described here were approved by the University of Waterloo Animal Research Ethics Committee and adhered to the ARVO Statement for Use of Animals in Ophthalmic and Vision Research. The rats were anesthetized with ketamine/xylazine (0.2 ml per 100 g body weight) delivered intraperitoneally, and a subcutaneous injection of 5 ml sterile saline was administered immediately after to keep the animal well hydrated during the imaging procedure. The rat's head was stabilized stereotactically and 1 drop of 0.5% tropicamide (pupillary dilator; Alcon) was applied to each eye. One drop of 0.5% proparacaine hydrochloride (topical anesthetic; Alcaine, Alcon) was applied to the imaged eye, and artificial tears were administered every 5 minutes to keep the cornea well hydrated and optically transparent.

A flow chart of proposed new approach to accurate evaluation of absolute and pulsatile BF is presented in Figure 8.1. A doughnut-shaped area of the rat retina, centered at the ONH was imaged using a dense concentric circular scan pattern (Fig. 8.1A). Two hundred concentric circular scans with diameters ranging from 0.8 mm to 1 mm were used to cover the imaged retinal area. Each concentric scan was comprised of 3000 A-scans, which offered overlap between adjacent A-scans of 78% -84%, dependent on the diameter of the circular scan. The camera acquisition rate was set to 47 kHz resulting in frame rate of 15.7 fps and total acquisition time of 12.7 seconds. To calculate

the absolute BF for each retinal blood vessel, the information from each complex OCT image was divided into two parts: the amplitude was used to segment the retinal blood vessels (Fig. 8.1B-D), while the phase was used to calculate the axial blood flow (Fig. 8.1E). A three-step method was used to segment the retinal blood vessels. First, the retinal surface was segmented automatically in each circular DOCT scan (Fig. 8.1B). Second, a shadow diagram was generated for each circular DOCT scan by averaging the intensity of the OCT image between the two cyan lines and the retinal pigmented epithelium. Then, an *en-face* shadow image was composed by combining all 200 axial OCT shadow diagrams. The dark areas in the *en-face* shadow image (Fig. 8.1C) correspond to the retinal blood vessels. Third, an algorithm based on modified graph theory and a dynamic programming[281] was developed and used to segment automatically the retinal blood vessels from the *en-face* shadow image. The two boundaries for each blood vessel were segmented pairwisely and different blood vessels were segmented in sequence. Note that for branching blood vessels, only one branch was segmented by the automatic algorithm, while the second branch

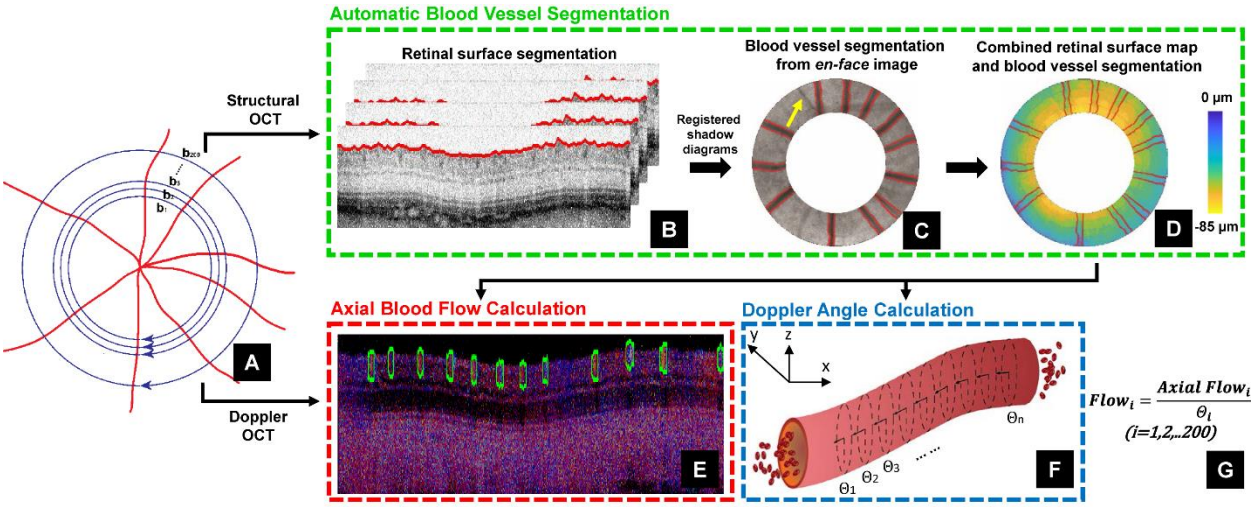

Figure 8.1 Flow chart for the absolute retinal BF assessment. (A) Diagram of concentric scans with variable diameter, centered at the ONH. (B-D) Automatic blood vessel segmentation protocol: (B) Retinal surface segmentation for each concentric scan (red

line). The area between the two cyan dashed lines is averaged axially to generate a shadow image (C) in which blood vessel are segmented and marked with red lines. The yellow arrow marks a branched blood vessel that is not segmented by the automatic algorithm. (D) A retinal surface elevation map where all segmented blood vessels are marked. (E) A representative DOCT cross-sectional image labelled with segmented blood vessels. (F) Diagram for precise Doppler angle calculation of the spatially dependent magnitude and direction of the retinal BF. (G) Formula for calculating the absolute BF from the i*th* circular scan.

was ignored (yellow arrow in Fig. 8.1C). Once the vessels' segmentation was complete, a retinal surface elevation map was generated with all the segmented blood vessels labelled on it (Fig. 8.1D). The axial and lateral displacements of each blood vessel along radial direction were determined from the surface elevation map and the Doppler angle was calculated using the formula:

$$\Theta = \arccos\left(\frac{\Delta z}{\sqrt{\Delta x^2 + \Delta y^2 + \Delta z^2}}\right)$$

Here, Δy and Δz are the lateral and axial displacements of the blood vessel between adjacent circular scans respectively, and Δx is the distance between adjacent circular scans (0.5 μm). The absolute retinal blood flow for the ith concentric circular DOCT scan was calculated by the dividing the axial BF by the corresponding Doppler angle (formula in Fig. 8.1G). In this study, Doppler angles larger than 85° were excluded from the data analysis, as the imprecision of calculating the absolute retinal BF is strongly dependent on $1/\cos(\Theta)$[92].

8.3 Results and Discussion

Representative time traces of the retinal BF measured from 3 arteries and 3 veins in one rat are shown in Figure 8.2A. These traces were selected to show the minimum, maximum and mean BF pulsatility magnitude for all the retinal vessels of that animal. A 1.5 s time window shows 5 complete cardiac cycles and an average arteriovenous delay of 160 ms that was determined by

applying a cross correlation method[282] to the sum of the arterial and venous flow. Quantitative metrics of the pulsatile BF, such as the mean BF, the pulsatility index (PI), and the resistance index (RI), were used to analyze the pulsatile BF. For each retinal blood vessel, the mean BF was calculated by averaging the blood flow within the time window, while the PI and RI were calculated using the definition formulas shown in Fig 8.2A. To test the reproducibility of the pulsatile blood flow data, the same scanning protocol was repeated (n = 6) in the same animal with 3-minute time interval between consecutive measurements. Statistical data for the BF, PI and RI are shown in Figure 8.2B-D, where arteries are marked in red color and veins in blue color. Although the absolute magnitudes for the arterial and venous BF were very similar and ranged from ~ 0.7 μL/min to ~0.9 μL/min, the arterial PI and RI values were higher than the ones determined for retinal veins.

The same scanning protocol was applied to 9 additional animals and the statistical results are presented in Fig. 8.3A. The average total retinal BF was 6.2 ± 0.8 μL/min in arteries and 5.6 ± 0.8 μL/min in veins. The difference between the arterial and venous total BF is most likely due to failure of the automatic segmentation algorithm to recognize and account retinal veins, as the veins in the shadow images were not distinctive enough to be segmented properly. For example, in all 10 animals, the segmentation algorithm successfully identified and segmented a total of 66 arteries and 56 veins. Fig. 8.3B shows a histogram of the absolute BF measured from all segmented blood vessels. Arterial flow showed a slightly broader distribution compared to venous flow; however, the centroids for arterial venous BF histograms were almost identical. Furthermore, the mean absolute BF per vessel was very similar: 0.93 μL/min in arteries vs 0.98 μL/min in veins. Fig. 8.3C and 8.3D show histograms for the PI and RI respectively, determined from all segmented blood

vessels. The PI for 22% of the retinal arteries was higher that the PI measured in any of the retinal veins. Similarly, the RI for 28% of the retinal arteries was higher that the RI measured in any of the retinal veins.

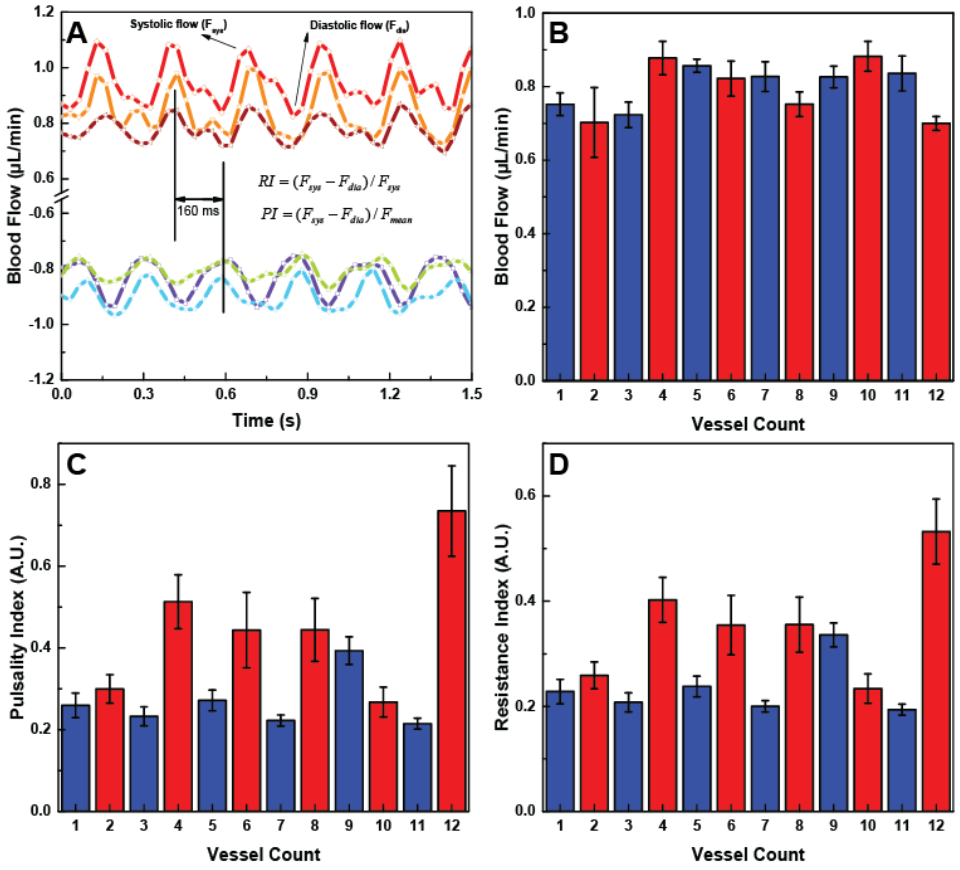

Figure 8.2 (A) Representative pulsatile BF recordings acquired from 3 arteries and 3 veins of one rat. The averaged arterio-venous delay was measured to be 160 ms. (B-D). The mean retinal BF, PI and RI calculated from twelve segmented retinal blood vessels in one rat (red- arteries; blue – veins). Data is presented as Mean ± SE.

To evaluate the performance of the proposed new method for accurate assessment of pulsatile blood flow, results from the dense concentric circle protocol were compared with results from the dual concentric circle protocol[92] using the same raw data. For the dual circle protocol, the innermost and outermost of the 200 concentric scans were used to calculate the Doppler angle,

while the 8 central circular scans that covered 1 full cardiac cycle were used to calculate the mean axial blood flow. Results showed 3.8° ± 2.1° difference in the Doppler angle assessment between the dense concentric circle and the dual concentric circle protocols, which resulted in ~8% difference in the assessment of the absolute blood flow. Considering the fact that the dual concentric circle scanning protocol does not account for changes in the spatial orientation of blood vessels with respect to the incident direction of the OCT imaging beam, it is natural to conclude that the dense concentric circle scanning protocol allows for more accurate assessment of the Doppler angle and consequently, the absolute retinal blood flow.

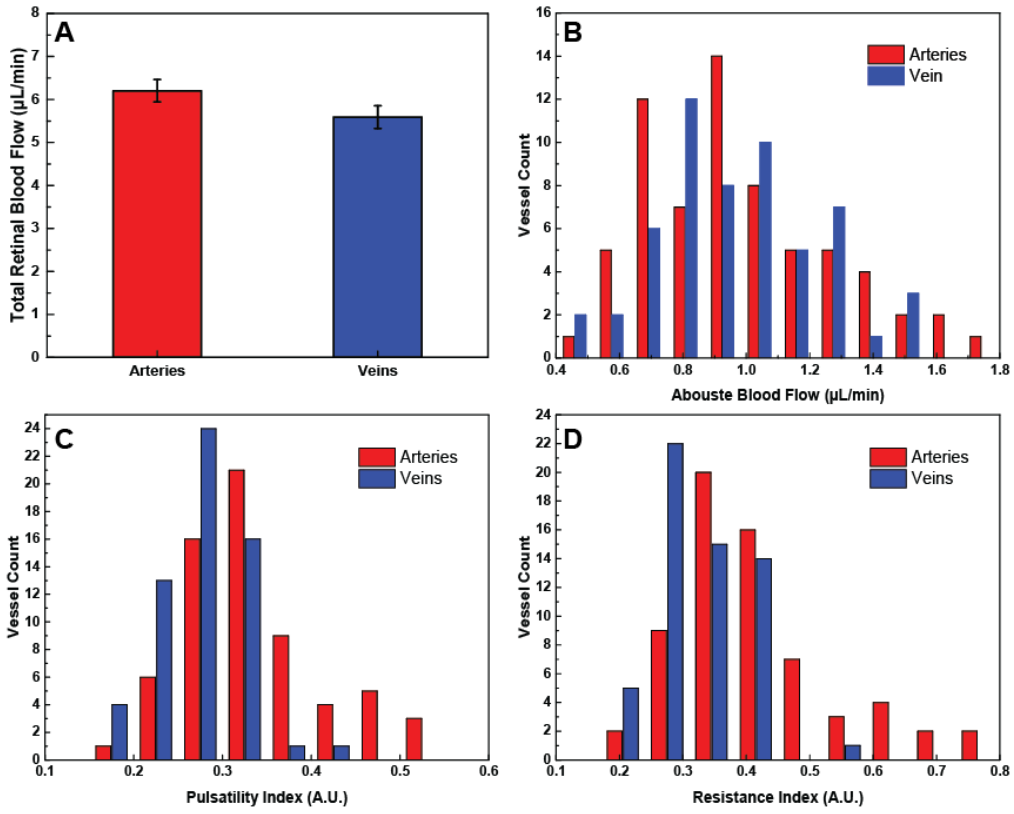

Figure 8.3 (A) Statistical results for the total RBF measured from all animals in the study (n=5). (B-D) Histograms show the number of retinal vessels as functions of the mean RBF, PI and RI.

8.4 Conclusion

In this chapter, a new dense concentric circle scanning protocol was developed using a camera with a relatively slow image acquisition rate (47 kHz) to measure accurately the pulsatile blood flow in retinal arteries and veins of the rat retina with spectral domain OCT. This method offers simplicity of the OCT system design, scanning protocol and data analysis, as well as better accuracy in the measurement of the Doppler angle and the assessment of the pulsatile retinal blood flow. Although this method was tested in the animal retina, it can be easily adapted to imaging and assessment of retinal blood flow in the human eye by using the full speed of the camera (92 kHz) and reducing the number of concentric scans. Because of its simplicity and accuracy, this method can find applications in both clinical studies and fundamental animal research of potentially blinding retinal diseases.

Chapter 9 Conclusion

This thesis dissertation examined changes in the retinal morphology, blood flow and physiology associated with elevated IOP in a rat model of glaucoma. Results from these studies extend our knowledge of elevated IOP-induced alterations in the eye and provide insight to better our understanding of glaucoma.

9.1 Summary of contributions

The main contributions of this PhD dissertation are:

- Results from our acute/chronic intermittent IOP elevation studies suggest that: 1) acute moderate IOP elevation is associated with temporal increase of retinal electrophysiological response to visual stimulation; 2) Monotonic decrease of retinal blood flow/perfusion and nonlinear response of retinal electrophysiology are observed for IOP elevation from non-ischemic level to ischemic level; 3) Chronic, intermittent IOP elevations to 35 mmHg for 1h/day on 6 days/ week over a period of 2 months did not cause permanent retinal functional and ONH morphological changes. However, significantly reduced retinal function and larger ONH depression depth were observed temporarily in response to acute IOP elevation, which indicates that a moderate stress test can serve as a sensitive marker for identifying early signs of glaucomatous damage. The novel OCT+ERG system, designed for simultaneous imaging of the retinal morphology, function and blood flow/perfusion, is a valuable research tool that provides the advantages of shortening the total data acquisition time and allowing for direct correlation of retinal function, retinal blood flow/perfusion and retinal morphology. Moreover, the OCT+ERG system used for

this PhD research can be adapted easily for clinical studies of glaucoma with minimal modifications, such as changing the optical design of the imaging/stimulation probe to adapt it to the human eye, use of ERG electrodes designed for human subjects and using the maximum data acquisition rate of the OCT camera in order to enable imaging of faster retinal blood flow that is typical for the human eye. Using the full speed of the camera (92 kHz) will also suppress the phase wrapping, as well as reduce the motion artifacts associated with involuntary eye motion.

- In this thesis research, the new OCT+ERG system was used to assess the neurovascular coupling in the rat retina under normal and moderately elevated IOP, and results from our studies showed that acute IOP elevation to 43 mmHg caused the reduction of the magnitude of the flicker evoked retinal blood flow change. This OCT+ERG system along with the image acquisition protocol and image processing algorithms can be adapted easily for clinical studies of glaucoma by redesigning the OCT+ERG imaging probe to adapt it to human eye. Furthermore, the same system and imaging protocols can be used for human and animal studies of different vascular diseases of the retina, such as DR and AMD.
- The development of a novel method based on a dense circular scanning protocol can achieve more accurate measurement of pulsatile retinal blood flow. This scanning protocol can be adapted directly for clinical studies with some modification such as: 1) utilize the full speed of the camera (92 kHz) in order to reduce eye motion artifacts and enable assessment of faster blood flow; 2) reduce the number of circular concentric scans to 40, which should reduce the risk of repeated exposure of retinal tissue to laser radiation, while still providing accurate assessment of the pulsatile total retinal blood flow.

9.2 Future Research

The OCT+ERG technology and the animal studies discussed in this PhD thesis leave plenty of room for future technological development, as well as pose questions that can before the center point of future animal and human studies. For example:

- The current OCT+ERG technology was developed specifically for simultaneous assessment of the retinal structure, function and blood flow/perfusion in the rat retina. This technology can easily be adapted for clinical studies on humans or in transgenic mice, to be able to investigate other retinal neurodegenerative diseases such as AMD, DR, Alzheimer's, etc. The adaptation of the technology is straightforward, as it requires only a redesign of the combined imaging probe to adapt it to the human or mice retina. Some revision to the MATLAB codes used for processing and analysis of the retinal data will be necessary to adapt them to the human and mice retinal images.
- The neurovascular coupling experiments described in Ch. 6 and 7 were conducted with a limited number of parameters for the visual stimulus. Future experiments can focus on different colors, durations, intensities and patterns of the visual stimuli in order to uncover functional links between certain types of retinal neurons. Furthermore, the study in Ch. 7 was conducted for only one level of IOP elevation. Future studies will focus on step-wise increase of the IOP and especially in the range of 10 mm – to 30 mmHg, in order to gain a better understanding of the origins of the supra-normal ERG a-wave and b-wave amplitudes that were observed under elevated IOP with the vascular loop.

References

[1] Y. C. Tham, X. Li, T. Y. Wong, H. A. Quigley, T. Aung, and C. Y. Cheng, "Global prevalence of glaucoma and projections of glaucoma burden through 2040: A systematic review and meta-analysis," *Ophthalmology*, vol. 121, no. 11, pp. 2081–2090, Nov. 2014.

[2] A. C. Day *et al.*, "The prevalence of primary angle closure glaucoma in European derived populations: a systematic review," *Br. J. Ophthalmol.*, vol. 96, no. 9, pp. 1162–1167, 2012.

[3] P. N. Schacknow and J. R. Samples, *The glaucoma book: A practical, evidence-based approach to patient care*. 2010.

[4] Y. H. Kwon, J. H. Fingert, M. H. Kuehn, and W. L. M. Alward, "Primary Open-Angle Glaucoma," *N. Engl. J. Med.*, vol. 360, no. 11, pp. 1113–1124, 2009.

[5] L. Ventura and V. Porciatti, "Restoration of retinal ganglion cell function in early glaucoma after intraocular pressure reduction: a pilot study," *Ophthalmology*, vol. 112, no. 1, pp. 20–27, 2005.

[6] A. P. Cherecheanu, G. Garhofer, D. Schmidl, R. Werkmeister, and L. Schmetterer, "Ocular perfusion pressure and ocular blood flow in glaucoma," *Curr. Opin. Pharmacol.*, vol. 13, no. 1, pp. 36–42, 2013.

[7] S. Wentz *et al.*, "18 . The role of blood flow in glaucoma," pp. 243–260, 2018.

[8] S. T. Venkataraman, J. G. Flanagan, and C. Hudson, "Vascular reactivity of optic nerve head and retinal blood vessels in glaucoma--a review.," *Microcirculation*, vol. 17, no. 7, pp. 568–81, 2010.

[9] A. J. Bellezza, C. J. Rintalan, H. W. Thompson, J. C. Downs, R. T. Hart, and C. F. Burgoyne, "Deformation of the lamina cribrosa and anterior scleral canal wall in early experimental glaucoma," *Investig. Ophthalmol. Vis. Sci.*, vol. 44, no. 2, pp. 623–637, 2003.

[10] K. M. Ivers *et al.*, "In vivo detection of laminar and peripapillary scleral hypercompliance

in early monkey experimental glaucoma," *Investig. Ophthalmol. Vis. Sci.*, vol. 57, no. 9, p. OCT388-OCT403, 2016.

[11] J. C. Downs, "Optic nerve head biomechanics in aging and disease," *Exp. Eye Res.*, vol. 133, pp. 19–29, 2015.

[12] R. Grytz *et al.*, "Material properties of the posterior human sclera," *J. Mech. Behav. Biomed. Mater.*, vol. 29, pp. 602–617, 2014.

[13] C. F. Burgoyne, J. Crawford Downs, A. J. Bellezza, J. K. Francis Suh, and R. T. Hart, "The optic nerve head as a biomechanical structure: A new paradigm for understanding the role of IOP-related stress and strain in the pathophysiology of glaucomatous optic nerve head damage," *Prog. Retin. Eye Res.*, vol. 24, no. 1, pp. 39–73, 2005.

[14] J. C. Downs, M. D. Roberts, and C. F. Burgoyne, "Biomechanics of the Optic Nerve Head *," *J. Glaucoma*, vol. 1, no. 2009, pp. 183–201, 2010.

[15] K. M. Ivers *et al.*, "In Vivo Changes in Lamina Cribrosa Microarchitecture and Optic Nerve Head Structure in Early Experimental Glaucoma," *PLoS One*, vol. 10, no. 7, p. e0134223, 2015.

[16] L. Wang, G. Cull, C. F. Burgoyne, S. Thompson, and B. Fortune, "Longitudinal alterations in the dynamic autoregulation of optic nerve head blood flow revealed in experimental glaucoma.," *Investig. Ophthalmol. Vis. Sci.*, vol. 55, no. 6, pp. 3509–16, 2014.

[17] J. E. Grunwald, C. E. Riva, R. A. Stone, E. U. Keates, and B. L. Petrig, "Retinal Autoregulation in Open-angle Glaucoma," *Ophthalmology*, vol. 91, no. 12, pp. 1690–1694, Dec. 1984.

[18] C. E. Riva, T. Salgarello, E. Logean, A. Colotto, E. M. Galan, and B. Falsini, "Flicker-evoked response measured at the optic disc rim is reduced in ocular hypertension and early glaucoma," *Investig. Ophthalmol. Vis. Sci.*, vol. 45, no. 10, pp. 3662–3668, 2004.

[19] G. Garhöfer, C. Zawinka, H. Resch, K. H. Huemer, L. Schmetterer, and G. T. Dorner, "Response of retinal vessel diameters to flicker stimulation in patients with early open

angle glaucoma.," *J. Glaucoma*, vol. 13, no. 4, pp. 340–4, Aug. 2004.

[20] K. Gugleta, C. Türksever, A. Polunina, and S. Orgül, "Effect of ageing on the retinal vascular responsiveness to flicker light in glaucoma patients and in ocular hypertension.," *Br. J. Ophthalmol.*, vol. 97, no. 7, pp. 848–51, 2013.

[21] K. Gugleta, G. Fuchsjäger-Mayrl, and S. Orgül, "Is Neurovascular Coupling of Relevance in Glaucoma?," *Surv. Ophthalmol.*, vol. 52, no. 6 SUPPL., pp. 139–143, 2007.

[22] K. Gugleta *et al.*, "Dynamics of retinal vessel response to flicker light in glaucoma patients and ocular hypertensives," *Graefe's Arch. Clin. Exp. Ophthalmol.*, vol. 250, no. 4, pp. 589–594, 2012.

[23] K. Gugleta *et al.*, "Retinal neurovascular coupling in patients with glaucoma and ocular hypertension and its association with the level of glaucomatous damage," *Graefe's Arch. Clin. Exp. Ophthalmol.*, vol. 251, no. 6, pp. 1577–1585, 2013.

[24] J. G. Feghali, J. C. Jin, and J. V. Odom, "Effect of short-term intraocular pressure elevation on the rabbit electroretinogram," *Investig. Ophthalmol. Vis. Sci.*, vol. 32, no. 8, pp. 2184–2189, 1991.

[25] Q. Yang, J. Shen, W. Guo, J. Wen, Z. Wang, and D. Yu, "Effect of acute intraocular pressure elevation on blood flow velocity and resistance in the rabbit ophthalmic artery.," *Vet. Ophthalmol.*, vol. 14, no. 6, pp. 353–7, 2011.

[26] L. Wang and a Bill, "Effects of constant and flickering light on retinal metabolism in rabbits," *Acta Ophthalmol Scand*, vol. 75, no. 3, pp. 227–231, 1997.

[27] C. J. Abbott, T. E. Choe, C. F. Burgoyne, G. Cull, L. Wang, and B. Fortune, "Comparison of retinal nerve fiber layer thickness in vivo and axonal transport after chronic intraocular pressure elevation in young versus older rats," *PLoS One*, vol. 9, no. 12, pp. 1–24, 2014.

[28] B. C. Chauhan, J. Pan, M. L. Archibald, T. L. LeVatte, M. E. M. Kelly, and F. Tremblay, "Effect of intraocular pressure on optic disc topography, electroretinography, and axonal loss in a chronic pressure-induced rat model of optic nerve damage," *Investig. Ophthalmol. Vis. Sci.*, vol. 43, no. 9, pp. 2969–2976, 2002.

[29] S. Sandalon *et al.*, “Functional and structural evaluation of lamotrigine treatment in rat models of acute and chronic ocular hypertension,” *Exp. Eye Res.*, vol. 115, pp. 47–56, 2013.

[30] K. M. Joos, C. Li, and R. M. Sappington, “Morphometric changes in the rat optic nerve following short-term intermittent elevations in intraocular pressure,” *Investig. Ophthalmol. Vis. Sci.*, vol. 51, no. 12, pp. 6431–6440, Dec. 2010.

[31] B. Fortune *et al.*, “Selective ganglion cell functional loss in rats with experimental glaucoma,” *Investig. Ophthalmol. Vis. Sci.*, vol. 45, no. 6, pp. 1854–1862, 2004.

[32] E. Woldemussie, G. Ruiz, M. Wijono, and L. a Wheeler, “Neuroprotection of Retinal Ganglion Cells by Brimonidine in Rats with Laser-Induced Chronic Ocular Hypertension,” pp. 2849–2855, 2015.

[33] A. Sawada and A. H. Neufeld, “Confirmation of the rat model of chronic, moderately elevated intraocular pressure,” *Exp Eye Res*, vol. 69, no. 5, pp. 525–531, 1999.

[34] H. H. Liu, B. V. Bui, C. T. O. Nguyen, J. M. Kezic, A. J. Vingrys, and Z. He, “Chronic ocular hypertension induced by circumlimbal suture in rats,” *Investig. Ophthalmol. Vis. Sci.*, vol. 56, no. 5, pp. 2811–2820, 2015.

[35] Z. He, A. J. Vingrys, J. A. Armitage, C. T. Nguyen, and B. V. Bui, “Chronic hypertension increases susceptibility to acute IOP challenge in rats,” *Investig. Ophthalmol. Vis. Sci.*, vol. 55, no. 12, pp. 7888–7895, 2014.

[36] B. Fortune *et al.*, “Selective ganglion cell functional loss in rats with experimental glaucoma,” *Investig. Ophthalmol. Vis. Sci.*, vol. 45, no. 6, pp. 1854–1862, Jun. 2004.

[37] B. V. Bui, Z. He, A. J. Vingrys, C. T. O. Nguyen, V. H. Y. Wong, and B. Fortune, “Using the electroretinogram to understand how intraocular pressure elevation affects the rat retina,” *J. Ophthalmol.*, vol. 2013, 2013.

[38] J. C. MORRISON, C. G. MOORE, L. M. H. DEPPMEIER, B. G. GOLD, C. K. MESHUL, and E. C. JOHNSON, “A Rat Model of Chronic Pressure-induced Optic Nerve Damage,” *Exp. Eye Res.*, vol. 64, no. 1, pp. 85–96, 1997.

[39] S. D. Grozdanic, Y. H. Kwon, D. S. Sakaguchi, R. H. Kardon, and I. M. Sonea, "Functional evaluation of retina and optic nerve in the rat model of chronic ocular hypertension," *Exp. Eye Res.*, vol. 79, no. 1, pp. 75–83, 2004.

[40] D. E. Brooks, "Glaucoma in the dog and cat.," *Vet. Clin. North Am. Small Anim. Pract.*, vol. 20, no. 3, pp. 775–97, May 1990.

[41] J. Ruiz-Ederra *et al.*, "The pig eye as a novel model of glaucoma," *Exp. Eye Res.*, vol. 81, no. 5, pp. 561–569, Nov. 2005.

[42] C. McMahon, E. V. Semina, and B. A. Link, "Using zebrafish to study the complex genetics of glaucoma," *Comp. Biochem. Physiol. Part C Toxicol. Pharmacol.*, vol. 138, no. 3, pp. 343–350, Jul. 2004.

[43] S. S. Hayreh, J. B. Jonas, and M. B. Zimmerman, "Parapapillary chorioretinal atrophy in chronic high-pressure experimental glaucoma in rhesus monkeys," *Investig. Ophthalmol. Vis. Sci.*, vol. 39, no. 12, pp. 2296–2303, 1998.

[44] H. Yang, H. Thompson, M. D. Roberts, I. A. Sigal, J. C. Downs, and C. F. Burgoyne, "Deformation of the early glaucomatous monkey optic nerve head connective tissue after acute IOP elevation in 3-D histomorphometric reconstructions," *Investig. Ophthalmol. Vis. Sci.*, vol. 52, no. 1, pp. 345–363, 2011.

[45] M. J. A. Girard, J. K. Francis Suh, M. Bottlang, C. F. Burgoyne, and J. Crawford Downs, "Biomechanical changes in the sclera of monkey eyes exposed to chronic IOP elevations," *Investig. Ophthalmol. Vis. Sci.*, vol. 52, no. 8, pp. 5656–5669, 2011.

[46] N. G. Strouthidis, B. Fortune, H. Yang, I. A. Sigal, and C. F. Burgoyne, "Effect of acute intraocular pressure elevation on the monkey optic nerve head as detected by spectral domain optical coherence tomography.," *Investig. Ophthalmol. Vis. Sci.*, vol. 52, no. 13, pp. 9431–7, Jan. 2011.

[47] J. B. Jonas and S. S. Hayreh, "Localised retinal nerve fibre layer defects in chronic experimental high pressure glaucoma in rhesus monkeys.," *Br. J. Ophthalmol.*, vol. 83, no. 11, pp. 1291–5, 1999.

[48] R. A. Bouhenni, J. Dunmire, A. Sewell, and D. P. Edward, “Animal models of glaucoma,” *J. Biomed. Biotechnol.*, vol. 2012, 2012.

[49] E. van der Zypen, “Experimental Morphological Study on Structure and Function of the Filtration Angle of the Rat Eye,” *Ophthalmologica*, vol. 174, no. 5, pp. 285–298, 1977.

[50] C. Remé, U. Urner, and B. Aeberhard, “The development of the chamber angle in the rat eye. Morphological characteristics of developmental stages.,” *Graefes Arch. Clin. Exp. Ophthalmol.*, vol. 220, no. 3, pp. 139–53, 1983.

[51] C. L. Schlamp, Y. Li, J. a Dietz, K. T. Janssen, and R. W. Nickells, “Progressive ganglion cell loss and optic nerve degeneration in DBA/2J mice is variable and asymmetric.,” *BMC Neurosci.*, vol. 7, p. 66, 2006.

[52] F. Schuettauf, K. Quinto, R. Naskar, and D. Zurakowski, “Effects of anti-glaucoma medications on gangion cell survival: The DBA/2J mouse model,” *Vision Res.*, vol. 42, no. 20, pp. 2333–2337, 2002.

[53] T. I. Tsai, B. V. Bui, and A. J. Vingrys, “Effect of acute intraocular pressure challenge on rat retinal and cortical function,” *Investig. Ophthalmol. Vis. Sci.*, vol. 55, no. 2, pp. 1067–1077, 2014.

[54] Y. X. Kong, J. G. Crowston, a J. Vingrys, I. a Trounce, and V. B. Bui, “Functional changes in the retina during and after acute intraocular pressure elevation in mice,” *Investig. Ophthalmol. Vis. Sci*, vol. 50, no. 12, pp. 5732–5740, 2009.

[55] Z. He, B. V Bui, and A. J. Vingrys, “The rate of functional recovery from acute IOP elevation.,” *Investig. Ophthalmol. Vis. Sci.*, vol. 47, no. 11, pp. 4872–80, 2006.

[56] J. G. Crowston *et al.*, “An acute intraocular pressure challenge to assess retinal ganglion cell injury and recovery in the mouse,” *Exp. Eye Res.*, vol. 141, pp. 3–8, 2014.

[57] Z. Zhi, W. Cepurna, E. Johnson, H. Jayaram, J. Morrison, and R. K. Wang, “Evaluation of the effect of elevated intraocular pressure and reduced ocular perfusion pressure on retinal capillary bed filling and total retinal blood flow in rats by OMAG/OCT,” *Microvasc. Res.*, vol. 101, pp. 86–95, 2015.

[58] Z. Zhi, W. O. Cepurna, E. C. Johnson, J. C. Morrison, and R. K. Wang, “Impact of intraocular pressure on changes of blood flow in the retina, choroid, and optic nerve head in rats investigated by optical microangiography,” *Biomed. Opt. Express*, vol. 3, no. 9, p. 2220, 2012.

[59] Z. Zhi, W. Cepurna, E. Johnson, T. Shen, J. Morrison, and R. K. Wang, “Volumetric and quantitative imaging of retinal blood flow in rats with optical microangiography.,” *Biomed. Opt. Express*, vol. 2, no. 3, pp. 579–91, 2011.

[60] B. Fortune *et al.*, “Deformation of the Rodent Optic Nerve Head and Peripapillary Structures during Acute Intraocular Pressure Elevation,” *Investig. Opthalmol. Vis. Sci.*, vol. 52, no. 9, p. 6651, 2011.

[61] J. M. Kezic, V. Chrysostomou, I. A. Trounce, P. G. McMenamin, and J. G. Crowston, “Effect of anterior chamber cannulation and acute IOP elevation on retinal macrophages in the adult mouse,” *Investig. Ophthalmol. Vis. Sci.*, vol. 54, no. 4, pp. 3028–3036, 2013.

[62] H. Levkovitch-Verbin, H. A. Quigley, K. R. G. Martin, D. Valenta, L. A. Baumrind, and M. E. Pease, “Translimbal laser photocoagulation to the trabecular meshwork as a model of glaucoma in rats,” *Investig. Ophthalmol. Vis. Sci.*, vol. 43, no. 2, pp. 402–410, 2002.

[63] M. Salinas-Navarro *et al.*, “Functional and morphological effects of laser-induced ocular hypertension in retinas of adult albino Swiss mice.,” *Mol. Vis.*, vol. 15, no. December, pp. 2578–98, 2009.

[64] H. Chen *et al.*, “Optic neuropathy due to microbead-induced elevated intraocular pressure in the mouse,” *Investig. Ophthalmol. Vis. Sci.*, vol. 52, no. 1, pp. 36–44, 2011.

[65] H. Chen *et al.*, “Progressive degeneration of retinal and superior collicular functions in mice with sustained ocular hypertension,” *Investig. Ophthalmol. Vis. Sci.*, vol. 56, no. 3, pp. 1971–1984, 2015.

[66] L. Jia, W. O. Cepurna, E. C. Johnson, and J. C. Morrison, “Patterns of intraocular pressure elevation after aqueous humor outflow obstruction in rats,” *Investig. Ophthalmol. Vis. Sci.*, vol. 41, no. 6, pp. 1380–1385, 2000.

[67] V. Prokosch, M. Schallenberg, and S. Thanos, “Crystallins Are Regulated Biomarkers for Monitoring Topical Therapy of Glaucomatous Optic Neuropathy,” *PLoS One*, vol. 8, no. 2, 2013.

[68] M. Roh *et al.*, “Etanercept, a widely used inhibitor of tumor necrosis factor-α (TNF- α), prevents retinal ganglion cell loss in a rat model of glaucoma,” *PLoS One*, vol. 7, no. 7, pp. 1–13, 2012.

[69] M. Vidal-Sanz *et al.*, “Understanding glaucomatous damage: Anatomical and functional data from ocular hypertensive rodent retinas,” *Prog. Retin. Eye Res.*, vol. 31, no. 1, pp. 1–27, 2012.

[70] S. Yu, T. Tanabe, and N. Yoshimura, “A rat model of glaucoma induced by episcleral vein ligation,” *Exp. Eye Res.*, vol. 83, no. 4, pp. 758–770, Oct. 2006.

[71] J. Danias *et al.*, “Characterization of retinal damage in the episcleral vein cauterization rat glaucoma model,” *Exp. Eye Res.*, vol. 82, no. 2, pp. 219–228, Feb. 2006.

[72] H.-H. Liu and J. G. Flanagan, “A Mouse Model of Chronic Ocular Hypertension Induced by Circumlimbal Suture,” *Investig. Opthalmol. Vis. Sci.*, vol. 58, no. 1, p. 353, 2017.

[73] D. Zhao *et al.*, “Characterization of the circumlimbal suture model of chronic IOP elevation in mice and assessment of changes in gene expression of stretch sensitive channels,” *Front. Neurosci.*, vol. 11, no. FEB, pp. 1–15, 2017.

[74] J. H. K. Liu, X. Zhang, D. F. Kripke, and R. N. Weinreb, “Twenty-four-hour intraocular pressure pattern associated with early glaucomatous changes,” *Investig. Ophthalmol. Vis. Sci.*, vol. 44, no. 4, pp. 1586–1590, 2003.

[75] E. Hughes, P. Spry, and J. Diamond, “24-Hour Monitoring of Intraocular Pressure in Glaucoma Management: a Retrospective Review.,” *J. Glaucoma*, vol. 12, no. 3, pp. 232–6, 2003.

[76] O. W. Gramlich *et al.*, “Dynamics, alterations, and consequences of minimally invasive intraocular pressure elevation in rats,” *Investig. Ophthalmol. Vis. Sci.*, vol. 55, no. 1, pp. 600–611, 2014.

[77] M. J. Gallardo, N. Aggarwal, H. D. Cavanagh, and J. T. Whitson, “Progression of glaucoma associated with the sirsasana (headstand) yoga posture,” *Adv. Ther.*, vol. 23, no. 6, pp. 921–925, 2006.

[78] M. Baskaran, K. Raman, K. K. Ramani, J. Roy, L. Vijaya, and S. S. Badrinath, “Intraocular pressure changes and ocular biometry during Sirsasana (headstand posture) in yoga practitioners,” *Ophthalmology*, vol. 113, no. 8, pp. 1327–32, Aug. 2006.

[79] S. S. Siddique, A. M. Suelves, U. Baheti, and C. S. Foster, “Glaucoma and Uveitis,” *Surv. Ophthalmol.*, vol. 58, no. 1, pp. 1–10, 2013.

[80] W. C. Panek, G. N. Holland, D. A. Lee, and R. E. Christensen, “Glaucoma in patients with uveitis.,” *Br. J. Ophthalmol.*, vol. 74, no. 4, pp. 223–7, Apr. 1990.

[81] M. Choma, M. Sarunic, C. Yang, and J. Izatt, “Sensitivity advantage of swept source and Fourier domain optical coherence tomography,” *Opt. Express*, vol. 11, no. 18, p. 2183, 2003.

[82] O. Tan *et al.*, “*En face* Doppler total retinal blood flow measurement with 70 kHz spectral optical coherence tomography,” *J. Biomed. Opt.*, vol. 20, no. 6, p. 66004, 2015.

[83] B. K. Lee *et al.*, “Cardiac-gated en face doppler measurement of retinal blood flow using swept-source optical coherence tomography at 100,000 axial scans per second,” *Investig. Ophthalmol. Vis. Sci.*, vol. 56, no. 4, pp. 2522–2530, 2015.

[84] L. Guo *et al.*, “En face optical coherence tomography: a new method to analyse structural changes of the optic nerve head in rat glaucoma.,” *Br. J. Ophthalmol.*, vol. 89, no. 9, pp. 1210–1216, 2005.

[85] V. J. Srinivasan and H. Radhakrishnan, “Total average blood flow and angiography in the rat retina,” *J. Biomed. Opt.*, vol. 18, no. 7, p. 76025, 2013.

[86] C. J. Pedersen, D. Huang, M. A. Shure, and A. M. Rollins, “Measurement of absolute flow velocity vector using dual-angle, delay-encoded Doppler optical coherence tomography,” *Opt. Lett.*, vol. 32, no. 5, pp. 506–508, 2007.

[87] G. C. Aschinger *et al.*, “Effect of Diffuse Luminance Flicker Light Stimulation on Total Retinal Blood Flow Assessed With Dual-Beam Bidirectional Doppler OCT,” *Investig. Opthalmol. Vis. Sci.*, vol. 58, no. 2, p. 1167, 2017.

[88] C. Blatter *et al.*, “Dove prism based rotating dual beam bidirectional Doppler OCT,” *Biomed. Opt. Express*, vol. 4, no. 7, p. 1188, 2013.

[89] R. M. Werkmeister *et al.*, “Measurement of absolute blood flow velocity and blood flow in the human retina by dual-beam bidirectional Doppler Fourier-domain optical coherence tomography,” *Investig. Ophthalmol. Vis. Sci.*, vol. 53, no. 10, pp. 6062–6071, 2012.

[90] A. S. G. Singh, C. Kolbitsch, T. Schmoll, and R. a Leitgeb, “Stable absolute flow estimation with Doppler OCT based on virtual circumpapillary scans.,” *Biomed. Opt. Express*, vol. 1, no. 4, pp. 1047–1058, 2010.

[91] A. M. Shahidi, S. R. Patel, D. Huang, O. Tan, J. G. Flanagan, and C. Hudson, “Assessment of total retinal blood flow using Doppler Fourier Domain Optical Coherence Tomography during systemic hypercapnia and hypocapnia.,” *Physiol. Rep.*, vol. 2, no. 7, p. e12046, 2014.

[92] T. Nagaoka *et al.*, “Evaluation of retinal circulation using Segmental-Scanning doppler optical coherence tomography in anesthetized cats,” *Investig. Ophthalmol. Vis. Sci.*, vol. 57, no. 7, pp. 2936–2941, 2016.

[93] A. Mariampillai *et al.*, “Speckle variance detection of microvasculature using swept-source optical coherence tomography.,” *Opt. Lett.*, vol. 33, no. 13, pp. 1530–1532, 2008.

[94] M. S. Mahmud *et al.*, “Review of speckle and phase variance optical coherence tomography to visualize microvascular networks,” *J. Biomed. Opt.*, vol. 18, no. 5, p. 50901, 2013.

[95] Y. Zhao *et al.*, “Doppler standard deviation imaging for clinical monitoring of in vivo human skin blood flow.,” *Opt. Lett.*, vol. 25, no. 18, pp. 1358–60, 2000.

[96] H. Ren, Z. Ding, Y. Zhao, J. Miao, J. S. Nelson, and Z. Chen, “Phase-resolved functional optical coherence tomography: simultaneous imaging of in situ tissue structure, blood

flow velocity, standard deviation, birefringence, and Stokes vectors in human skin," *Opt. Lett.*, vol. 27, no. 19, p. 1702, 2002.

[97] E. Jonathan, J. Enfield, and M. J. Leahy, "Correlation mapping method for generating microcirculation morphology from optical coherence tomography (OCT) intensity images," *J. Biophotonics*, vol. 4, no. 9, pp. 583–587, 2011.

[98] C. Chen, W. Shi, and W. Gao, "Imaginary part-based correlation mapping optical coherence tomography for imaging of blood vessels in vivo," *J. Biomed. Opt.*, vol. 20, no. 11, p. 116009, 2015.

[99] Y. Jia *et al.*, "Split-spectrum amplitude-decorrelation angiography with optical coherence tomography.," *Opt. Express*, vol. 20, no. 4, pp. 4710–25, 2012.

[100] P. Li, Y. Cheng, L. Zhou, C. Pan, Z. Ding, and P. Li, "Single-shot angular compounded optical coherence tomography angiography by splitting full-space B-scan modulation spectrum for flow contrast enhancement," *Opt. Lett.*, vol. 41, no. 5, p. 1058, 2016.

[101] "The Electroretinogram: ERG by Ido Perlman – Webvision." [Online]. Available: http://webvision.med.utah.edu/book/electrophysiology/the-electroretinogram-erg/.

[102] Y.-C. Tham, X. Li, T. Y. Wong, H. A. Quigley, T. Aung, and C.-Y. Cheng, "Global Prevalence of Glaucoma and Projections of Glaucoma Burden through 2040," *Ophthalmology*, vol. 121, no. 11, pp. 2081–2090, Nov. 2014.

[103] B. C. Chauhan, "Canadian Glaucoma Study," *Arch. Ophthalmol.*, vol. 126, no. 8, p. 1030, 2008.

[104] Y. M. Buys *et al.*, "Comparison of newly diagnosed ocular hypertension and open-angle glaucoma: Ocular variables, risk factors, and disease severity," *J. Ophthalmol.*, vol. 2012, pp. 17–20, 2012.

[105] B. C. Chauhan *et al.*, "Canadian Glaucoma Study: 3. Impact of risk factors and intraocular pressure reduction on the rates of visual field change.," *Arch. Ophthalmol. (Chicago, Ill. 1960)*, vol. 128, no. 10, pp. 1249–55, Oct. 2010.

[106] M. O. Gordon and M. A. Kass, “The Ocular Hypertension Treatment Study,” vol. 117, no. May, pp. 573–583, 1999.

[107] L. Sanchez-Parra, S. Pardhan, R. J. Buckley, M. Parker, and R. R. A. Bourne, “Diurnal intraocular pressure and the relationship with swept-source OCT???derived anterior chamber dimensions in Angle closure: The IMPACT study,” *Investig. Ophthalmol. Vis. Sci.*, vol. 56, no. 5, pp. 2943–2949, 2015.

[108] N. Tojo, M. Oka, A. Miyakoshi, H. Ozaki, and A. Hayashi, “Comparison of Fluctuations of Intraocular Pressure Before and After Selective Laser Trabeculoplasty in Normal-tension Glaucoma Patients.,” *J. Glaucoma*, vol. 23, no. 8, pp. 138–143, 2013.

[109] T. R. Friberg and R. N. Weinreb, “Ocular manifestations of gravity inversion,” *Jama*, vol. 253, no. 12, pp. 1755–1757, 1985.

[110] M. Baskaran, K. Raman, K. K. Ramani, J. Roy, L. Vijaya, and S. S. Badrinath, “Intraocular Pressure Changes and Ocular Biometry during Sirsasana (Headstand Posture) in Yoga Practitioners,” *Ophthalmology*, vol. 113, no. 8, pp. 1327–1332, Aug. 2006.

[111] B. J. Frankfort *et al.*, “Elevated intraocular pressure causes inner retinal dysfunction before cell loss in a mouse model of experimental glaucoma,” *Investig. Ophthalmol. Vis. Sci.*, vol. 54, no. 1, pp. 762–770, 2013.

[112] B. V Bui, B. Edmunds, G. A. Cioffi, and B. Fortune, “The gradient of retinal functional changes during acute intraocular pressure elevation.,” *Investig. Ophthalmol. Vis. Sci.*, vol. 46, no. 1, pp. 202–13, Jan. 2005.

[113] P. A. Sieving and C. Nino, “Scotopic threshold response (STR) of the human electroretinogram.,” *Investig. Ophthalmol. Vis. Sci.*, vol. 29, no. 11, pp. 1608–14, Nov. 1988.

[114] K. M. Joos, C. Li, and R. M. Sappington, “Morphometric changes in the rat optic nerve following short-term intermittent elevations in intraocular pressure,” *Investig. Ophthalmol. Vis. Sci.*, vol. 51, no. 12, pp. 6431–6440, 2010.

[115] Y. Liu, C. M. McDowell, Z. Zhang, H. E. Tebow, R. J. Wordinger, and A. F. Clark,

"Monitoring retinal morphologic and functional changes in mice following optic nerve crush," *Investig. Ophthalmol. Vis. Sci.*, vol. 55, no. 6, pp. 3766–3774, 2014.

[116] Z. Zhi, W. O. Cepurna, E. C. Johnson, J. C. Morrison, and R. K. Wang, "Impact of intraocular pressure on changes of blood flow in the retina, choroid, and optic nerve head in rats investigated by optical microangiography," *Biomed. Opt. Express*, vol. 3, no. 9, p. 2220, 2012.

[117] Y. Zhao *et al.*, "Changes in retinal morphology, electroretinogram and visual behavior after transient global ischemia in adult rats.," *PLoS One*, vol. 8, no. 6, p. e65555, Jan. 2013.

[118] B. V. Bui and B. Fortune, "Ganglion cell contributions to the rat full-field electroretinogram," *J. Physiol.*, vol. 555, no. 1, pp. 153–173, 2004.

[119] A. A. Moayed *et al.*, "Combined optical coherence tomography and electroretinography system for in vivo simultaneous morphological and functional imaging of the rodent retina.," *J. Biomed. Opt.*, vol. 15, no. 4, p. 40506, 2014.

[120] A. Moshiri *et al.*, "Near complete loss of retinal ganglion cells in the math5/brn3b double knockout elicits severe reductions of other cell types during retinal development.," *Dev. Biol.*, vol. 316, no. 2, pp. 214–27, Apr. 2008.

[121] S. M. Saszik, J. G. Robson, and L. J. Frishman, "The scotopic threshold response of the dark-adapted electroretinogram of the mouse," *J. Physiol.*, vol. 543, no. 3, pp. 899–916, Jul. 2002.

[122] Y. You, V. K. Gupta, J. C. Li, N. Al-Adawy, A. Klistorner, and S. L. Graham, "FTY720 Protects Retinal Ganglion Cells in Experimental Glaucoma," *Investig. Opthalmol. Vis. Sci.*, vol. 55, no. 5, p. 3060, 2014.

[123] C. F. Burgoyne, J. C. Downs, A. J. Bellezza, and R. T. Hart, "Three-dimensional reconstruction of normal and early glaucoma monkey optic nerve head connective tissues," *Investig. Ophthalmol. Vis. Sci.*, vol. 45, no. 12, pp. 4388–4399, 2004.

[124] B. Fortune *et al.*, "The effect of acute intraocular pressure elevation on peripapillary

retinal thickness, retinal nerve fiber layer thickness, and retardance.," *Investig. Ophthalmol. Vis. Sci.*, vol. 50, no. 10, pp. 4719–4726, 2009.

[125] H. A. Quigley, "The Pathogenesis of Reversible Cupping in Congenital Glaucoma," *Am. J. Ophthalmol.*, vol. 84, no. 3, pp. 358–370, Sep. 1977.

[126] B. V Bui, A. H. Batcha, E. Fletcher, V. H. Y. Wong, and B. Fortune, "Relationship between the magnitude of intraocular pressure during an episode of acute elevation and retinal damage four weeks later in rats," *PLoS One*, vol. 8, no. 7, p. e70513, Jan. 2013.

[127] C. A. Westall *et al.*, "Values of electroretinogram responses according to axial length," *Doc. Ophthalmol.*, vol. 102, no. 2, pp. 115–130, 2001.

[128] H. A. Quigley, "The Pathogenesis of Reversible Cupping in Congenital Glaucoma," *Am. J. Ophthalmol.*, vol. 84, no. 3, pp. 358–370, Sep. 1977.

[129] D. B. Yan, F. M. Coloma, A. Metheetrairut, G. E. Trope, J. G. Heathcote, and C. R. Ethier, "Deformation of the lamina cribrosa by elevated intraocular pressure ," *Br. J. Ophthalmol.*, vol. 78, no. 8, pp. 643–648, 1994.

[130] D. Zhao, Z. He, A. J. Vingrys, B. V. Bui, and C. T. O. Nguyen, "The effect of intraocular and intracranial pressure on retinal structure and function in rats," *Physiol. Rep.*, vol. 3, no. 8, p. e12507, 2015.

[131] S. Deng *et al.*, "Autophagy in retinal ganglion cells in a rhesus monkey chronic hypertensive glaucoma model.," *PLoS One*, vol. 8, no. 10, p. e77100, Jan. 2013.

[132] A. U. Bayer *et al.*, "Retinal morphology and ERG response in the DBA/2NNia mouse model of angle-closure glaucoma," *Investig. Ophthalmol. Vis. Sci.*, vol. 42, no. 6, pp. 1258–1265, 2001.

[133] L. L. Fernández-Sánchez, L. P. De Sevilla Müller, N. C. Brecha, and N. Cuenca, "Loss of outer retinal neurons and circuitry alterations in the DBA/2J mouse," *Investig. Ophthalmol. Vis. Sci.*, vol. 55, no. 9, pp. 6059–6072, 2014.

[134] Vaegan, S. L. Graham, I. Goldberg, L. Buckland, and F. C. Hollows, "Flash and pattern

electroretinogram changes with optic atrophy and glaucoma," *Exp. Eye Res.*, vol. 60, no. 6, pp. 697–706, 1995.

[135] E. Wittstrom, P. Schatz, M. Lövestam-Adrian, V. Ponjavic, A. Bergström, and S. Andréasson, "Improved retinal function after trabeculectomy in glaucoma patients," *Graefe's Arch. Clin. Exp. Ophthalmol.*, vol. 248, no. 4, pp. 485–495, 2010.

[136] M. Gur, Y. Y. Zeevi, M. Bielik, and E. Neumann, "Changes in the oscillatory potentials of the electroretinogram in glaucoma," *Curr. Eye Res.*, vol. 6, no. 3, pp. 457–466, Jan. 1987.

[137] K. Holopigian, W. Seiple, C. Mayron, R. Koty, and M. Lorenzo, "Electrophysiological and psychophysical flicker sensitivity in patients with primary open angle glaucoma and ocular hypertension," *Investig. Ophthalmol. Vis Sci*, vol. 31, no. 9, pp. 1863–1868, 1990.

[138] Y. J. Chen *et al.*, "Protective effects of glucosamine on oxidative-stress and ischemia/reperfusion-induced retinal injury," *Investig. Ophthalmol. Vis. Sci.*, vol. 56, no. 3, pp. 1506–1516, 2015.

[139] P. Olivier, F. B. Jolicoeur, G. Lafond, A. L. Drumheller, and J. R. Brunette, "Dose related effects of 6-OHDA on rabbit retinal dopamine concentrations and ERG B-wave amplitudes.," *Brain Res. Bull.*, vol. 16, no. 5, pp. 751–3, May 1986.

[140] W. Skrandies and H. Wässle, "Dopamine and serotonin in cat retina: electroretinography and histology," *Exp. brain Res.*, 1988.

[141] J. M. Jagadeesh, H. C. Lee, and M. Salazar-Bookaman, "Influence of chlorpromazine on the rabbit electroretinogram," *Investig. Ophthalmol. Vis. Sci.*, vol. 19, no. 12, pp. 1449–1456, 1980.

[142] T. Schneider and E. Zrenner, "Effects of D-1 and D-2 dopamine antagonists on ERG and optic nerve response of the cat," *Exp. Eye Res.*, vol. 52, no. 4, pp. 425–430, Apr. 1991.

[143] D. A. Fox, S. V. Kala, W. R. Hamilton, J. E. Johnson, and J. P. O'Callaghan, "Low-level human equivalent gestational lead exposure produces supernormal scotopic electroretinograms, increased retinal neurogenesis and decreased retinal dopamine utilization in rats," *Environ. Health Perspect.*, vol. 116, no. 5, pp. 618–625, 2008.

[144] S. J. Rothenberg *et al.*, “Increased ERG a- and b-wave amplitudes in 7- to 10-year-old children resulting from prenatal lead exposure,” *Investig. Ophthalmol. Vis. Sci.*, vol. 43, no. 6, pp. 2036–2044, 2002.

[145] M. Joseph Phillips *et al.*, “Retinal function and structure in ant1-deficient mice,” *Investig. Ophthalmol. Vis. Sci.*, vol. 51, no. 12, pp. 6744–6752, 2010.

[146] A. Khan Kareem *et al.*, “Prolonged elevation of intraocular pressure results in retinal ganglion cell loss and abnormal retinal function in mice,” *Exp. Eye Res.*, vol. 130, pp. 29–37, 2015.

[147] M. Suh, Y. Sauvé, K. J. Merrells, J. X. Kang, and D. W. L. Ma, “Supranormal electroretinogram in fat-1 mice with retinas enriched in docosahexaenoic acid and n-3 very long chain fatty acids (C24-C36),” *Investig. Ophthalmol. Vis. Sci.*, vol. 50, no. 9, pp. 4394–4401, 2009.

[148] F. Montiani-Ferreira, G. C. Shaw, A. M. Geller, and S. M. Petersen-Jones, “Electroretinographic features of the retinopathy, globe enlarged (rge) chick phenotype.,” *Mol. Vis.*, vol. 13, pp. 553–65, Apr. 2007.

[149] A. Vincent, A. G. Robson, and G. E. Holder, “PATHOGNOMONIC (DIAGNOSTIC) ERGs A Review and Update,” *Retina*, vol. 33, no. 1, pp. 5–12, 2013.

[150] N. J. Ward, K. W. Ho, W. S. Lambert, C. Weitlauf, and D. J. Calkins, “Absence of transient receptor potential vanilloid-1 accelerates stress-induced axonopathy in the optic projection,” *J. Neurosci.*, vol. 34, no. 9, pp. 3161–70, Feb. 2014.

[151] A. Vielma, L. Delgado, C. Elgueta, R. Osorio, A. G. Palacios, and O. Schmachtenberg, “Nitric oxide amplifies the rat electroretinogram,” *Exp. Eye Res.*, vol. 91, no. 5, pp. 700–709, 2010.

[152] J. Cudeiro and C. Rivadulla, “Sight and insight – on the physiological role of nitric oxide in the visual system,” *Trends Neurosci.*, vol. 22, no. 3, pp. 109–116, 1999.

[153] M. B. Djamgoz *et al.*, “Light-adaptive role of nitric oxide in the outer retina of lower vertebrates: a brief review.,” *Philos. Trans. R. Soc. Lond. B. Biol. Sci.*, vol. 355, no. 1401,

pp. 1199–203, 2000.

[154] B. Hoffpauir, E. McMains, and E. Gleason, “Nitric oxide transiently converts synaptic inhibition to excitation in retinal amacrine cells.,” *J. Neurophysiol.*, vol. 95, no. 5, pp. 2866–77, 2006.

[155] S. L. Mills and S. C. Massey, “Differential properties of two gap junctional pathways made by AII amacrine cells,” *Nature*, vol. 377, no. 6551, pp. 734–737, Oct. 1995.

[156] G. Y. Wang, L. C. Liets, and L. M. Chalupa, “Nitric oxide differentially modulates ON and OFF responses of retinal ganglion cells,” *J Neurophysiol*, vol. 90, no. 2, pp. 1304–1313, 2003.

[157] M. Sato, T. Ohtsuka, and W. K. Stell, “Endogenous nitric oxide enhances the light-response of cones during light-adaptation in the rat retina,” *Vision Res.*, vol. 51, no. 1, pp. 131–137, 2011.

[158] M. Sato and T. Ohtsuka, “Opposite effects of nitric oxide on rod and cone photoreceptors of rat retina in situ,” *Neurosci. Lett.*, vol. 473, no. 1, pp. 62–66, 2010.

[159] H. Oku, H. Yamaguchi, T. Sugiyama, S. Kojima, M. Ota, and I. Azuma, “Retinal toxicity of nitric oxide released by administration of a nitric oxide donor in the albino rabbit,” *Investig. Ophthalmol. Vis. Sci.*, vol. 38, no. 12, pp. 2540–2544, 1997.

[160] M. Kobayashi, “Nitric Oxide Synthase Expression in Ischemic Rat Retinas,” *Jpn. J. Ophthalmol.*, vol. 44, no. 3, pp. 235–244, Jun. 2000.

[161] A. H. Neufeld, M. R. Hernandez, and M. Gonzalez, “Nitric Oxide Synthase in the Human Glaucomatous Optic Nerve Head,” *Arch. Ophthalmol.*, vol. 115, no. 4, p. 497, Apr. 1997.

[162] K. Takahata *et al.*, “Retinal neuronal death induced by intraocular administration of a nitric oxide donor and its rescue by neurotrophic factors in rats,” *Investig. Ophthalmol. Vis. Sci.*, vol. 44, no. 4, pp. 1760–1766, 2003.

[163] I. M. Goldstein, P. Ostwald, and S. Roth, “Nitric oxide: a review of its role in retinal function and disease.,” *Vision Res.*, vol. 36, no. 18, pp. 2979–2994, 1996.

[164] A. H. Neufeld, “Nitric oxide: a potential mediator of retinal ganglion cell damage in glaucoma.,” *Surv. Ophthalmol.*, vol. 43 Suppl 1, no. June, pp. S129-35, Jun. 1999.

[165] A. W. Siu, M. C. P. Leung, C. Ho To, F. K. W. Siu, J. Z. Ji, and K. Fai So, “Total retinal nitric oxide production is increased in intraocular pressure-elevated rats,” *Exp. Eye Res.*, vol. 75, no. 4, pp. 401–406, 2002.

[166] L. Vidal, F. Díaz, A. Villena, M. Moreno, J. G. Campos, and I. P. de Vargas, “Nitric oxide synthase in retina and optic nerve head of rat with increased intraocular pressure and effect of timolol.,” *Brain Res. Bull.*, vol. 70, no. 4–6, pp. 406–13, Oct. 2006.

[167] N. Cuenca *et al.*, “Changes in the inner and outer retinal layers after acute increase of the intraocular pressure in adult albino Swiss mice,” *Exp. Eye Res.*, vol. 91, no. 2, pp. 273–285, 2010.

[168] S. Shareef, A. Sawada, and A. H. Neufeld, “Isoforms of Nitric Oxide Synthase in the Optic Nerves Intraocular Pressure,” *Investig. Ophthalmol. Vis. Sci.*, vol. 40, no. 12, pp. 2884–2891, 1999.

[169] C. E. Riva, S. Harino, B. L. Petrig, and R. D. Shonat, “Laser Doppler flowmetry in the optic nerve.,” *Exp. Eye Res.*, vol. 55, no. 3, pp. 499–506, 1992.

[170] E. Polska *et al.*, “Regulation of choroidal blood flow during combined changes in intraocular pressure and arterial blood pressure,” *Investig. Ophthalmol. Vis. Sci.*, vol. 48, no. 8, pp. 3768–3774, 2007.

[171] W. J. Lavery, E. R. Muir, J. W. Kiel, and T. Q. Duong, “Magnetic resonance imaging indicates decreased choroidal and retinal blood flow in the DBA/2J mouse model of glaucoma.,” *Investig. Ophthalmol. Vis. Sci.*, vol. 53, no. 2, pp. 560–4, 2012.

[172] Q. Wang *et al.*, “Imaging retinal capillaries using ultrahigh-resolution optical coherence tomography and adaptive optics,” *Investig. Ophthalmol. Vis. Sci.*, vol. 52, no. 9, pp. 6292–6299, 2011.

[173] a. Pinhas *et al.*, “Assessment of Perfused Foveal Microvascular Density and Identification of Nonperfused Capillaries in Healthy and Vasculopathic Eyes,” *Investig. Ophthalmol.*

Vis. Sci., vol. 55, no. 12, pp. 8056–8066, 2014.

[174] Z. He, A. J. Vingrys, J. A. Armitage, and B. V. Bui, "The role of blood pressure in glaucoma," *Clin. Exp. Optom.*, vol. 94, no. 2, pp. 133–149, 2011.

[175] A. Gurdita, B. Tan, K. M. Joos, K. Bizheva, and V. Choh, "Pigmented and albino rats differ in their responses to moderate, acute and reversible intraocular pressure elevation," *Doc. Ophthalmol.*, pp. 1–15, 2017.

[176] Z. He, J. K. H. Lim, C. T. O. Nguyen, A. J. Vingrys, and B. V Bui, "Coupling blood flow and neural function in the retina: a model for homeostatic responses to ocular perfusion pressure challenge," *Physiol. Rep.*, vol. 1, no. 3, p. e00055, 2013.

[177] A. A. Moayed, S. Hariri, V. Choh, and K. Bizheva, "In vivo imaging of intrinsic optical signals in chicken retina with functional optical coherence tomography," *Opt. Lett.*, vol. 36, no. 23, p. 4575, 2011.

[178] B. Tan, E. Mason, B. MacLellan, and K. K. Bizheva, "Correlation of Visually Evoked Functional and Blood Flow Changes in the Rat Retina Measured With a Combined OCT+ERG System," *Investig. Opthalmol. Vis. Sci.*, vol. 58, no. 3, p. 1673, 2017.

[179] V. Resta *et al.*, "Acute retinal ganglion cell injury caused by intraocular pressure spikes is mediated by endogenous extracellular ATP," *Eur. J. Neurosci.*, vol. 25, no. 9, pp. 2741–2754, 2007.

[180] H. A. Quigley and D. R. Anderson, "Distribution of axonal transport blockade by acute intraocular pressure elevation in the primate optic nerve head," *Investig. Ophthalmol. Vis. Sci.*, vol. 16, no. 7, pp. 640–644, 1977.

[181] Z. He, C. T. O. Nguyen, J. A. Armitage, A. J. Vingrys, and B. V. Bui, "Blood pressure modifies retinal susceptibility to intraocular pressure elevation," *PLoS One*, vol. 7, no. 2, p. e31104, 2012.

[182] V. H. Y. Wong, A. J. Vingrys, A. I. Jobling, and B. V Bui, "Susceptibility of streptozotocin-induced diabetic rat retinal function and ocular blood flow to acute intraocular pressure challenge.," *Investig. Ophthalmol. Vis. Sci.*, vol. 54, no. 3, pp. 2133–

2141, 2013.

[183] V. Choh, A. Gurdita, B. Tan, R. C. Prasad, K. Bizheva, and K. M. Joos, “Short-term moderately elevated intraocular pressure is associated with elevated scotopic electroretinogram responses,” *Investig. Ophthalmol. Vis. Sci.*, vol. 57, no. 4, pp. 2140–2151, 2016.

[184] V. Choh *et al.*, “Isoflurane and ketamine:xylazine differentially affect intraocular pressure-associated scotopic threshold responses in Sprague-Dawley rats,” *Doc. Ophthalmol.*, 2017.

[185] S. Hariri, A. A. Moayed, A. Dracopoulos, C. Hyun, S. Boyd, and K. Bizheva, “Limiting factors to the OCT axial resolution for in-vivo imaging of human and rodent retina in the 1060nm wavelength range,” *Opt. Express*, vol. 17, no. 26, pp. 24304–24316, 2009.

[186] S. Marschall, A. Gawish, Y. Feng, L. Sorbara, P. Fieguth, and K. Bizheva, “In-vivo imaging of keratoconic corneas using high-speed high-resolution swept-source OCT,” 2013, p. 88020P.

[187] V. J. Srinivasan and H. Radhakrishnan, “Total average blood flow and angiography in the rat retina,” *J. Biomed. Opt.*, vol. 18, no. 7, p. 76025, 2013.

[188] V. J. Srinivasan *et al.*, “Quantitative cerebral blood flow with optical coherence tomography,” *Opt.Express*, vol. 18, no. 3, pp. 2477–2494, 2010.

[189] W. J. N. K. L. V. M. a. V. Ro F. Frangi, “Multiscale vessel enhancement filtering,” *Med. Image Comput. Comput. Assist. Interv.*, vol. 1496, pp. 130–137, 1998.

[190] P. Smith, D. B. Reid, C. Environment, L. Palo, P. Alto, and P. L. Smith, “Smith et al. - 1979 - A Tlreshold Selection Method from Gray-Level Histograms,” vol. 20, no. 1, pp. 62–66, 1979.

[191] F. Tayyari *et al.*, “Variability and repeatability of quantitative, fourier-domain optical coherence tomography doppler blood flow in young and elderly healthy subjects,” *Investig. Ophthalmol. Vis. Sci.*, vol. 55, no. 12, pp. 7716–7725, 2014.

[192] T. E. Kornfield and E. A. Newman, “Measurement of Retinal Blood Flow Using Fluorescently Labeled Red Blood Cells.,” *eNeuro*, vol. 2, no. 2, pp. 1–13, 2015.

[193] L. Wang, G. Cull, C. F. Burgoyne, S. Thompson, and B. Fortune, “Longitudinal alterations in the dynamic autoregulation of optic nerve head blood flow revealed in experimental glaucoma,” *Investig. Ophthalmol. Vis. Sci.*, vol. 55, no. 6, pp. 3509–3516, 2014.

[194] M. Nagahara, Y. Tamaki, M. Araie, and S. Eguchi, “EVects of scleral buckling and encircling procedures on human optic nerve head and retinochoroidal circulation.”

[195] R. Sugawara *et al.*, “Choroidal blood flow in the foveal region in eyes with rhegmatogenous retinal detachment and scleral buckling procedures,” *Br J Ophthalmol*, vol. 90, pp. 1363–1365, 2006.

[196] C. D. Regillo, R. C. Sergott, and G. C. Brown, “Successful Scleral Buckling Procedures Decrease Central Retinal Artery Blood Flow Velocity,” *Ophthalmology*, vol. 100, no. 7, pp. 1044–1049, Jul. 1993.

[197] H. Ogasawara, G. T. Feke, A. Yoshida, M. T. Milbocker, J. J. Weiter, and J. W. McMeel, “Retinal blood flow alterations associated with scleral buckling and encircling procedures,” *Br J Ophthalmol*, vol. 76, no. 5, pp. 275–279, 1992.

[198] Z. Zhi, W. Cepurna, E. Johnson, H. Jayaram, J. Morrison, and R. K. Wang, “Evaluation of the effect of elevated intraocular pressure and reduced ocular perfusion pressure on retinal capillary bed filling and total retinal blood flow in rats by OMAG/OCT,” *Microvasc. Res.*, vol. 101, pp. 86–95, 2015.

[199] I. Perlman, “Relationship between the amplitudes of the b wave and the a wave as a useful index for evaluating the electroretinogram.,” *Br. J. Ophthalmol.*, vol. 67, no. 7, pp. 443–448, 1983.

[200] Y. Matsui, O. Katsumi, H. Sakaue, and T. Hirose, “Electroretinogram b/a wave ratio improvement in central retinal vein obstruction.,” *Br. J. Ophthalmol.*, vol. 78, no. 3, pp. 191–8, 1994.

[201] S. Yasuda *et al.*, “Significant correlation between electroretinogram parameters and ocular vascular endothelial growth factor concentration in central retinal vein occlusion eyes,” *Investig. Ophthalmol. Vis. Sci.*, vol. 52, no. 8, pp. 5737–5742, 2011.

[202] C. S. Matsumoto, K. Shinoda, and K. Nakatsuka, “High correlation of scotopic and photopic electroretinogram components with severity of central retinal artery occlusion,” *Clin. Ophthalmol.*, vol. 5, no. 1, pp. 115–121, 2011.

[203] P. Speros and J. Price, “Oscillatory potentials. History, techniques and potential use in the evaluation of disturbances of retinal circulation,” *Surv. Ophthalmol.*, vol. 25, no. 4, pp. 237–252, Jan. 1981.

[204] H. A. Hancock and T. W. Kraft, “Oscillatory potential analysis and ERGs of normal and diabetic rats,” *Investig. Ophthalmol. Vis. Sci.*, vol. 45, no. 3, pp. 1002–1008, 2004.

[205] H. Asi and I. Perlman, “Relationships between the electroretinogram a-wave, b-wave and oscillatory potentials and their application to clinical diagnosis,” *Doc. Ophthalmol.*, vol. 79, no. 2, pp. 125–139, 1992.

[206] H. a Quigley and E. M. Addicks, “Chronic experimental glaucoma in primates,” *Methods*, pp. 126–136, 1980.

[207] D. R. Anderson and A. Hendrickson, “The effect of elevated intraocular pressure on axoplasmic transport in the optic nerve of the rhesus monkey.,” *Investig. Ophthalmol. Vis. Sci*, vol. 13, pp. 771–783, 1974.

[208] N. N. Osborne, J. P. Wood, G. Chidlow, J. H. Bae, J. Melena, and M. S. Nash, “Ganglion cell death in glaucoma: what do we really know?,” *Br. J. Ophthalmol.*, vol. 83, no. 8, pp. 980–986, 1999.

[209] S. Mosaed, J. H. K. Liu, and R. N. Weinreb, “Correlation between office and peak nocturnal intraocular pressures in healthy subjects and glaucoma patients,” *Am. J. Ophthalmol.*, vol. 139, no. 2, pp. 320–324, 2005.

[210] J. H. K. Liu, R. P. Bouligny, D. F. Kripke, and R. N. Weinreb, “Nocturnal elevation of intraocular pressure is detectable in the sitting position,” *Investig. Ophthalmol. Vis. Sci.*,

vol. 44, no. 10, pp. 4439–4442, 2003.

[211] S. D. Grozdanic, D. M. Betts, D. S. Sakaguchi, R. A. Allbaugh, Y. H. Kwon, and R. H. Kardon, “Laser-Induced Mouse Model of Chronic Ocular Hypertension,” *Investig. Opthalmol. Vis. Sci.*, vol. 44, no. 10, p. 4337, 2003.

[212] H.-H. Liu and J. G. Flanagan, “A Mouse Model of Chronic Ocular Hypertension Induced by Circumlimbal Suture,” *Investig. Opthalmol. Vis. Sci.*, vol. 58, no. 1, p. 353, 2017.

[213] T. S. Prata, C. G. V De Moraes, F. N. Kanadani, R. Ritch, and A. Paranhos, “Posture-induced intraocular pressure changes: Considerations regarding body position in glaucoma patients,” *Surv. Ophthalmol.*, vol. 55, no. 5, pp. 445–453, 2010.

[214] S. S. Siddique, A. M. Suelves, U. Baheti, and C. S. Foster, “Glaucoma and Uveitis,” *Surv. Ophthalmol.*, vol. 58, no. 1, pp. 1–10, 2013.

[215] O. W. Gramlich *et al.*, “Dynamics, alterations, and consequences of minimally invasive intraocular pressure elevation in rats,” *Investig. Ophthalmol. Vis. Sci.*, vol. 55, no. 1, pp. 600–611, 2014.

[216] C. J. Abbott, T. E. Choe, T. A. Lusardi, C. F. Burgoyne, L. Wang, and B. Fortune, “Evaluation of retinal nerve fiber layer thickness and axonal transport 1 and 2 weeks after 8 hours of acute intraocular pressure elevation in rats,” *Investig. Ophthalmol. Vis. Sci.*, vol. 55, no. 2, pp. 674–687, 2014.

[217] J. G. Crowston *et al.*, “An acute intraocular pressure challenge to assess retinal ganglion cell injury and recovery in the mouse,” *Exp. Eye Res.*, vol. 141, pp. 3–8, 2014.

[218] Dirk-Jan Kroon, “Region Growing - File Exchange - MATLAB Central.” [Online]. Available: https://www.mathworks.com/matlabcentral/fileexchange/19084-region-growing. [Accessed: 02-Jul-2017].

[219] D. M. Inman, R. M. Sappington, P. J. Horner, and D. J. Calkins, “Quantitative correlation of optic nerve pathology with ocular pressure and corneal thickness in the DBA/2 mouse model of glaucoma,” *Investig. Ophthalmol. Vis. Sci.*, vol. 47, no. 3, pp. 986–996, 2006.

[220] W. S. Bond *et al.*, “Virus-mediated EpoR76E Therapy Slows Optic Nerve Axonopathy in Experimental Glaucoma,” *Mol. Ther.*, vol. 24, no. 2, pp. 230–239, 2016.

[221] C. F. Burgoyne, H. A. Quigley, H. W. Thompson, S. Vitale, and R. Varma, “Early changes in optic disc compliance and surface position in experimental glaucoma.,” *Ophthalmology*, vol. 102, no. 12, pp. 1800–1809, 1995.

[222] A. Gurdita, B. Tan, K. M. Joos, K. Bizheva, and V. Choh, “Pigmented and albino rats differ in their responses to moderate, acute and reversible intraocular pressure elevation,” *Doc. Ophthalmol.*, pp. 1–15, 2017.

[223] H. H. Liu, Z. He, C. T. O. Nguyen, A. J. Vingrys, and B. V. Bui, “Reversal of functional loss in a rat model of chronic intraocular pressure elevation,” *Ophthalmic Physiol. Opt.*, vol. 37, pp. 71–81, 2016.

[224] S. Remtulla and P. E. Hallett, “A schematic eye for the mouse, and comparisons with the rat,” *Vision Res.*, vol. 25, no. 1, pp. 21–31, 1985.

[225] L. Panagis, X. Zhao, Y. Ge, L. Ren, T. W. Mittag, and J. Danias, “Retinal gene expression changes related to IOP exposure and axonal loss in DBA/2J mice,” *Investig. Ophthalmol. Vis. Sci.*, vol. 52, no. 11, pp. 7807–7816, 2011.

[226] Z. He, A. J. Vingrys, J. A. Armitage, C. T. Nguyen, and B. V. Bui, “Chronic hypertension increases susceptibility to acute IOP challenge in rats,” *Investig. Ophthalmol. Vis. Sci.*, vol. 55, no. 12, pp. 7888–7895, 2014.

[227] I. Dielemans, J. R. Vingerling, D. Algra, A. Hofman, D. E. Grobbee, and P. T. V. M. de Jong, “Primary Open-angle Glaucoma, Intraocular Pressure, and Systemic Blood Pressure in the General Elderly Population,” *Ophthalmology*, vol. 102, no. 1, pp. 54–60, 1995.

[228] A. Alm and A. Bill, “Ocular and optic nerve blood flow at normal and increased intraocular pressures in monkeys (Macaca irus): a study with radioactively labelled microspheres including flow determinations in brain and some other tissues,” *Exp. Eye Res.*, vol. 15, no. 1, pp. 15–29, 1973.

[229] J. B. Jonas and S. S. Hayreh, “Localised retinal nerve fibre layer defects in chronic

experimental high pressure glaucoma in rhesus monkeys.," *Br. J. Ophthalmol.*, vol. 83, no. 11, pp. 1291–5, 1999.

[230] D. Schmidl, G. Garhofer, and L. Schmetterer, "The complex interaction between ocular perfusion pressure and ocular blood flow - Relevance for glaucoma," *Exp. Eye Res.*, vol. 93, no. 2, pp. 141–155, 2011.

[231] B. Pemp *et al.*, "Reduced retinal vessel response to flicker stimulation but not to exogenous nitric oxide in type 1 diabetes," *Investig. Ophthalmol. Vis. Sci.*, vol. 50, no. 9, pp. 4029–4032, 2009.

[232] A. Scheiner, C. Riva, K. K, and B. Petrig, "Effect of flicker an macular blood-flow asessed by the blue field simulation technique," *Investig. Ophthalmol. Vis. Sci.*, vol. 35, no. 9, pp. 3436–3441, 1994.

[233] V. Van Toi and C. E. Riva, "Sinusoidal Flicker Stimulation in Cats," pp. 189–202, 1994.

[234] J. Kiryu, S. Asrani, M. Shahidi, M. Mori, and R. Zeimer, "Local response of the primate retinal microcirculation to increased metabolic demand induced by flicker," *Investig. Ophthalmol. Vis. Sci.*, vol. 36, no. 7, pp. 1240–1246, 1995.

[235] Y. Y. Shih *et al.*, "Quantitative retinal and choroidal blood flow during light, dark adaptation and flicker light stimulation in rats using fluorescent microspheres," *Curr Eye Res*, vol. 38, no. 2, pp. 292–298, 2013.

[236] E. Chaigneau, M. Oheim, E. Audinat, and S. Charpak, "Two-photon imaging of capillary blood flow in olfactory bulb glomeruli.," *Proc. Natl. Acad. Sci. U. S. A.*, vol. 100, no. 22, pp. 13081–6, 2003.

[237] Y. Wang, A. A. Fawzi, O. Tan, X. Zhang, and D. Huang, "Flicker-induced changes in retinal blood flow assessed by Doppler optical coherence tomography," *Biomed Opt Express*, vol. 2, no. 7, pp. 1852–1860, 2011.

[238] E. Wei *et al.*, "Parafoveal retinal vascular response to pattern visual stimulation assessed with OCT angiography," *PLoS One*, vol. 8, no. 12, pp. 1–7, 2013.

[239] W. Choi, B. Baumann, A. C. Clermont, E. P. Feener, D. A. Boas, and J. G. Fujimoto, "Functional imaging of hemodynamic stimulus response in the rat retina with ultrahigh-speed spectral / Fourier domain OCT," *SPIE BiOS*, vol. 8567, p. 85671C, 2013.

[240] A. D. Pechauer, A. D. Pechauer, D. Huang, and Y. Jia, "Detecting Blood Flow Response to Stimulation of the Human Eye Detecting Blood Flow Response to Stimulation of the Human Eye," *Biomed Res. Int.*, vol. 2015, p. 14, 2015.

[241] B. Falsini *et al.*, "The fundamental and second harmonic of the photopic flicker electroretinogram: Temporal frequency-dependent abnormalities in retinitis pigmentosa," *Clin. Neurophysiol.*, vol. 110, no. 9, pp. 1554–1562, 1999.

[242] C. E. Riva, E. Logean, and B. Falsini, "Visually evoked hemodynamical response and assessment of neurovascular coupling in the optic nerve and retina," *Prog. Retin. Eye Res.*, vol. 24, no. 2, pp. 183–215, 2005.

[243] S. Hariri, M. C. Tam, D. Lee, D. Hileeto, A. A. Moayed, and K. Bizheva, "Noninvasive imaging of the early effect of sodium iodate toxicity in a rat model of outer retina degeneration with spectral domain optical coherence tomography," *J. Biomed. Opt.*, vol. 18, no. 2, p. 26017, 2013.

[244] A. A. Moayed *et al.*, "Combined optical coherence tomography and electroretinography system for in vivo simultaneous morphological and functional imaging of the rodent retina.," *J. Biomed. Opt.*, vol. 15, no. 4, p. 40506, 2014.

[245] M. Guizar-Sicairos, S. T. Thurman, and J. R. Fienup, "Efficient subpixel image registration algorithms.," *Opt. Lett.*, vol. 33, no. 2, pp. 156–158, 2008.

[246] D. L. McCulloch *et al.*, "ISCEV Standard for full-field clinical electroretinography (2015 update)," *Doc. Ophthalmol.*, vol. 130, no. 1, pp. 1–12, 2015.

[247] T. E. Kornfield and E. A. Newman, "Regulation of Blood Flow in the Retinal Trilaminar Vascular Network," *J. Neurosci.*, vol. 34, no. 34, pp. 11504–11513, 2014.

[248] H. Radhakrishnan and V. J. Srinivasan, "Multiparametric optical coherence tomography imaging of the inner retinal hemodynamic response to visual stimulation," *J Biomed Opt*,

vol. 18, no. 8, p. 86010, 2013.

[249] R. M. Werkmeister *et al.*, “Measurement of retinal blood flow in the rat by combining Doppler Fourier-domain optical coherence tomography with fundus imaging,” *J. Biomed. Opt.*, vol. 19, no. 10, p. 106008, 2014.

[250] J. Lee, J. Y. Jiang, W. Wu, F. Lesage, and D. a. Boas, “Statistical intensity variation analysis for rapid volumetric imaging of capillary network flux,” *Biomed. Opt. Express*, vol. 5, no. 4, pp. 1160–1172, 2014.

[251] H. Ren, C. Du, K. Park, N. D. Volkow, and Y. Pan, “Quantitative imaging of red blood cell velocity invivo using optical coherence Doppler tomography,” *Appl. Phys. Lett.*, vol. 100, no. 23, pp. 1–5, 2012.

[252] K. Bizheva *et al.*, “Optophysiology: depth-resolved probing of retinal physiology with functional ultrahigh-resolution optical coherence tomography.,” *Proc. Natl. Acad. Sci. U. S. A.*, vol. 103, no. 13, pp. 5066–5071, 2006.

[253] B. Wang, Y. Lu, and X. Yao, “*In vivo* optical coherence tomography of stimulus-evoked intrinsic optical signals in mouse retinas,” *J. Biomed. Opt.*, vol. 21, no. 9, p. 96010, 2016.

[254] V. J. Srinivasan, M. Wojtkowski, and J. G. Fujimoto, “In vivo measurement of retinal physiology with high-speed ultrahigh-resolution optical coherence tomography,” vol. 31, no. 15, pp. 2308–2310, 2006.

[255] D. Hillmann, H. Spahr, C. Pfäffle, H. Sudkamp, G. Franke, and G. Hüttmann, “In vivo optical imaging of physiological responses to photostimulation in human photoreceptors,” *Proc. Natl. Acad. Sci.* , vol. 113, no. 46, pp. 13138–13143, 2016.

[256] N. R. Kim, E. S. Lee, G. J. Seong, J. H. Kim, H. G. An, and C. Y. Kim, “Structure-function relationship and diagnostic value of macular ganglion cell complex measurement using fourier-domain OCT in glaucoma,” *Investig. Ophthalmol. Vis. Sci.*, vol. 51, no. 9, pp. 4646–4651, 2010.

[257] J. C. Mwanza, J. D. Oakley, D. L. Budenz, R. T. Chang, O. J. Knight, and W. J. Feuer, “Macular ganglion cell-inner plexiform layer: Automated detection and thickness

reproducibility with spectral domain-optical coherence tomography in glaucoma," *Investig. Ophthalmol. Vis. Sci.*, vol. 52, no. 11, pp. 8323–8329, 2011.

[258] J. Flammer *et al.*, "The impact of ocular blood flow in glaucoma," *Prog. Retin. Eye Res.*, vol. 21, no. 4, pp. 359–393, 2002.

[259] Faal H, "Primary Open-Angle Glaucoma," *Community Eye Health*, vol. 25, no. 79,80, pp. 41–43, 2012.

[260] T. Yoshioka, T. Nagaoka, Y. Song, H. Yokota, T. Tani, and A. Yoshida, "Role of Neuronal Nitric Oxide Synthase in Regulating Retinal Blood Flow During Flicker-Induced Hyperemia in Cats," *Investig. Opthalmol. Vis. Sci.*, vol. 56, no. 5, p. 3113, 2015.

[261] R. a. Leitgeb, R. M. Werkmeister, C. Blatter, and L. Schmetterer, "Doppler Optical Coherence Tomography," *Prog. Retin. Eye Res.*, vol. 41, pp. 26–43, 2014.

[262] Y. Wang, A. Lu, J. Gil-Flamer, O. Tan, J. A. Izatt, and D. Huang, "Measurement of total blood flow in the normal human retina using Doppler Fourier-domain optical coherence tomography.," *Br. J. Ophthalmol.*, vol. 93, no. 5, pp. 634–7, 2009.

[263] G. C. Aschinger *et al.*, "Effect of diffuse luminance flicker light stimulation on total retinal blood flow assessed with dual-beam bidirectional doppler OCT," *Investig. Ophthalmol. Vis. Sci.*, vol. 58, no. 2, pp. 1167–1178, 2017.

[264] G. Garhöfer, H. Resch, G. Weigert, S. Lung, C. Simader, and L. Schmetterer, "Short-term increase of intraocular pressure does not alter the response of retinal and optic nerve head blood flow to flicker stimulation," *Investig. Ophthalmol. Vis. Sci.*, vol. 46, no. 5, pp. 1721–1725, 2005.

[265] E. A. Newman, "Functional hyperemia and mechanisms of neurovascular coupling in the retinal vasculature.," *J. Cereb. Blood Flow Metab.*, vol. 33, no. 11, pp. 1685–95, 2013.

[266] D. G. Buerk, C. E. Riva, and S. D. Cranstoun, "Nitric oxide has a vasodilatory role in cat optic nerve head during flicker stimuli," *Microvasc Res*, vol. 52, no. 1, p. 13–26., 1996.

[267] W. Skrandies and H. Wässle, "Dopamine and serotonin in cat retina: electroretinography

and histology.," *Exp. brain Res.*, vol. 71, no. 2, pp. 231–40, Jan. 1988.

[268] C. L. Baker, R. R. Hess, B. T. Olsen, and E. Zrenner, "Current source density analysis of linear and non-linear components of the primate electroretinogram.," *J. Physiol.*, vol. 407, no. 1988, pp. 155–176, 1988.

[269] R. a Bush and P. a Sieving, "Inner retinal contributions to the primate photopic fast flicker electroretinogram.," *J. Opt. Soc. Am. A. Opt. Image Sci. Vis.*, vol. 13, no. 3, pp. 557–65, 1996.

[270] C. L. Baker and R. F. Hess, "Linear and nonlinear components of human electroretinogram.," *J. Neurophysiol.*, vol. 51, no. 5, pp. 952–967, 1984.

[271] M. Kondo and P. A. Sieving, "Primate photopic sine-wave flicker ERG: Vector modeling analysis of component origins using glutamate analogs," *Investig. Ophthalmol. Vis. Sci.*, vol. 42, no. 1, pp. 305–312, 2001.

[272] S. Viswanathan, L. J. Frishman, and J. G. Robson, "The uniform field and pattern ERG in macaques with experimental glaucoma: Removal of spiking activity," *Investig. Ophthalmol. Vis. Sci.*, vol. 41, no. 9, pp. 2797–2810, 2000.

[273] S. Bolay *et al.*, "Blood Flow and ERG Responses to Luminance Flicker in Monkeys ," *Investig. Ophthalmol. Vis. Sci.*, vol. 44, no. 13, p. 351, May 2003.

[274] V. Patel, S. Rassam, R. Newsom, J. Wiek, and E. Kohner, "Retinal blood flow in diabetic retinopathy.," *BMJ*, vol. 305, no. 6855, pp. 678–683, 1992.

[275] W. H. Morgan, M. L. Hazelton, and D. Y. Yu, "Retinal venous pulsation: Expanding our understanding and use of this enigmatic phenomenon," *Prog. Retin. Eye Res.*, vol. 55, pp. 82–107, 2016.

[276] E. Sato, G. T. Feke, M. N. Menke, and J. Wallace McMeel, "Retinal haemodynamics in patients with age-related macular degeneration.," *Eye (Lond).*, vol. 20, no. 6, pp. 697–702, 2006.

[277] J. Yi *et al.*, "Visible light optical coherence tomography measures retinal oxygen

metabolic response to systemic oxygenation," *Light Sci. Appl.*, vol. 4, no. 9, p. e334, 2015.

[278] M. D. Knudtson *et al.*, "Variation associated with measurement of retinal vessel diameters at different points in the pulse cycle," *Br. J. Ophthalmol.*, vol. 88, no. 1, p. 57 LP-61, Dec. 2003.

[279] L. M. Peterson, S. Gu, M. W. Jenkins, and A. M. Rollins, "Orientation-independent rapid pulsatile flow measurement using dual-angle Doppler OCT.," *Biomed. Opt. Express*, vol. 5, no. 2, pp. 499–514, 2014.

[280] S. Huang *et al.*, "In vivo imaging of retinal hemodynamics with OCT angiography and Doppler OCT," *Biomed. Opt. Express*, vol. 7, no. 2, p. 663, 2016.

[281] F. Larocca, S. J. Chiu, R. P. McNabb, A. N. Kuo, J. a Izatt, and S. Farsiu, "Robust automatic segmentation of corneal layer boundaries in SDOCT images using graph theory and dynamic programming.," *Biomed. Opt. Express*, vol. 2, no. 6, pp. 1524–1538, 2011.

[282] F. Moret, C. M. Reiff, W. A. Lagrèze, and M. Bach, "Quantitative Analysis of Fundus-Image Sequences Reveals Phase of Spontaneous Venous Pulsations," *Transl. Vis. Sci. Technol.*, vol. 4, no. 5, p. 3, 2015.

Appendices

Acute moderate IOP elevation is associated temporal retinal function enhancement and ONH depression, and the conclusion can also be extended to different rat strains and different types of anesthesia. As a co-author, I have contributed to the following publications and manuscripts:

- ERG Data collection with isoflurane anesthesia.

  Choh, V., Gurdita, A., **Tan, B**., Feng, Y., Bizheva, K., McCulloch, D. L., & Joos. K.M., Isoflurane and ketamine: xylazine differentially affect intraocular pressure-associated scotopic threshold responses in Sprague-Dawley rats. Documenta Ophthalmologica. doi:10.1007/s10633-017-9597-7 (2017)

- OCT, ERG and STR data collection.

  Gurdita, A., **Tan, B**., Joos, K. M., Bizheva, K., & Choh, V. Pigmented and albino rats differ in their responses to acute intraocular pressure elevation. Documenta Ophthalmologica. DOI : 10.1007/s10633-017-9586-x (2017).